Empirical Mode Decomposition for Seismic Applications

by

Jiajun Han

A thesis submitted in partial fulfillment of the requirements for the degree of

Doctor of Philosophy

in

Geophysics

Department of Physics
University of Alberta

Abstract

Empirical mode decomposition (EMD) is a powerful signal analysis technique to analyze non-stationary signal systems, like seismic data. Through the sifting process, EMD splits the non-stationary features of the input signal into individual decomposition modes, which are called intrinsic mode functions (IMFs). Each IMF has a symmetric, narrow-band waveform, which ensures that their instantaneous frequency of them is smooth and positive. However some negative features encumber its direct application namely mode mixing and splitting, aliasing and end-point artifacts. Two variants, ensemble EMD (EEMD) and complete ensemble EMD (CEEMD) have been recently introduced to overcome some of the negative features associated with EMD. Furthermore, two EMD-like methods are also introduced: first one is the synchrosqueezing transform (SST), which decomposes the input signal into SST modes, and these modes manifest similar features to IMFs; another one is the 2D extension of EMD, bidimensional empirical mode decomposition (BEMD), which can aid image analysis.

This thesis focuses on testing the suitability of EMD methods for seismic processing and interpretation, and we present 4 new techniques. The first method is CEEMD combined with instantaneous spectra for seismic spectral decomposition. After CEEMD, the instantaneous frequency spectra manifests visibly higher time-frequency resolution than short time Fourier and wavelet transforms on both syn-

thetic and field data examples. The second method is EEMD thresholding. It is effective for suppressing random noise in each trace, which is highly attractive for microseismic processing. Furthermore, the proposed EEMD thresholding can be extended into the f-x domain as f-x EEMD thresholding, which aims to reduce dipping coherent and random noise. The third application is SST for seismic signal time-frequency analysis. It shows comparable results to CEEMD combined with instantaneous spectra; therefore it is highly suitable for high resolution seismic interpretation. The last proposed method is BEMD thresholding, which aims to reduce random noise of 2D seismic images.

Utilizing the particular features of IMFs or SST modes, the presented methods manifest excellent performance on seismic spectral decomposition and seismic denoising. The synthetic and real data examples illustrate that EMD methods are highly promising for seismic processing and interpretation.

Preface

Chapter 2 of this thesis has been published as Jiajun Han and Mirko van der Baan, “Empirical mode decomposition for seismic time-frequency analysis”, *Geophysics*, 78, 2, O9-O19, 2013. Mirko van der Baan led this project. I was responsible for code development, data analysis, figure preparation and manuscript writing.

Chapter 3 of this thesis has been published as Roberto H. Herrera, Jiajun Han and Mirko van der Baan, “Applications of the synchrosqueezing transform in seismic time-frequency analysis”, *Geophysics*, 79, 3, V55-V64, 2014. Mirko van der Baan led this project. Roberto H. Herrera wrote the manuscript. I was responsible for a part of code development, figure composition and manuscript composition.

“Science is a wonderful thing if one does not have to earn one’s living at it.”

Albert Einstein

Acknowledgements

First and foremost, I would like to thank my supervisor Mirko van der Baan. His passion for science deeply encourages me, and I enjoy the great benefit from the discussions with him during my whole Ph.D. study. His life philosophy has profoundly influenced me too, ’from easy to complicate’, ’keep life easier’, all these are greatly helpful for my future life and work. I thank my supervisor during my M.Sc study, Liguo Han in Jilin University of China. Every discussions with him help me open my mind to the geophysics, and make my work more related to industry. I am also grateful to all geophysics professors in the Department of Physics at the University of Alberta for sharing their work and knowledge. I would also like to thank the members in my group, as well as all friends in the University of Alberta for making my life colorful. Furthermore, I am grateful for the guidance from Brian Russell, Dan Hampson and all colleagues in the Geo-software group during my internship in CGG calgary. Finally, I give my deepest gratitude to my family, I couldn’t become who I am now without your support and encouragements.

Contents

List of Tables

List of Figures

List of Abbreviations

AR	autoregressive
ARMA	autoregressive moving average
BEMD	Bidimensional Empirical Mode Decomposition
BEEMD	Bidimensional Ensemble Empirical Mode Decomposition
BIMF	Bidimensional Intrinsic Mode Function
BP	Basis Pursuit
CEEMD	Complete Ensemble Empirical Mode Decomposition
CMP	Common Midpoint
CWT/WT	Continuous Wavelet Transform
EMD	Empirical Mode Decomposition
EEMD	Ensemble Empirical Mode Decomposition
f-k	Frequency - wavenumber
f-x	Frequency - Offset
IMF	Intrinsic Mode Function
MP	Matching Pursuit
SNR	Signal to Noise Ratio
SSA	Singular Spectrum Analysis
SST	Synchrosqueezing Transform
STFT	Short Time Fourier Transform
t-x	Time - Offset
1D	One-Dimensional
2D	Two-Dimensional
3D	Three-Dimensional

Chapter 1

Introduction[1]

1.1 Background

1.1.1 Time frequency analysis

Accurate and precise analysis of non-stationary spectral variations is a long standing problem aiming at revealing signal characteristics such as any underlying periodicities. The discrete Fourier transform (DFT), with its fast implementation the Fast Fourier Transform (FFT) (Cooley and Tukey, 1965; Cooley, 1969), and variants have been well studied (e.g., Hinich and Clay, 1968; Brigham, 1998). They provide an efficient way to estimate the frequency content of a discrete and finite time series. The main application of the DFT to time-varying spectra is the spectrogram, also called Short-Time Fourier Transform (STFT). Likewise, wavelet transforms and variants are now well-established and many review articles exist (e.g., Kumar and Foufoula-Georgiou, 1997; Mallat, 2008). Furthermore, S transform (Stockwell et al., 1996), halfway between the STFT and wavelet transform, also shows its effectiveness in estimating of frequency variation (Odebeatu et al., 2006; Stockwell, 2007).

All these methods are bound by the Heisenberg/Gabor uncertainty principle (Gabor, 1946) with a trade-off between time and frequency resolutions (Reine et al., 2009). Also, signal windowing leads to smearing, which correspond to the widen-

---

[1] The chapter is based in part of paper ”Spectral estimation - What’s new? What’s next?”. Jean Baptiste Tary, Roberto Henry Herrera, Jiajun Han and Mirko van der Baan, submitted, Reviews of Geophysics.

ing of the main lobe around its central frequency, and side-lobe leakage (Hall, 2006). Lately, various new transforms have been developed to circumvent these issues such as matching pursuit (MP) (Mallat and Zhang, 1993), basis pursuit (BP) (Chen et al., 2001), Empirical Mode Decomposition (EMD) coupled with the Hilbert-Huang Spectrum (Huang et al., 1998) and the synchrosqueezing transform (SST) (Daubechies et al., 2011).

All these methods can be considered as non-parametric, meaning that they do not assume any particular stationary structure prior to time-frequency (T-F) decomposition of the signal. On the other hand, parametric methods drew a lot of attention in the 80s/90s as they are not assuming zero-valued or periodic data outside the data window and hence are less restricted by smearing and leakage. Autoregressive (AR) and autoregressive moving-average (ARMA) models for example provide correct and accurate spectral estimation if the assumed model is appropriate for the investigated time series (Makhoul, 1975; Ulrych and Bishop, 1975; Kay and Marple, 1981).

In seismic processing and interpretation, time-frequency analysis, and corresponding spectral decomposition plays a significant role. It requires one of the above transformations of each individual 1D seismic trace into a 2D time-frequency representation, which describes how the frequency content varies with time. Spectral decomposition has emerged in last 15 years as an enlightening seismic attribute, producing very informative maps of thin beds, especially in clastic successions with sharp impedance contrasts (Partyka et al., 1999). These maps are typically interpreted qualitatively, using geomorphologic pattern-recognition, or semi-quantitatively, to infer relative thickness variation. Due to its effectiveness, spectral decomposition has been successfully applied in hydrocarbon detection (Castagna et al., 2003), seismic attenuation estimation (Reine et al., 2009), reservoir characterization (Li and Zheng, 2008) and so on.

Many methods exist to achieve the spectral decomposition and each has different resolution capabilities in time and frequency. As spectral decomposition provides interpreters with the details of reservoir thickness variation and geological discontinuities, high resolution techniques are helpful for more accurately locating these spectral anomalies, by decreasing spectral smearing, thus facilitating the further seismic interpretation.

1.1.2 Seismic noise attenuation

Noise suppression is a crucial step in both seismic and microseismic processing since noise compromises our ability to depict the Earth interior. For seismic processing, the common methods for suppressing random noise are CMP stacking, frequency bandpass filter, spatial prediction filtering methods and matrix rank reduction techniques (Chen, 2013). Well-known techniques, like f-x deconvolution (Canales, 1984) and f-x projection filtering (Soubaras, 1994) are examples of spatial prediction filtering methods. The coherent energy, like reflections, can be predicted using model-based approaches, and the residual are an estimate of random noise. Lately developed techniques, like f-x singular spectrum analysis (SSA) (Sacchi, 2009) and its variants (Oropeza and Sacchi, 2010, 2011) are examples for matrix rank reduction techniques. These methods are all effective for random noise attenuation, and widely accepted in the oil and gas industry. Due to the diversity of coherent noise in seismic data, there are different types of methods for coherent noise reduction. For example, the strong energy of ground roll can be effectively reduced by a f-k filter, as ground roll presents low frequency and velocity features; multiples can be separated by Radon transform from seismic reflections as they exhibit parabolic moveout after NMO; and steeply dipping coherent noise can be suppressed by a dip filter and f-x empirical mode decomposition (Bekara and Van der Baan, 2009). All these coherent noise reduction methods try to represent the seismic data in a particular domain, where the signal and coherent noise are more easily distinguished from each other. For microseismic processing, although there is only individual trace, strong electronic and random noise may bring down the quality of data severely. The traditional methods are frequency bandpass filter for suppressing the random noise, and notch process for wiping off the electronic noise.

1.2 Empirical mode decomposition

EMD, developed by Huang et al. (1998) is a powerful signal analysis technique to model non-stationary and nonlinear signal systems. As a fully data-driven technique, there is no predefined decomposition basis. EMD captures the non-stationary feature of the input signal in the decomposition modes, which are called intrinsic mode functions (IMFs). A time-frequency representation is obtained by combining EMD with the Hilbert transform to compute instantaneous frequencies (Taner et al., 1979; Magrin-Chagnolleau and Baraniuk, 1999). This is sometimes called the Hilbert-Huang spectrum (Huang et al., 1998).

EMD adaptively decomposes a multi-component signal $x(t)$ into a number K of IMFs

$$x(t) = \sum_{k=1}^{K} IMF_k + R. \tag{1.1}$$

where R is the final residual, which is a non-zero-mean slowly varying function with only few extrema. The EMD algorithm is listed below (Huang et al., 1998; Magrin-Chagnolleau and Baraniuk, 1999):

(1). Initialize: $r_0 = x(t)$, $i = 1$.

(2). Extract the $i-th$ IMF:

(a). Initialize: $h_0(t)$ = $r_i(t)$, j = 1

(b). Extract the local minima and maxima of $h_{j-1}(t)$

(c). Form the upper and lower envelopes of $h_{j-1}(t)$ by interpolating between the successive local maxima and minima using a cubic spline.

(d). Calculate the mean/average $m_{j-1}(t)$ of the upper and lower envelopes

(e). $h_j(t)$ = $h_{j-1}(t)$ - $m_{j-1}(t)$

(f). if stopping criterion is satisfied then set $h_j(t)$ as the $i-th$ IMF, else go to step (b) with $j = j+1$

(3). $r_i(t)$ = $r_{i-1}(t)$ - $imf_i(t)$.

(4). if $r_i(t)$ still has at least 2 extrema then go to (2) with $i = i+1$, else the decomposition is finished and $r_i(t)$ is the final residual R.

Each IMF is obtained through the sifting process, which is referred from step (a) to (f). After decomposition, the number of extrema and the number of zero crossings of each IMF are equal or differ at most by one; furthermore, at any point, the mean value of the envelope defined by the local maxima and the envelope defined by the local minima is zero. These conditions are necessary to ensure that each IMF has a localised frequency content by preventing frequency spreading (Huang et al., 1998). Moreover, EMD has several interesting properties that makes it an attractive tool for signal analysis. It results in complete signal decomposition, i.e., the original signal is reconstructed by summing all IMFs. No loss of information occurs. The EMD is a quasi-orthogonal decomposition in that the cross-correlation coefficients between the different IMFs are always close to zero. This minimizes energy leakage between the IMFs (Bekara and Van der Baan, 2009).

There are two variants to improve some drawbacks associated with EMD, namely ensemble EMD (EEMD) and complete ensemble EMD (CEEMD). We discuss them in next section, and their implementation is introduced in chapter 2. Based on the EMD/IMFs features, there are also two extensions developed.

The first extension is bidimensional empirical mode decomposition (BEMD), which is 2D extension of EMD for the image analysis (Linderhed, 2002; Nunes et al., 2003). Its theory is totally same as EMD: through the sifting process, the decomposition modes are called bidimensional intrinsic mode functions (BIMFs). The only different step between two methods is the upper and lower envelopes are created by 2D interpolation methods for BEMD, otherwise using 1D interpolation for EMD. As the fundamental theories of two methods are same, BEMD shares several similar promising features with EMD. BEMD also keeps the complete decomposition feature, no loss of information is incurred by summing all BIMFs. The mean envelope of each BIMF is guaranteed to be zero or nearly zero, and the BIMFs are locally orthogonal. The only difference between BIMFs and IMFs is the number of local extrema and the number of zero crossings. For IMFs, the number of local extrema and the number of zero crossings must be equal or differ by at most one. However, due to the properties of an image, it is impossible to satisfy this property for BIMFs (Bhuiyan et al., 2008).

Another extension is SST, which is originally proposed as an EMD-like method

(Daubechies et al., 2011). This is because SST can also decompose the input signal into SST modes, which show the similar features with IMFs. Moreover, SST has a strong mathematical foundation, and it is essentially a frequency reassignment technique based on wavelet transform. Due to the similarity between SST and EMD, there are several papers to compare these two techniques (Mandic et al., 2013; Auger et al., 2013; Herrera et al., 2014). In chapter 3, we elaborately introduce SST theory and extend it for seismic time-frequency analysis.

1.2.1 Time-frequency analysis by EMD methods

The trait of EMD on time-frequency analysis is fundamentally different from all the previous techniques. From the fundamental ideas, STFT, wavelet transform, S transform and even the reassignment technique, like SST, are all the same, as they drop the comparison with a template performed by an inner product of signal and basis functions. On the other hand, AR methods reduce a time series to a small set of parameters, and estimate the future values by a set of past ones. EMD, as the name implies, is an empirical decomposition in that no a priori decomposition basis is chosen such as sines and cosines for the Fourier transform or a mother wavelet for the Wavelet transform. Moreover, there is no estimation function/assumption assisted with it. Through the sifting process, EMD aims at solving the predicaments of instantaneous frequency.

From the birth in geophysics of instantaneous frequency (Taner et al., 1979), scholars have begun to doubt its physical meaning. The instantaneous frequency holds the promise of the highest possible time resolution since it produces a frequency at each time sample, but at the expense of a very limited frequency resolution due to the Heisenberg/Gabor uncertainty principle (Gabor, 1946). For the mono-component signal, instantaneous frequency manifests its superiorities, high accuracy and resolution. However, the contradictory of its physical meaning shows up when apply for multi-component signal. Saha (1987) points out it approximates the average Fourier spectral frequency weighted by the amplitude spectrum. In seismic interpretation, direct calculation can lead to instantaneous frequencies, which fluctuate rapidly with spatial and temporal location. For obtaining the smoother instantaneous frequency, taper and averaging techniques are necessary (Fomel, 2007). Moreover, the instantaneous frequency is sensitive to the noise in seismic data. All these disadvantages make it is gradually replaced by spectral decomposition techniques in the 1990s (Chakraborty and Okaya, 1995; Partyka et al., 1999).

Huang et al. (2009) summarize the applicability conditions for instantaneous frequency, namely, the time series must be mono-component and narrow-band. Through the sifting process, each IMF is guarantee to be a symmetric, smooth and narrow-band waveform, thus the IMFs are much closer to applicability conditions of instantaneous frequency than the original time series.

Even though EMD offers several promising properties, some features encumber its direct applications namely mode mixing and splitting, aliasing and end-point artifacts (Mandic et al., 2013). EMD is also relatively inefficient for flat signals due to the extrema interpolation step, and for signals with frequency components that are not well-separated.

Two variants were recently introduced to overcome some of the negative features associated with EMD, namely EEMD and CEEMD. EEMD, briefly speaking, is EMD combined with noise stabilization. Using the injection of controlled zero mean Gaussian white noise, EEMD effectively reduces mode mixing problem (Wu and Huang, 2009a; Tong et al., 2012; Mandic et al., 2013). Adding white Gaussian noise helps perturbing the signal and enables the EMD algorithm to visit all possible solutions in the finite neighborhood of the final answer, and it also takes advantage of the zero mean of the noise to cancel aliasing (Wu and Huang, 2009a). However, EEMD leaves two problems: first, different noise realizations may end up with different numbers of IMFs, which could mix up the IMFs after each decomposition in the frequency domain; second, EEMD does not maintain the complete decomposition feature of EMD (Torres et al., 2011a; Han and Van der baan, 2013). In other words, contrary to EMD, the sum of the IMFs obtained via EEMD does not necessarily reconstruct the original signal. The reconstruction error of EEMD is often acceptable when the injected noise is of small amplitude.

The robust improvement of EEMD is CEEMD, proposed by Torres et al. (2011a), which obtains again the final IMFs sequentially, contrary to EEMD. Briefly speaking, CEEMD equals EEMD but applies averaging on IMF 1 first before continuing to next one. It solves not only the mode mixing problem, but also leads to complete signal reconstruction. We combine CEEMD with instantaneous spectra for seismic time-frequency analysis, which is presented in chapter 2. The new method manifests visibly higher time-frequency resolution than short-time time Fourier and wavelet transforms; therefore it is attractive for high resolution seismic spectral decomposition (Han and Van der Baan, 2013).

SST is a derivation of the wavelet transform empowered by a reassignment step. It concentrates the frequency content around the instantaneous frequencies in the wavelet domain. SST assumes that the signal is a superposition of nonstationary monochromatic wavelets and can be efficiently decomposed by the CWT, followed by the computation of the instantaneous frequencies plus a reassignment step to concentrate the energy around the ridges. Due to the reassignment procedure, SST shows high time-frequency resolution feature, and it is robust to the noise (Thakur et al., 2013). Han et al. (2013) and Herrera et al. (2014) extend its explanation with applications to seismic signals.

1.2.2 Noise attenuation by EMD methods

After explored the filter band structure of EMD on white Gaussian noise (Flandrin et al., 2004a), scholars began to pay more attention to noise reduction from EMD view. These applications mainly focus on random noise attenuation and first emerge in signal processing area. The initial attempt is partial reconstructions with the selected IMFs to suppress random noise for the input noisy signal (Flandrin et al., 2004). Through comparing the theoretical IMFs energy distribution on white Gaussian noise and true IMFs energy distribution of noisy signal, Flandrin et al. (2004) select the IMFs, which contain mainly signal information for reconstruction and throw out the other IMFs. This approach resembles a properly set bandpass filter, but the selected IMFs still may be noise contaminated. Since EMD can be treated as a wavelet-like transform (Wu and Huang, 2004; Flandrin et al., 2004a), Boudraa and Cexus (2006) combine wavelet denoising techniques with EMD. They improve the previous denoising scheme by using adaptive thresholding for each IMF. This approach is based on the IMFs energy distribution on random noise (Huang and Shen, 2005), and shows better results than wavelet denoising. Kopsinis and McLaughlin (2009) further improve this idea. Inspired by translation invariant wavelet thresholding, they propose an iterative EMD denoising method to enhance Boudraa and Cexus (2006)'s results, furthermore, they also propose IMF interval thresholding instead of original thresholding (hard and soft thresholding) methods to fit IMFs features. Recently, Chang and Liu (2010) remove the random noise in ECG signal by combining EEMD with Wiener filter, and a hybrid method based higher order statistics has also been proposed (Tsolis and Xenos, 2011).

In geophysical data processing, geophysicists have never forgotten the powerful denoising capabilities of EMD. Battista et al. (2007) remove cable strum noise in seismic data by exploiting EMD. Battista et al. (2009) utilize EMD for dewowing the GPR datasets. The hybrid methods, which combine EMD with wavelet transform (Chen et al., 2012) and curvelet transform (Dong et al., 2013), are developed to reduce random noise in seismic data. These applications are all trace based techniques, and the denoising strategies are only from the purely signal processing view. However, the geophysical datasets are charactered by the lateral coherence, like seismic and GPR data. Bekara and Van der Baan (2009) first extend EMD into f-x domain, as the t-x domain linear or quasilinear events manifest as a superposition of harmonics in the f-x domain. They eliminate the first EMD component in the f-x domain to attenuate random and coherent seismic noise, and this technique is termed as f-x EMD. Based on this strategy, Chen and Ma (2014) and Chen et al. (2014) improve f-x EMD by combining AR model and f-x SSA.

In this thesis, we propose two novel denoising techniques. The first one is EEMD thresholding based on EMD. It is trace based method for suppressing random noise in microseismic data, and it can be also applied into f-x domain for removing both random and coherent noise in seismic data. This work is presented in chapter 4. Another one is BEMD thresholding based on BEMD, which is presented in chapter 6. BEMD thresholding is effective for reducing random noise in seismic vertical profile and seismic time slice.

1.3 Motivation and contribution

EMD has developed more than 15 years (Huang et al., 1998), and recently, its two variants, EEMD, CEEMD and its 2D extension, BEMD have proposed. Although EMD methods have shown the powerful and potential capabilities in signal processing and a few geophysical areas, many geophysicists still tend to avoid EMD, this is mainly because these methods are lack connection to a signal model. The motivations of this thesis are: first, to show the suitability of EMD based methods for seismic processing and interpretation; second, we hope this thesis will draw the attention of mathematicians to EMD, from mathematical view to prove the technique.

The contributions of this thesis are the following:

- We present CEEMD combined with instantaneous frequency for seismic spectral decomposition.
- We introduce the SST, an EMD-like transform for seismic time-frequency analysis.
- We propose a trace based denoising method, EEMD thresholding, to reduce random noise in microseismic data. We also extend it into f-x domain for suppressing random and coherent noise in seismic data.
- We develop BEEMD to alleviate interpolation artifacts caused by the type of chosen interpolant for BEMD.
- We calculate the energy distribution of each BIMF on white Gaussian noise. Based on this energy distribution, we propose the BEMD thresholding method for suppressing random noise for 2D seismic images.

1.4 Thesis overview

Chapter 2 describes the EMD methods for seismic spectral decomposition. CEEMD is a robust extension of EMD. It solves not only the mode mixing problem, but also leads to complete signal reconstructions. After CEEMD, instantaneous spectra manifests higher time-frequency resolution than the traditional methods, like short time

Fourier and wavelet transforms. The synthetic and field data examples clarify the effectiveness of the proposed method.

Chapter 3 introduces the SST for seismic spectral decomposition. SST is originally proposed as an EMD-like method, and it has a strong mathematical foundation based on frequency reassignment of wavelet transform. SST and CEEMD give comparable results in different applications. SST is therefore attractive for high resolution time-frequency analysis of seismic data.

Chapter 4 proposes a novel trace-based denoising technique, EEMD thresholding. The method is fully data-driven, and effective for suppressing random noise in different signal to noise ratio (SNR) cases in each trace. Considering the lateral coherence of seismic data, we extend the proposed method to the f-x domain as f-x EEMD thresholding, which aims to reduce dipping coherent and random noise. The synthetic, microseismic and seismic examples illustrate the good performance of our proposed methods.

Chapter 5 develops BEEMD, which alleviates many interpolation artifacts caused by the type of chosen interpolant for BEMD. Thereby facilitating any interpretation without the need to adapt the interpolant each time to the image.

Chapter 6 is about a novel 2D image denoising technique. From Monte Carlo simulations, we find that BEMD behaves like a constant-Q, wavelet-like, filter bank structure for white Gaussian noise. Based on the energy distribution of BIMFs, a BEMD thresholding method is proposed. The method is fully data-driven, and effective for suppressing random noise in seismic data. The seismic examples illustrate the good performance of the proposed method.

Chapter 7 gives the discussion and conclusions of the thesis. Moreover, future work is discussed.

Chapter 2

Empirical mode decomposition for seismic time-frequency analysis[1]

Summary

Time frequency analysis plays a significant role in seismic data processing and interpretation. Complete ensemble empirical mode decomposition (CEEMD) is a robust extension of empirical mode decomposition (EMD), and it decomposes a seismic signal into a sum of oscillatory components, with guaranteed positive and smoothly varying instantaneous frequencies. Analysis on synthetic and real data demonstrates that this method promises higher spectral resolution than the short-time Fourier transform or wavelet transform. Application on field data thus offers the potential of highlighting subtle geologic structures that might otherwise escape unnoticed.

2.1 Introduction

The most common tool for spectral analysis is the Fourier transform; however, if applied to the entire trace, it provides no information about local frequency variations. Such knowledge of how the frequency content of a signal varies in time can be significant. Local time-frequency analysis is commonly used in both seismic

---

[1] A version of this chapter has been published. Jiajun Han and Mirko van der Baan, Geophysics, 2013, 78, 2, O9-O19.

processing and interpretation, and there is therefore a rich history and diversity in developed decomposition methodologies.

Taner et al. (1979) propose the instantaneous frequency attribute which is useful in correlation and appears to indicate hydrocarbon accumulations. The wavelet transform developed by Morlet et al. (1982) manifests more flexibility and superiority in geophysical applications (Chakraborty and Okaya, 1995). Partyka et al. (1999) first demonstrate the value of spectral decomposition in 3D seismic data interpretation using tapered short time Fourier transforms. Barnes (2000) improves the interpretability of instantaneous attributes by using a weighted average window. Castagna et al. (2003) demonstrate the suitability of the instantaneous spectrum for hydrocarbon detection. Liu and Marfurt (2007) also utilize the instantaneous spectrum for detecting geological structures. Odebeatu et al. (2006) apply the S-transform to reflection data and relate the gas saturation to a clear spectral signature. Li and Zheng (2008) employ the Wigner-Ville distribution for carbonate reservoir characterization. Reine et al. (2009) find transforms with varying time windows (e.g., wavelet transform and S-transform) allow for more robust estimation of seismic attenuation. Most recently, local attributes derived from an inversion-based time-frequency analysis have also been used in seismic interpretation (Liu et al., 2011).

Time frequency decomposition maps a 1D signal of time into a 2D image of frequency and time, which describes how the frequency content varies with time. The widely used short time Fourier transform calculates the fast discrete Fourier transform in each time window to compute the spectrogram. The window length determines the tradeoff between time and frequency resolution as the decomposition basis of sine and cosine waves can only provide a fixed spectral resolution (Mallat, 2008). To overcome the limitations of the short time Fourier transform, wavelet based methods have been applied for seismic time frequency analysis. Chakraborty and Okaya (1995) compare the wavelet transform with Fourier based methods for performing time frequency analysis on seismic data, and show the superiority of the wavelet transform in terms of spectral resolution. Likewise, the S-transform is proposed by Stockwell et al. (1996). It can be interpreted as a hybrid of the wavelet transform and short time Fourier transform. Short time Fourier, wavelet and S-transforms have all been successfully applied to seismic time-frequency analysis; yet they are all inherently limited in terms of time-frequency resolution by their intrinsic choice of decomposition basis. The computation of instantaneous frequencies seems to offer the highest possible time-frequency resolution as an individual frequency is obtained at each time sample. Unfortunately, negative frequencies, which hold uncertain physical interpretation, are not uncommon (Barnes, 2007; Fomel, 2007). In this chapter we explore the possibilities of using the Empirical Mode Decomposition (Huang et al., 1998) in combination with instantaneous frequencies, since this is guaranteed to produce positive values only.

The empirical mode decomposition (EMD) method developed by Huang et al. (1998) is a powerful signal analysis technique for non-stationary and nonlinear systems. EMD decomposes a seismic signal into a sum of intrinsic oscillatory components, called Intrinsic Mode Functions (IMFs). Each IMF has different frequency components, potentially highlighting different geologic and stratigraphic information. Furthermore, high-resolution time-frequency analysis is possible by combining EMD with the instantaneous frequency. The resulting time-frequency resolution promises to be significantly higher than that obtained using traditional time-frequency analysis tools, such as short time Fourier and wavelet transforms.

The empirical mode decomposition methods have progressed from EMD to ensemble empirical mode decomposition (EEMD) (Wu and Huang, 2009a), and recently a complete ensemble empirical mode decomposition (CEEMD) has been proposed by Torres et al. (2011a). Even though EMD methods offer many promising features for analyzing and processing geophysical data, there have been few applications in geophysics. Magrin-Chagnolleau and Baraniuk (1999) and Han and Van der Baan (2011) use EMD to obtain robust seismic attributes. Battista et al. (2007) exploit EMD to remove cable strum noise in seismic data. Bekara and Van der Baan (2009) eliminate the first EMD component in the f-x domain to attenuate random and coherent seismic noise. Huang and Milkereit (2009) utilize the EEMD to analyze the time frequency distribution of well logs.

The objective of this chapter is to show the suitability of EMD-based methods for seismic time frequency analysis. First, we describe and illustrate the various EMD procedures. Next, using a synthetic example, we show the combination of CEEMD with instantaneous frequencies promises higher time frequency resolution than either the short time Fourier or wavelet transforms. Finally, we apply the technique on field data to highlight various geologic structures.

2.2 Theory

2.2.1 Empirical Mode Decomposition

EMD decomposes a data series into a finite set of signals, called intrinsic mode functions (IMFs). The IMFs represent the different oscillations embedded in the data. They satisfy two conditions: (1) in the whole data set, the number of extrema and the number of zero crossings must either equal or differ at most by one; and (2) at any point, the mean value of the envelope defined by the local maxima and the envelope defined by the local minima is zero. These conditions are necessary to ensure that each IMF has a localised frequency content by preventing frequency spreading due to asymmetric waveforms (Huang et al., 1998).

EMD is a fully data-driven separation of a signal into fast and slow oscillation components. The IMFs are computed recursively, starting with the most oscillatory one. The decomposition method uses the envelopes defined by the local maxima and the local minima of the data series. Once the maxima of the original signal are identified, cubic splines are used to interpolate all the local maxima and construct the upper envelope. The same procedure is used for local minima to obtain the lower envelope. Next, one calculates the average of the upper and lower envelopes and subtracts it from the initial signal. This interpolation process is continued on the remainder. This sifting process terminates when the mean envelope is reasonably zero everywhere, and the resultant signal is designated as the first IMF. The first IMF is subtracted from the data and the difference is treated as a new signal on which the same sifting procedure is applied to obtain the next IMF. The decomposition is stopped when the last IMF has a small amplitude or becomes monotonic (Huang et al., 1998; Bekara and Van der Baan, 2009; Han and Van der Baan, 2011). The sifting procedure ensures the first IMFs contain the detailed components of the input signal; the last one solely describes the signal trend.

Some properties that render EMD interesting for seismic signal analysis are (1) the decomposition is complete in the sense that summing all IMFs reconstructs the original input signal and no loss of information is incurred; (2) IMFs are quasi-orthogonal such that the crosscorrelation coefficients between the different IMFs are always close to zero; (3) the IMFs have partially overlapping frequency contents differentiating the decomposition from simple bandpass filters; (4) no predefined decomposition basis is defined in contrast with Fourier, wavelet and S-transforms (Huang et al., 1998; Flandrin et al., 2004a; Bekara and Van der Baan, 2009).

Unfortunately as desirable as the last two properties can be they may also constitute a major obstacle restricting the performance of EMD due to intermittency and mode mixing (Huang, 1999; Huang et al., 2003). Mode mixing is defined as a single IMF either consisting of signals of widely disparate scales or a signal of a similar scale residing in different IMF components (Huang and Wu, 2008). Deering and Kaiser (2005) try to use signal masking to solve the mode mixing problem. However the masking function is complicated to estimate in real world applications. In the next section we therefore introduce the recently proposed ensemble and complete ensemble EMD variants designed to prevent mode mixing.

2.2.2 Ensemble Empirical Mode Decomposition

Based on the filter bank structure of EMD (Flandrin et al., 2004a), Wu and Huang (2009a) propose the ensemble EMD (EEMD) to overcome mode mixing. EEMD is a noise-assisted analysis method. It injects noise into the decomposition algorithm to stabilize its performance.

The implementation procedure for EEMD is simple (Wu and Huang, 2009a):

(1). Add a fixed percentage of Gaussian white noise onto the target signal,

(2). Decompose the resulting signal into IMFs,

(3). Repeat steps (1) and (2) several times, using different noise realizations;

(4). Obtain the ensemble averages of the corresponding individual IMFs as the final result.

The added Gaussian white noise series are zero mean with a constant flat frequency spectrum. Their contribution thus cancels out and does not introduce signal components not already present in the original data. The ensemble averaged IMFs maintain therefore their natural dyadic properties and effectively reduce the chance of mode mixing. More explanation can be found in Appendix B.

Although EEMD can improve EMD performance, it does leave another question: is it a complete decomposition? Does the sum of all resulting IMFs reconstruct the original signal exactly? Unfortunately by design each individual noise-injected EMD application can produce a different number of IMFs. Summing the ensemble-averaged IMFs does not perfectly recreate the original signal, although the reconstruction error decreases with increasing number of employed noise realizations at the expense of increasing computation times.

2.2.3 Complete Ensemble Empirical Mode Decomposition

Complete ensemble empirical mode decomposition (CEEMD) is also a noise-assisted method. The procedure of CEEMD can be described as follows (Torres et al., 2011a):

First, add a fixed percentage of Gaussian white noise onto the target signal, and obtain the first EMD component of the data with noise. Repeat the decomposition I times using different noise realizations and compute the ensemble average to define it as the first IMF_1 of the target signal. Thus,

$$IMF_1 = \frac{1}{I}\sum_{i=1}^{I} E_1[x + \xi w_i], \tag{2.1}$$

where IMF_1 is the first EMD component of the target signal x , w_i is zero-mean Gaussian white noise with unit variance, ξ is a fixed coefficient, and it is defined as amount of input Gaussian white noise, which is relative to the standard deviation of the input signal. E_i produces the i-th IMF component and I is the number of realizations.

Then calculate the first signal residue r_1,

$$r_1 = x - IMF_1. \tag{2.2}$$

Next decompose realizations $r_1 + \xi E_1[w_i]$, i=1,2,...,I, until they reach their first IMF conditions and define the ensemble average as the second IMF_2:

$$IMF_2 = \frac{1}{I}\sum_{i=1}^{I} E_1[r_1 + \xi E_1[w_i]]. \tag{2.3}$$

For k = 2,3,...,K calculate the k-th residue: $r_k = r_{k-1} - IMF_k$, then extract the first IMF component of $r_k + \xi E_k[w_i]$, i=1,2,...,I and compute again their ensemble average to obtain $IMF_{(k+1)}$ of the target signal:

$$IMF_{(k+1)} = \frac{1}{I}\sum_{i=1}^{I} E_1[r_k + \xi E_k[w_i]]. \tag{2.4}$$

The sifting process is continued until the last residue does not have more than two extrema, producing,

$$R = x - \sum_{i=1}^{I} IMF_k, \tag{2.5}$$

where R is the final residual, and K is the total number of IMFs. Therefore the target signal can then be expressed as:

$$x = \sum_{k=1}^{K} IMF_k + R. \tag{2.6}$$

Equation (2.6) makes CEEMD a complete decomposition method (Torres et al., 2011a). Compared with both EMD and EEMD, CEEMD not only solves the mode mixing predicament, but also provides an exact reconstruction of the original signal. Therefore, it is more suitable than EMD or EEMD to analyze seismic signals.

2.2.4 Instantaneous frequency

The local symmetry property of the IMFs ensures that instantaneous frequencies are always positive, thereby rendering EMD or its variants interesting for time-frequency analysis (Huang et al., 1998). Seismic instantaneous attributes (Taner et al., 1979) are derived from the seismic trace $x(t)$ and its Hilbert transform $y(t)$ by computing its analytic signal, given by,

$$z(t) = x(t) + iy(t) = A(t)exp[i\theta(t)]. \tag{2.7}$$

where $A(t)$ and $\theta(t)$ denote the instantaneous amplitude and instantaneous phase, respectively. Instantaneous amplitude is the trace envelope, also called reflection strength, defined as,

$$A(t) = \sqrt{x^2(t) + y^2(t)}. \tag{2.8}$$

Instantaneous frequency $IF(t)$ is defined as the first derivative of instantaneous phase. Thus,

$$IF(t) = \frac{1}{2\pi}\frac{d\theta(t)}{dt}. \tag{2.9}$$

In order to prevent ambiguities due to phase unwrapping in equation (2.9), the instantaneous frequency can be calculated instead from

$$IF(t) = \frac{1}{2\pi}\frac{x(t)y'^{(}t) - x'^{(}t)y(t)}{x(t)^2 + y(t)^2}, \tag{2.10}$$

where prime denotes derivative with respect to time.

We use equations (2.8) and (2.10) to compute instantaneous amplitudes and frequencies for each IMF. Appendix A shows how to create 2D instantaneous spectra from 1D instantaneous attributes. Contrary to classical application of instantaneous attributes to the original signal, this procedure produces a multitude of instantaneous frequencies at each time sample, namely one for each IMF, allowing for a more in-depth signal analysis.

We also compute the peak frequency of the various IMFs and other decomposition methods to create a single attribute. It is defined as the frequency where the maximum energy in each time sample occurs. Peak frequency extraction is a useful kind of spectral decomposition technique which it has been widely applied in signal processing research (Marfurt and Kirlin, 2001; Boashash and Mesbah, 2004).

This attribute has the advantage that it produces a single image convenient for interpretation purposes. Further analysis using the individual frequency slices remains always feasible. In a similar fashion, Marfurt and Kirlin (2001) introduce a mean-frequency attribute as a way to summarize the information contained in a spectral decomposition.

2.3 Examples

2.3.1 Synthetic data: EMD, EEMD and CEEMD

In this section, we first compare the various EMD-based methods using synthetic signals to demonstrate the advantages of CEEMD. Then, we show that instantaneous spectral analysis after CEEMD has higher time-frequency resolution than traditional tools, like the short time Fourier and wavelet transforms.

The signal in Figure 2.1 is comprised of an initial 20Hz cosine wave, superposed 100Hz Morlet atom at 0.3s, two 30Hz Ricker wavelets at 1.07s and 1.1s, and three different frequency components between 1.3s and 1.7s of respectively 7, 30 and 40Hz. Noted that the 7 Hz frequency components are not continuous, comprise less than one-period portions, appearing at 1.37s, 1.51s and 1.65s.

EMD decomposes the synthetic data into 7 IMFs (Figure 2.2). The IMFs in Figure 2.2 show mode mixing deficiencies. IMF1 does not solely extract the high frequency Morlet atom, but is polluted with low frequency components. Likewise IMF2 and IMF3 mix low and high-frequency components from a variety of signal components. This makes it difficult to recognize the individual contributions of each component to various IMFs, thereby complicating signal analysis.

Figure 2.3 contains the EEMD output with 10% added Gaussian white noise and 100 realizations. The mode mixing problem is reduced to a large extent; for instance, the 100Hz Morlet atom is completely retrieved in IMF1. IMF 2 mainly contains the 40Hz signal, which is the second highest frequency component. Some slight mode mixing still occurs in IMF3 and IMF4, but at a significantly reduced level compared with the EMD output.

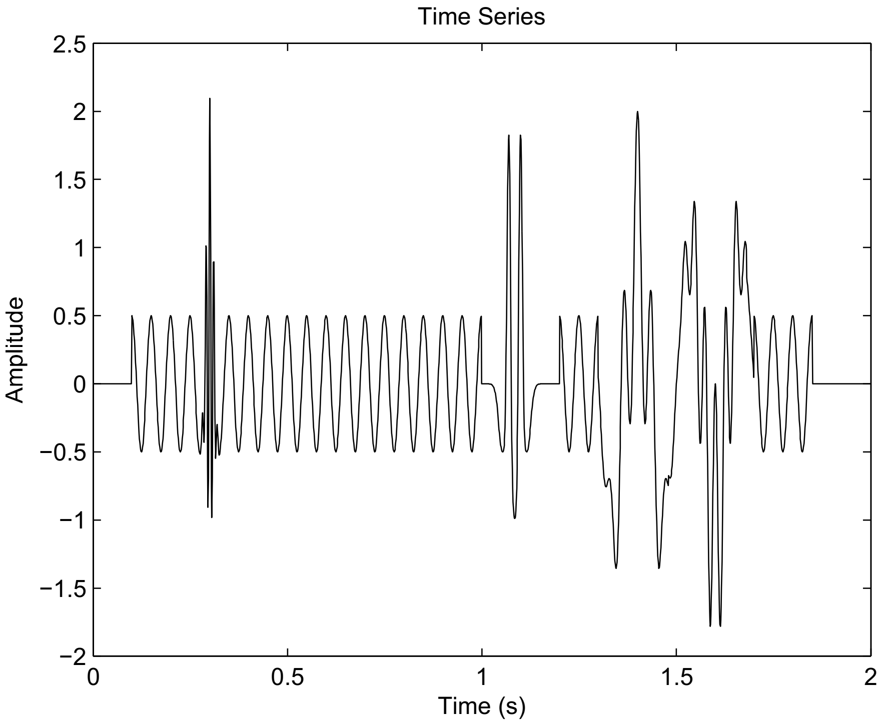

Figure 2.1: Synthetic example: background 20Hz cosine wave, superposed 100Hz Morlet atom at 0.3s, two 30Hz Ricker wavelets at 1.07s and 1.1s, and there are three different frequency components between 1.3s and 1.7s.

The CEEMD result also using 10% Gaussian white noise and 100 realizations is shown in Figure 2.4. The resulting IMF1 is similar to the one obtained by EEMD, retrieving the 100Hz Morlet atom completely. The resulting IMF2 and IMF3 contain mostly the 40Hz signal at 1.6s as well as some other higher frequency components, and IMF4 reflects the two 30Hz Ricker wavelets around 1.1s, 30Hz frequency component at 1.4s and the remainder of the 40Hz signal at 1.6s. The background 20Hz cosine wave is mainly reflected in IMF5. CEEMD is least affected by mode mixing of all EMD variants.

Figure 2.5 displays the reconstruction error for both EEMD and CEEMD results. EEMD does not perfectly reproduce the original signal with a reconstruction error of about 0.5% of the total energy; the CEEMD one is close to machine precision and thus negligible.

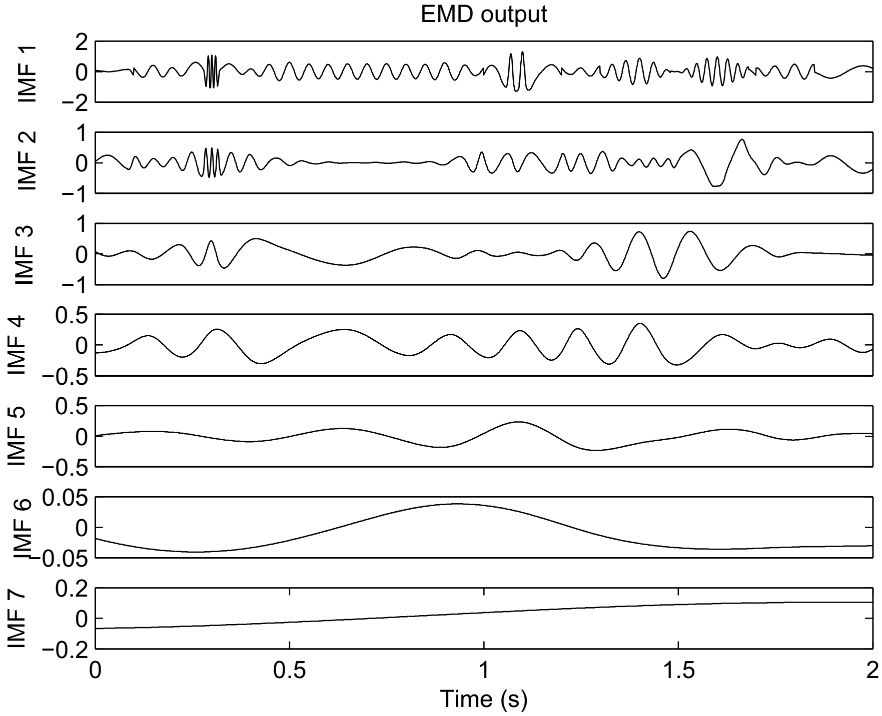

Figure 2.2: EMD output displaying mode mixing. IMF1 extracts both the high frequency Morlet atom and some low frequency components. IMF2 and IMF3 also mix different signal components.

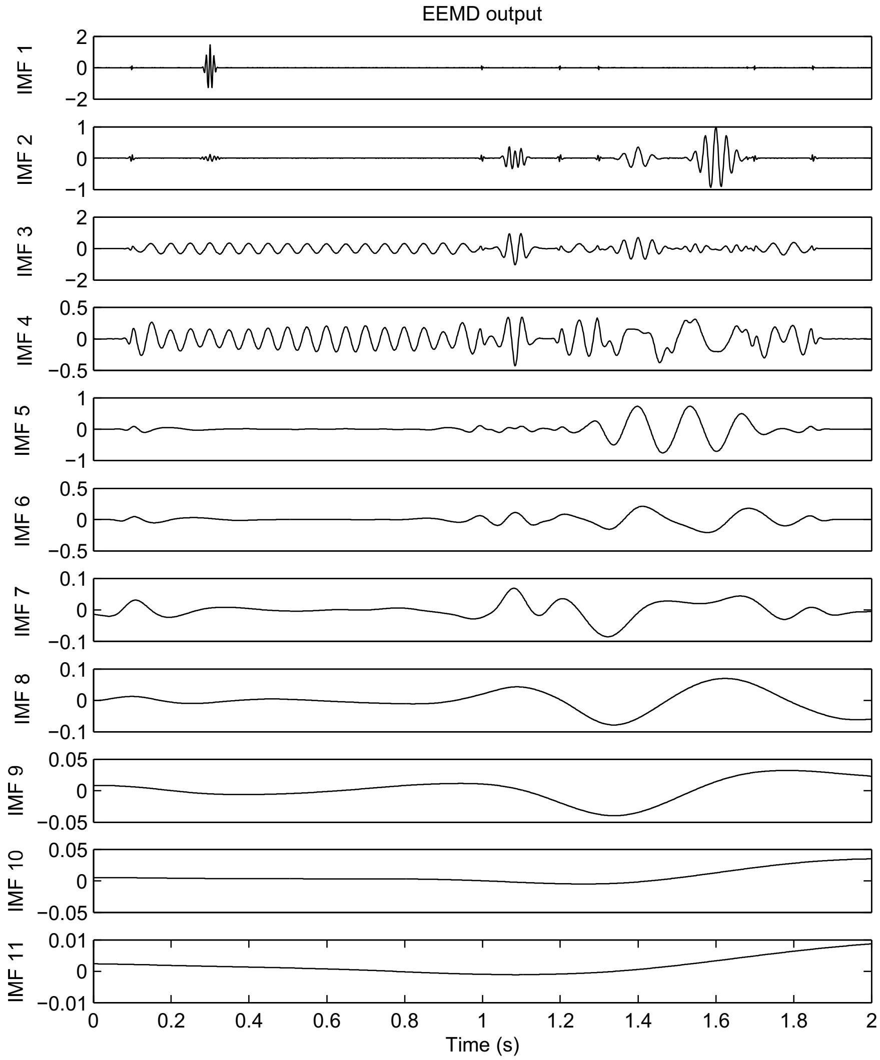

Figure 2.3: EEMD output with 10% added Gaussian white noise and 100 realizations. Although some mode mixing still occurs in IMF3 and IMF4, the mode mixing problem is reduced to a large extent compared with the EMD output (Figure 2.2).

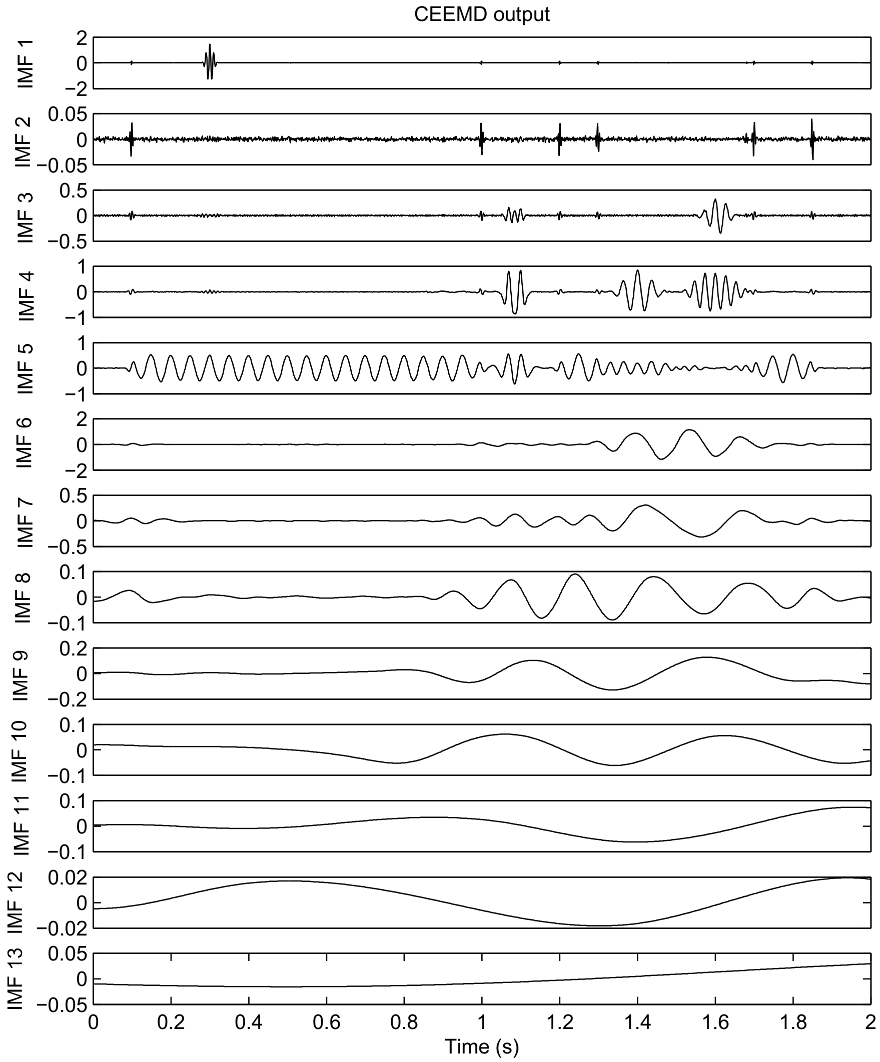

Figure 2.4: CEEMD output with 10% added Gaussian white noise and 100 realizations. The output is least affected by mode mixing of all EMD variants (compare with Figures 2.2 and 2.3).

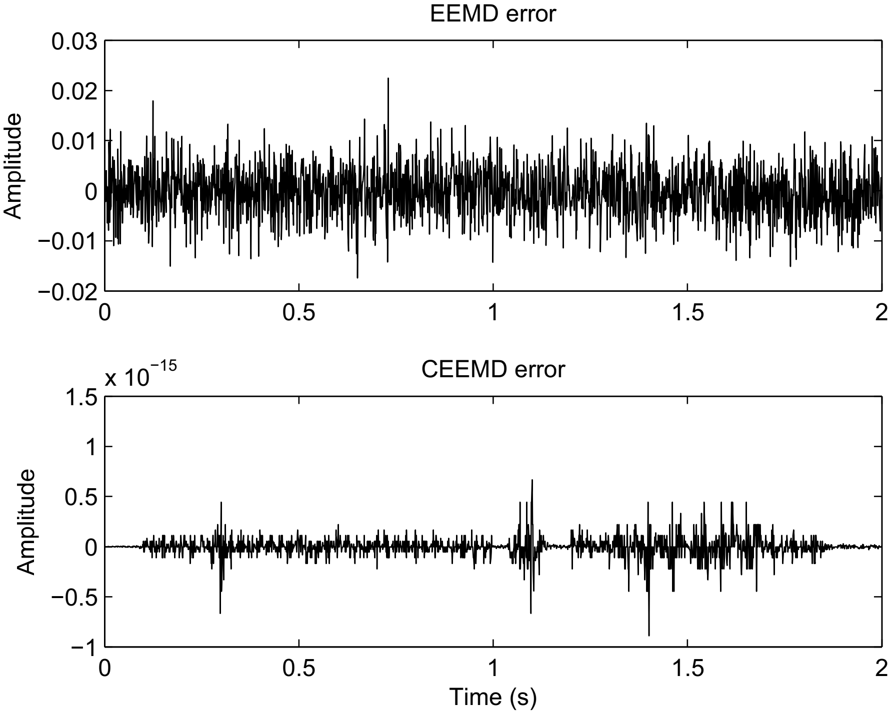

Figure 2.5: Reconstruction error for both EEMD and CEEMD results. EEMD can lead to non-negligible reconstruction error, whereas it is close to machine precision for CEEMD.

2.3.2 Synthetic data: Instantaneous frequency

After the CEEMD decomposition, each IMF is locally symmetric, such that the instantaneous frequency of each IMF is smoothly varying and guaranteed to be positive. We compute the instantaneous frequency of each IMF using equation 2.10 and associated instantaneous amplitude with equation 2.8. It is possible to smooth the resulting time-frequency image by means of a convolution with a 2D Gaussian filter of pre-specified width. This is useful for both display purposes and initial comparison with other time-frequency transforms. Next, we compare the resulting instantaneous spectrum, with the Short time Fourier and wavelet transforms for the same synthetic trace shown in Figure 2.1.

All three methods can discriminate the various frequency components between 1.2s and 2s, namely the 7, 30 and 40Hz signals, with acceptable temporal and spectral resolution. None of these three methods can identify the individual portions of the three 7 Hz frequency components, but solely their joint presence. The short-time Fourier transform with a 170ms time window (Figure 2.6) does not distinguish between the two Ricker wavelets clearly at 1.07s and 1.1s due to its fixed time-frequency resolution and their close spacing of 30ms. Wavelet analysis (Figure 2.7) fares better; however, the spectral resolution for the 100Hz Morlet wavelet at 0.3s is poor.

Figure 2.8 displays the instantaneous spectrum after CEEMD. The 100Hz Morlet wavelet, both 30Hz Ricker wavelets and three different frequency components are recovered with the highest time-frequency resolution. A small Gaussian weighted filter with width of 6×6 time and frequency samples is applied to the instantaneous spectrum for display purposes.

After calculating the instantaneous frequency, we can control the time-frequency resolution by varying the size of Gaussian weighted filter. Figure 2.9 shows the resulting instantaneous spectrum using a 30×30 Gaussian weighted filter, creating a result more comparable to the short-time Fourier and wavelet transforms (Figure 2.6 and 2.7).

This synthetic example shows the potentially significantly higher time-frequency resolution of CEEMD combined with instantaneous frequencies over that obtainable with the short time Fourier and wavelet transforms.

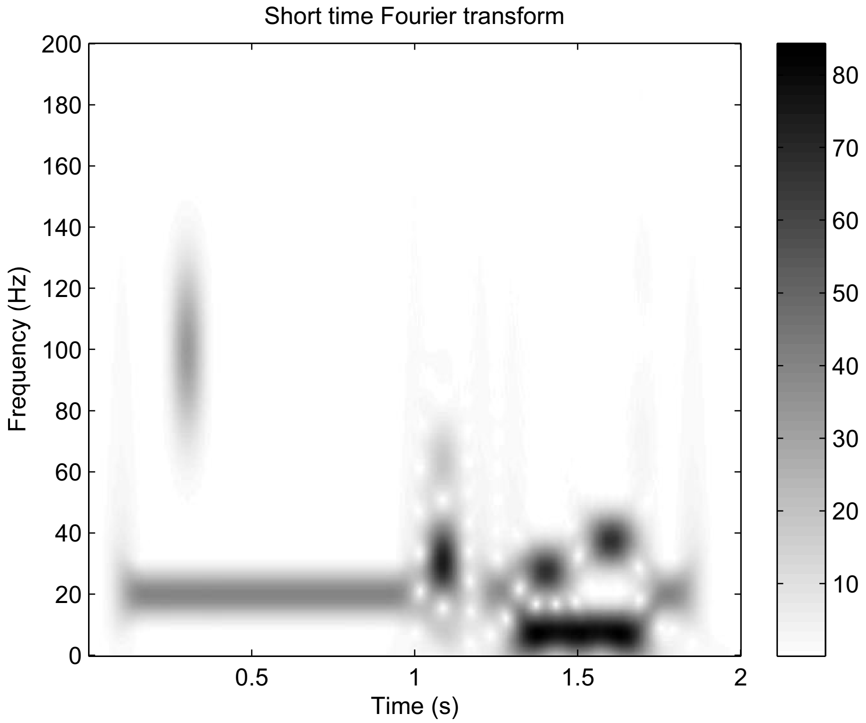

Figure 2.6: Amplitude spectrum from a short-time Fourier transform with a 170ms time window. It cannot distinguish between the two Ricker wavelets at 1.07s and 1.1s due to its fixed time-frequency resolution.

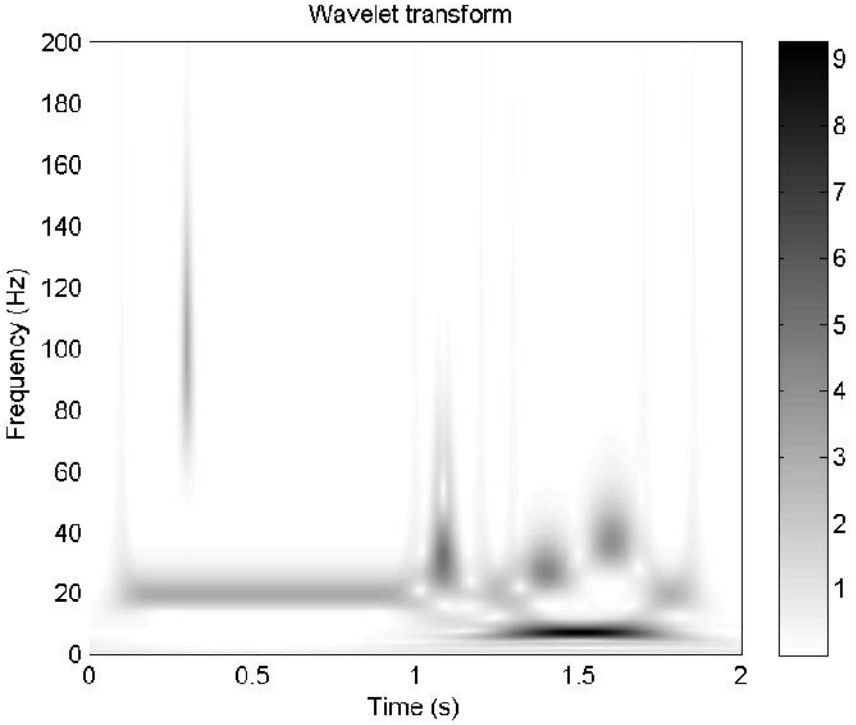

Figure 2.7: Amplitude spectrum after a wavelet transform analysis. It shows a better compromise between time and frequency resolution than the short-time Fourier transform as it distinguishes both Ricker wavelets at 1.1s. Yet, the frequency resolution for the 100Hz Morlet wavelet at 0.3s is poor.

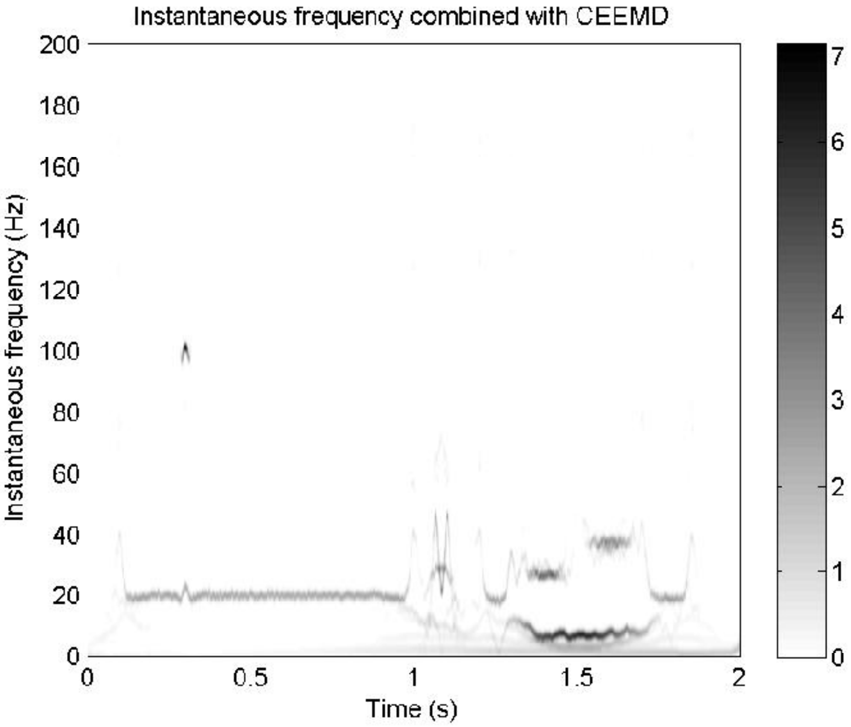

Figure 2.8: Instantaneous amplitude spectrum after CEEMD. It has the highest time-frequency resolution and identifies all individual components. A 6 × 6 Gaussian weighted filter is applied for display purposes.

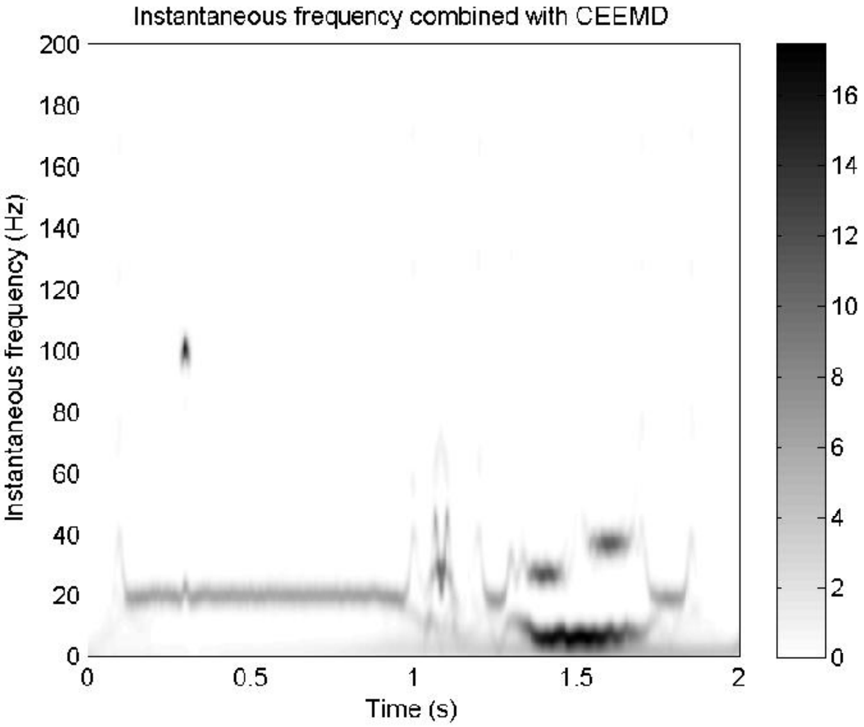

Figure 2.9: Instantaneous amplitude spectrum after CEEMD and a 30 × 30 Gaussian weighted filter. This smoothens the CEEMD result, making it more comparable to Figures 2.6 and 2.7.

2.3.3 Real data

Next we apply the various time-frequency analysis tools on a seismic dataset from a sedimentary basin in Canada. There are Cretaceous meandering channels at 0.42s between CMPs 75-105 and CMPs 160-180, respectively. An erosional surface is located between CMPs 35-50 around 0.4s. The data also contain evidence of migration artifacts (smiles) at the left edge between 0.1s and 0.6s. Note that Van der Baan et al. (2010) have used cumulative energy and local phase attributes to interpret the same data.

First, we take the trace for CMP 81 (Figure 2.11) as an example to show the time-frequency distributions corresponding to the various transforms. The results for the short time Fourier transform with a 50ms time window and the wavelet transform are shown in Figures 2.12 and 2.13, respectively. Both tools show that there are essentially two frequency bands, a lower one between 10-50 Hz persistent at all times, and an upper one that diminishes over time (90 Hz at 0.1s, 70 Hz at 0.5s and 50 Hz at 1s). The reduction in the high-frequency band is most likely due to attenuation of the seismic wavelet.

Instantaneous spectral analysis combined with CEEMD with 10% added Gaussian white noise using 50 realizations (Figure 2.14) provides a much sparser image. It reflects a similar time frequency distribution as the two traditional tools with both the persistent lower frequency band as well as the diminishing upper band visible. The sparser image is helpful for more accurately locating these spectral anomalies, thus facilitating further interpretation.

Next, we pick the peak frequency at each time sample and overlay it onto the original seismic data. Figure 2.15 shows the peak frequency after short time Fourier transform. This image shows smooth and continuous features, including alternately high and low frequency bands between 0.2 and 0.8s due to variations in reflector spacing, and a general decrease in high frequencies, which is associated with attenuation of the seismic wavelet.

Figure 2.15 delineates several interesting features in this dataset. First, the peak frequency attribute highlights the Cretaceous meandering channels at 0.42s, which are characterized by lower frequency content due to their increased thickness. Sec-

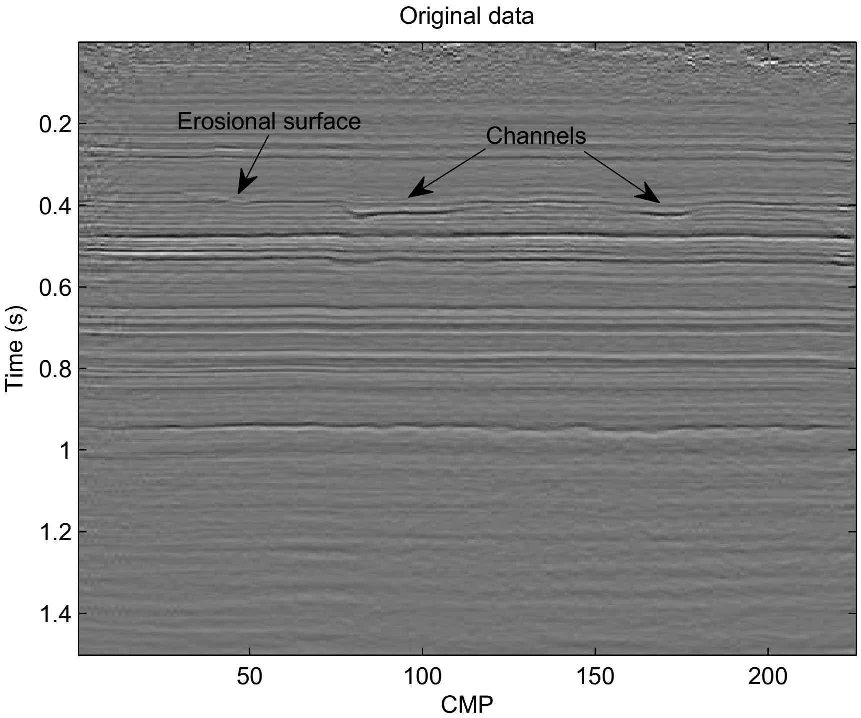

Figure 2.10: Seismic dataset from a sedimentary basin in Canada. The erosional surface and channels are highlighted by arrows. The horizontal axis spans 5.5km.

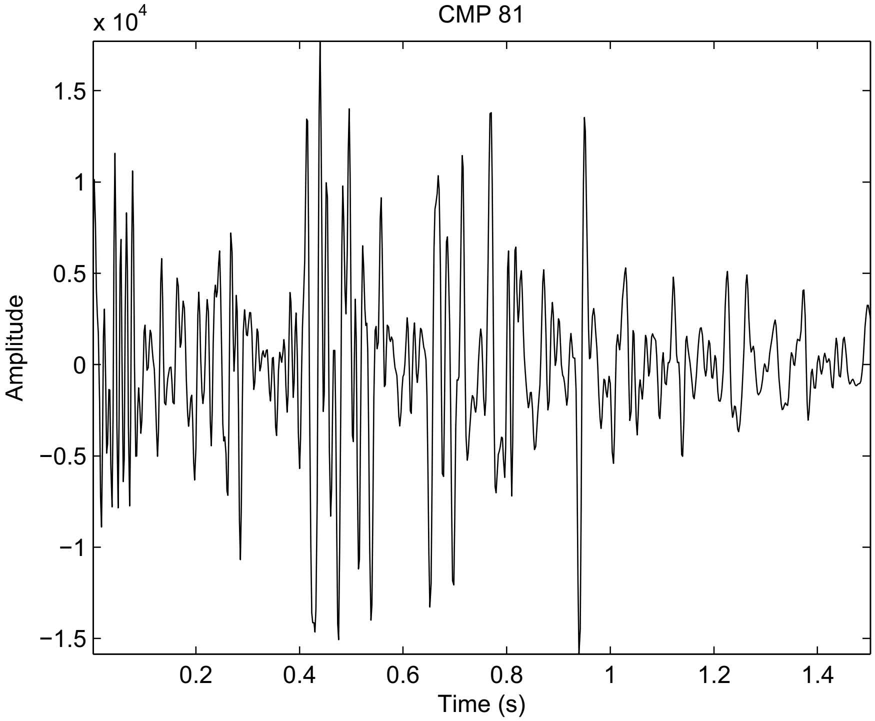

Figure 2.11: Individual trace of CMP 81 in Figure 2.10. The channel is at 0.42s.

ond, it indicates the weakening of the closely spaced reflections (thin layers) around 0.8s. High peak frequencies are clearly visible between CMPs 0-75, followed by predominantly low frequencies due to the thick homogeneous layer underneath. A comparison with the original section (Figure 2.10) shows indeed a reduction in the number of closely spaced reflections from the left to the right around 0.8s, although the migration artifacts visible at the left edge may also influence the high-frequency region to some extent.

As first sight the CEEMD-based peak frequencies seem to be noisier (Figure 2.16). However, the image contains more fine detail compared with the short-time Fourier result (Figure 2.15). Both images delineate the Cretaceous meandering channels around 0.42s. Also the thin-layer reflection at 0.80s is more clearly followed without the abrupt transition to a low-frequency layer at CMP 75 due to the influence of the underlying thick opaque layer. This is a direct result of the higher time resolution of CEEMD combined with computation of instantaneous frequencies. On the other hand, initial inspection of the smoother results for the short-time Fourier

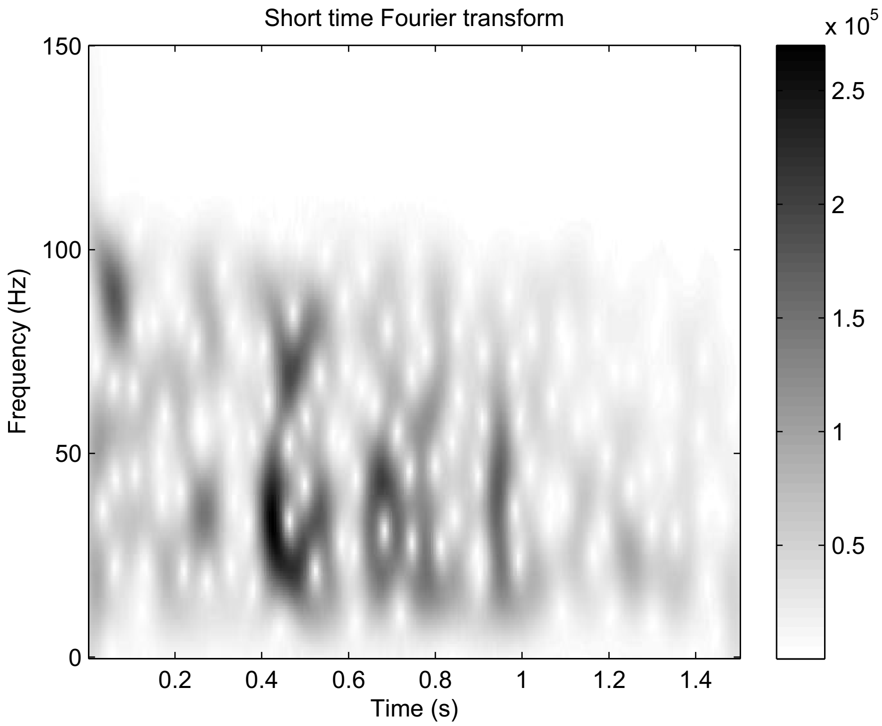

Figure 2.12: Amplitude spectrum for the short time Fourier transform with a 50ms time window for CMP 81. The strong 35 Hz anomaly at 0.42s is due to the channel.

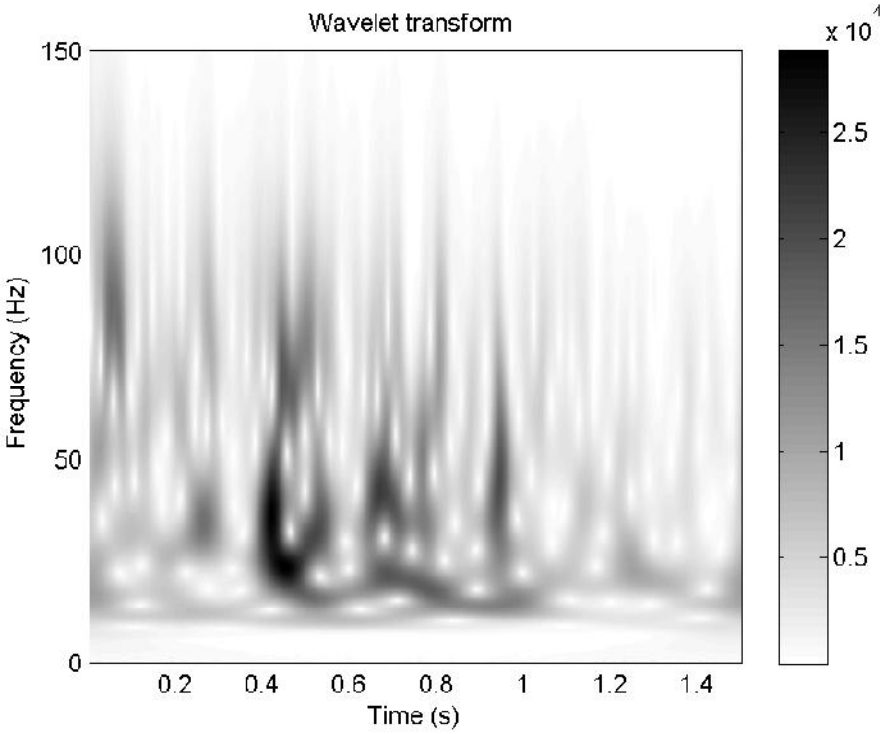

Figure 2.13: Wavelet amplitude spectrum for CMP 81. Vertical stripes at higher frequencies are due to an increased time resolution but poorer frequency resolution. High-frequency content is diminishing over time.

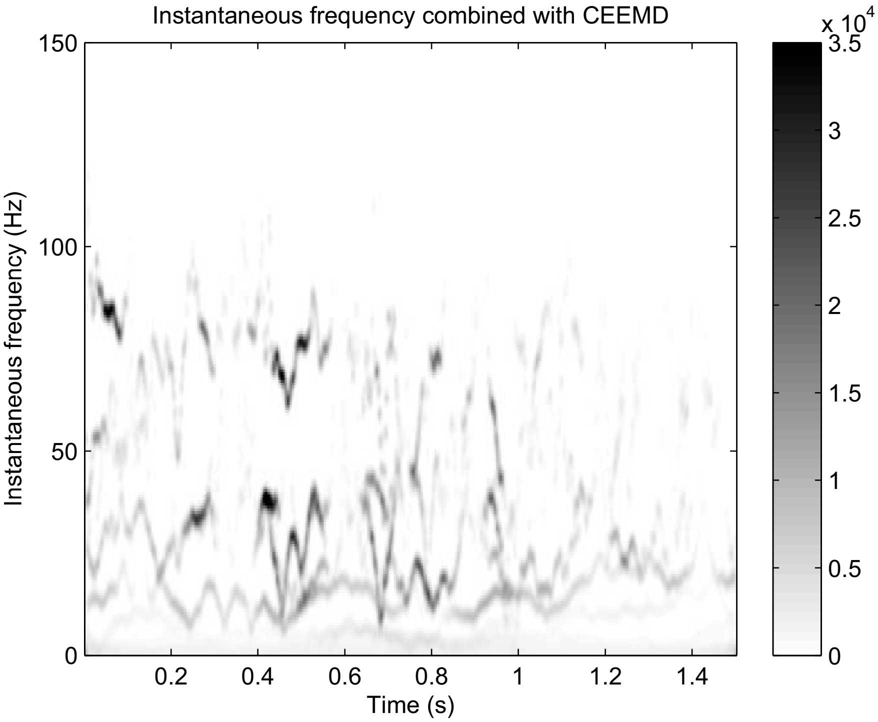

Figure 2.14: Instantaneous amplitude spectrum after CEEMD on CMP 81, displaying the highest time-frequency resolution. Similar features are visible as in Figures 2.12 and 2.13 including the channel at 0.42 s and the diminishing high-frequency content over time.

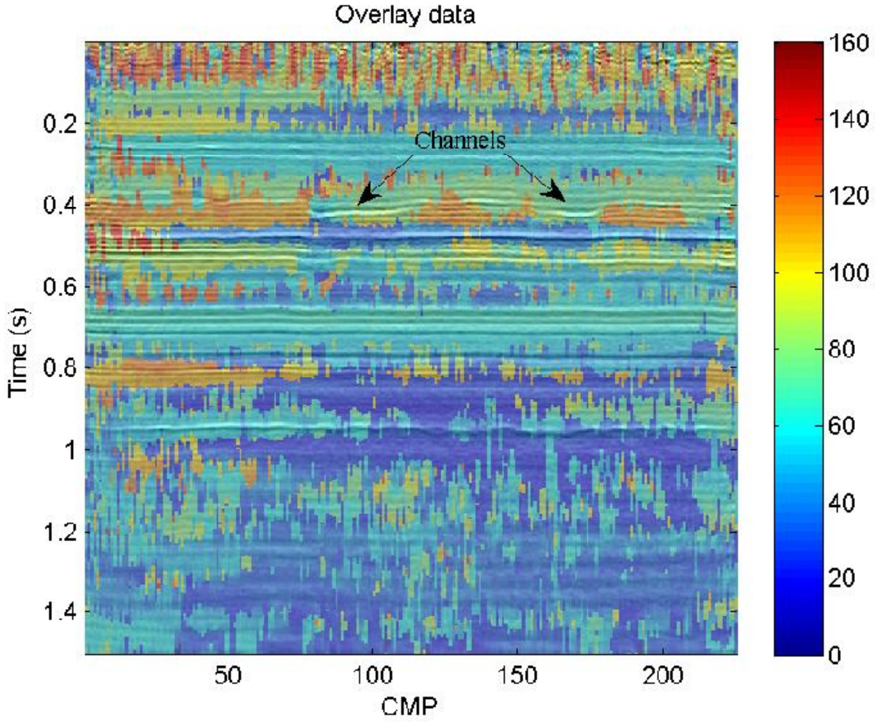

Figure 2.15: Peak frequency attribute after short time Fourier transform. The image highlights variations in reflector spacing, both laterally (channels) and vertically, as well as the gradually decreasing frequency content with depth due to attenuation. The colorbar represents the frequency bands in Hertz (Hz).

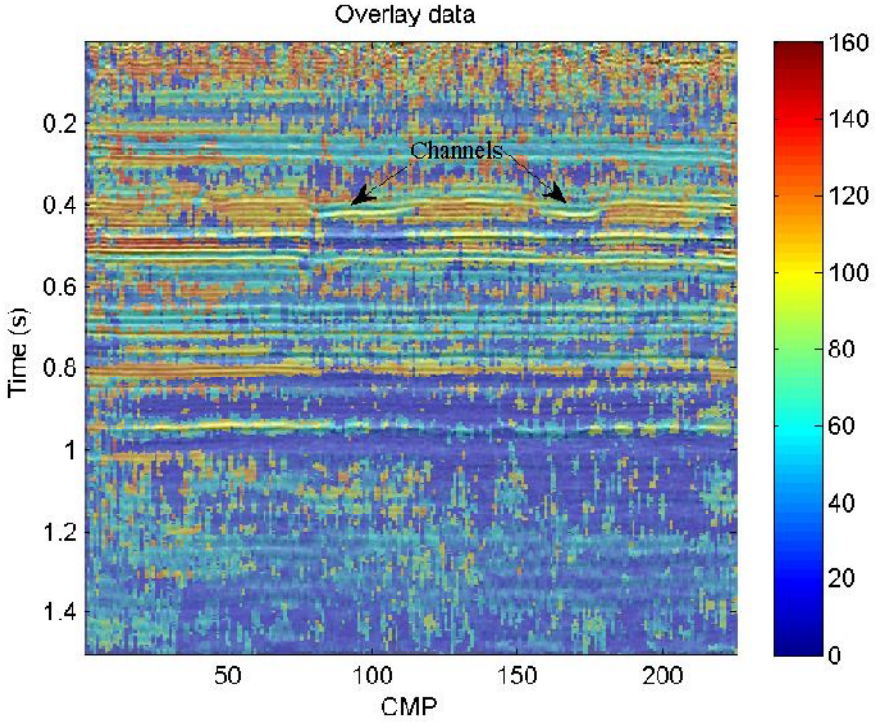

Figure 2.16: Peak frequency attribute from the instantaneous spectrum and CEEMD. A higher time-frequency resolution leads to more spatial and temporal variations but also a sharper delineation of the channels and individual reflection sequences. The colorbar represents the frequency bands in Hertz (Hz).

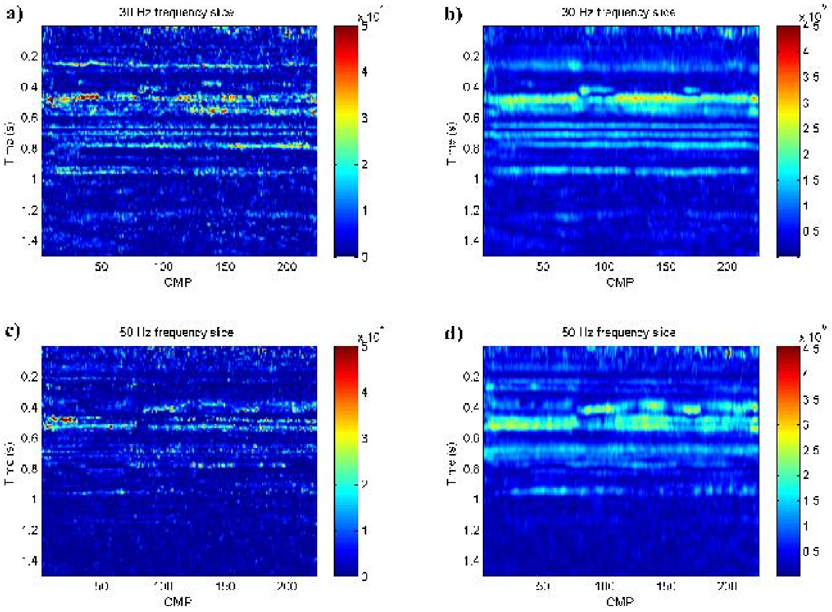

Figure 2.17: Constant-frequency slices. a) 30 Hz CEEMD-based method, b) 30 Hz short time Fourier transform, c) 50 Hz CEEMD-based method, d) 50 Hz short time Fourier transform. The instantaneous spectrum combined with CEEMD shows higher time-frequency resolution than the short time Fourier transform.

transform facilitates interpretation of the CEEMD results. Note that the colorbar in Figures 2.15 and 2.16 represent the frequency bands in Hertz (Hz).

Next, we extract the 30 Hz and 50 Hz frequency slices after CEEMD and short time Fourier transforms (Figure 2.17) to illustrate the higher time-frequency resolution of the CEEMD-based results. The instantaneous spectrum shows much sparser outputs and resolves the spectral characteristics of the various reflections more clearly than the short time Fourier results. This also explains why the Fourier-based peak frequency attribute is more continuous than the CEEMD-based result in Figures 2.15 and 2.16.

Finally, we perform a spectral decomposition of a 3D seismic data volume using both approaches. Figure 2.18 shows a time slice at 420ms displaying both the channel feature, as well as a subtle fault. CEEMD employs again 10% added Gaussian white noise and 50 realizations. A window length of 150ms (75 points) is used for the short time Fourier transform, producing a frequency step of 7 Hz in the spectral decomposition.

Figures 2.19a and 2.19c show respectively the 10Hz and 30Hz spectral slices for the instantaneous spectrum after CEEMD at 420ms. Both the channel and fault are visible, especially at 30Hz. Both spectral slices show similar features; yet there are also clear differences, in particular in the amplitudes of the channel, indicating little spectral leakage across these two frequencies. These amplitude differences are helpful in interpreting thickness variations.

The 10 and 30Hz spectral slices produced by Fourier analysis also show the fault and channel features (Figures 2.19b and 2.19d). However, there are significantly less amplitude variations across both slices as unique frequencies are spaced 7Hz apart due to the short window length and the spectral leakage inherent to the Fourier transform. This renders interpretation of thickness variations in the channel much more challenging as thinning or thickening by a factor two may still produce the same amplitudes across several spectral slices centered on the expected peak frequency. We could have opted for a longer Fourier analysis window, thereby reducing the frequency step in the amplitude spectra. On the other hand, this increases the risk of neighboring reflections negatively biasing the decomposition results. No local analysis window is defined for the CEEMD method thus circumventing this trade off.

2.4 Discussion

Instantaneous frequency can be used to detect and map meandering channels and to determine their thickness (Liu and Marfurt, 2006) as it maps at what frequency maximum constructive interference occurs between the top and bottom channel reflection. However, direct calculation can lead to instantaneous frequencies, which fluctuate rapidly with spatial and temporal location (Barnes, 2007; Han and Van der Baan, 2011).

Saha (1987) discusses the relationship between instantaneous frequency and Fourier frequency, and points out that the instantaneous frequency measured at an envelope peak approximates the average Fourier spectral frequency weighted by the

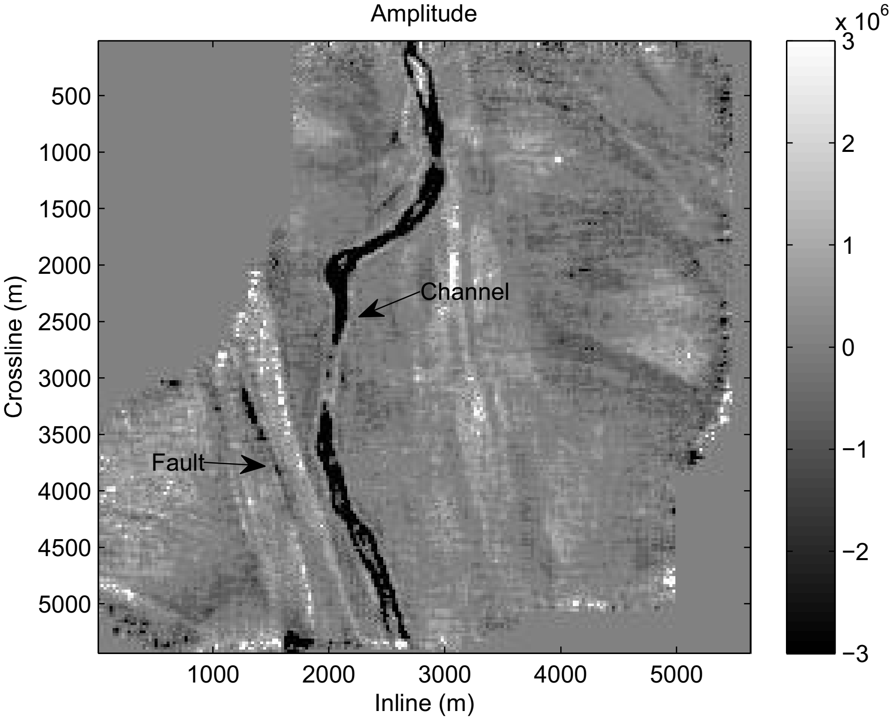

Figure 2.18: Time slice extracted at 420ms. The channel feature is clearly visible as is a subtle fault to its left.

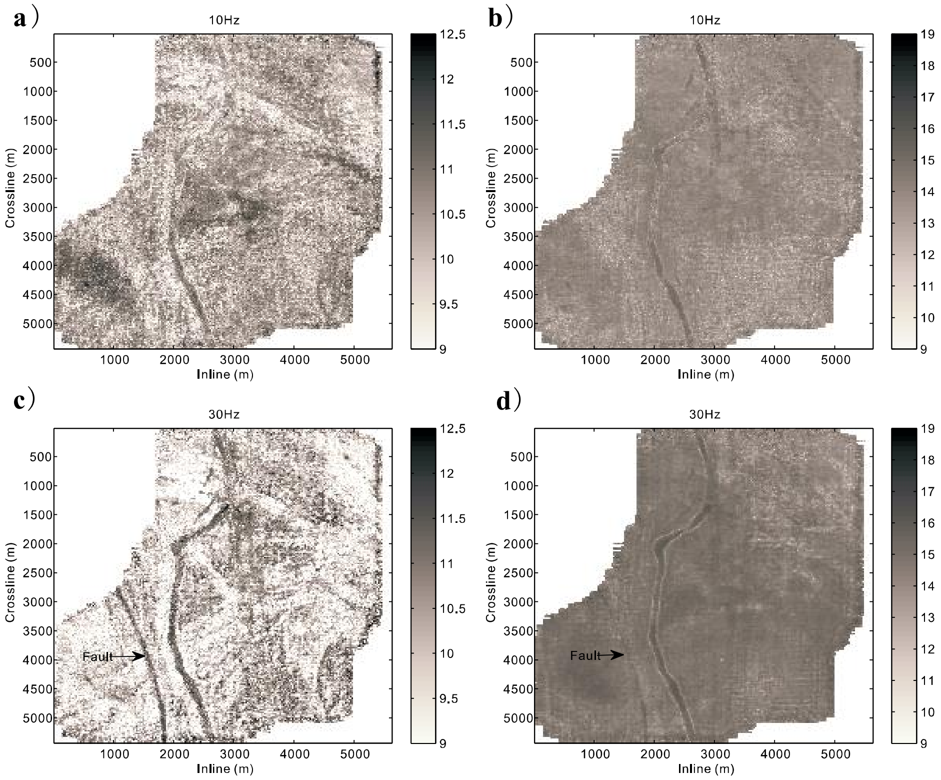

Figure 2.19: Spectral decomposition results: Power spectrum displayed on a logarithmic scale. a) 10Hz - CEEMD; b) 10Hz - Fourier; c) 30Hz - CEEMD; d) 30Hz - Fourier. Both methods show the fault and channel but amplitude variations for the Fourier-based results are much more similar for both spectral slices due limited frequency resolution because of the employed short analysis window and increased spectral leakage.

amplitude spectrum. Huang et al. (2009) summarize the applicability conditions for instantaneous frequency: namely, the time series must be mono-component and narrow band. Analysis of instantaneous frequencies has been gradually replaced by spectral decomposition techniques in the 1990s due to their increased flexibility (Chakraborty and Okaya, 1995; Partyka et al., 1999).

CEEMD successfully overcomes the mode-mixing problem, thus facilitating the analysis of individual IMFs. The subsequent computation of the instantaneous frequency then leads to relatively smoothly varying and positive instantaneous frequencies suitable for time-frequency analysis. In addition, both the synthetic and real data examples show this produces a potentially higher time-frequency resolution than the short time Fourier and wavelet transforms. Window length, overlap and mother wavelet parameters restrict the resolution of short time Fourier and wavelet transforms, and predefined decomposition bases render these two methods less suitable for analyzing non-stationary systems.

The computational cost of CEEMD is proportional to the number of realizations. We use 50 realizations in the real data application to balance computational cost versus satisfactory decomposition results. Broadly speaking we found in our tests that the computational cost of a wavelet transform and CEEMD using 50 realizations are respectively twice and 18 times that of a short time Fourier transform. A single EMD decomposition can thus be faster that a single short time Fourier transform result. Obviously these computation times strongly depend on the implementation and actual parameter settings, yet application of EMD and variants are not prohibitively expensive.

The actual time-frequency resolution of any EMD variant in combination with computation of the instantaneous frequency is to the best of our knowledge still unknown. The uncertainty principle states that it is impossible to achieve simultaneously high time and frequency resolution, as their product is always greater than or equal to a constant. In the short time Fourier transform, the window length causes the tradeoff between time and frequency resolution. Large time windows achieve good frequency resolution at the cost of high time resolution, and vice versa. Conversely wavelet and S-transforms display an inherent trade-off between time and frequency resolution via their variable-size analysis windows (Rioul and Vetterli, 1991; Kumar and Foufoula-Georgiou, 1997).

The instantaneous frequency calculates a frequency value at every time sample, producing the highest possible time resolution but with necessarily very poor frequency resolution. This provides an alternative insight into why negative frequency values are not uncommon. However, instantaneous frequency is not meaningless as the instantaneous frequency measured at an envelope peak approximates the weighted average Fourier spectral frequency, and shows superior results on mono-component and narrow band signals (Saha, 1987; Huang et al., 2009).

Flandrin et al. (2004a) show that EMD acts as a constant-Q bandpass filter for white-noise time series, and the constant-Q bandpass filter means the number of octaves is constant in each bandpass filter. In other words, white noise is divided into IMF components each comprising approximately a single octave. Results by Torres et al. (2011a) imply that CEEMD maintains this property. Given the uncertainty principle, we postulate therefore that the inherent frequency resolution of each individual IMF is one octave with a time resolution inversely proportional to the center frequency of this octave. The obtained IMFs have thus an increasing frequency resolution at the expense of a decreasing time resolution with increasing IMF number. In other words, the first IMF has thus the highest time resolution and the lowest frequency resolution. The opposite is true for the last IMF. Furthermore this implies that temporal fluctuations in the instantaneous frequencies are limited to approximately the reciprocal of the center frequency of the corresponding octave, or to put it differently, all computed instantaneous frequencies are guaranteed to be relatively smooth within their various scale lengths.

The preceding discussion assumes a white-noise signal. For arbitrary signals the performance of CEEMD in combination with instantaneous attributes may retrieve even more accurate and precise time-frequency decompositions if the original trace is comprised of individual mono-component and narrowband signals as the sifting algorithm is designed to extract individual IMFs with precisely such characteristics.

Finally, the main advantages of CEEMD combined with instantaneous frequencies are the implementary simplicity and controllable time-frequency resolution.

There are only two parameters in CEEMD, namely the percentage of Gaussian white noise and the number of noise-realizations.

Neither seems to have a critical influence on final decompositions. Furthermore we can control the time-frequency resolution by the size of the Gaussian weighted filter. Smaller sizes show higher temporal-spectral resolution, and vice versa. It is therefore possible to compute first a decomposition result similar to those of the short-time Fourier and wavelet transforms which can then be reduced for further and more precise analysis, thus allowing for seismic interpretation with controllable time-frequency resolution. The real data example verifies that instantaneous spectrum after CEEMD have higher time-frequency resolution than traditional decompositions. However, the associated peak-frequency attribute may therefore vary more rapidly both spatially and temporally, rendering the interpretation more challenging. Our recommendation is to analyze the principal frequency variations by short time Fourier transform or severely smoothed CEEMD-based instantaneous frequencies first, followed by identification of the subtle changes in geology using the unsmoothed instantaneous spectrum.

2.5 Conclusion

CEEMD is a robust extension of EMD methods. It solves not only the mode mixing problem, but also leads to complete signal reconstructions. After CEEMD, instantaneous frequency spectrum manifest visibly higher time-frequency resolution than short time Fourier and wavelet transforms on both synthetic and field data examples. These characteristics render the technique highly promising for both seismic processing and interpretation.

Chapter 3

Applications of the synchrosqueezing transform in seismic time-frequency analysis[1]

Summary

Time-frequency representation of seismic signals provides a source of information that is usually hidden in the Fourier spectrogram. The short-time Fourier and Wavelet transforms are the principal approaches to simultaneously decompose a signal into its time and frequency components. Known limitations, such as trade-offs between time and frequency resolution, may be overcome by alternative techniques that extract instantaneous modal components. The Empirical Mode Decomposition aims to decompose a signal into components that are well separated in the time-frequency plane allowing the reconstruction of these components. On the other hand, a recently proposed method called ”Synchrosqueezing transform” (SST) is an extension of the Wavelet transform incorporating elements of empirical mode decomposition and frequency reassignment techniques. This new tool produces a well-defined time-frequency representation allowing the identification of instanta-

---

[1] A version of this chapter has been published. Roberto H. Herrera, Jiajun Han and Mirko van der Baan, Geophysics, 2014, 79, 3, V55-V64. My contributions are creating the synthetic data, computing the empirical mode decomposition results, creating the routines for time slice attribute for fix frequency and commenting on the paper.

neous frequencies in seismic signals to highlight individual components. We introduce the SST with applications for seismic signals and produced promising results on synthetic and field data examples.

3.1 Introduction

This chapter is a follow up study of the Empirical Mode Decomposition (EMD) method described by Han and Van der Baan (2013). The Empirical Mode Decomposition method is an effective way to decompose a seismic signal into its individual components, called ”Intrinsic Mode Functions” (IMFs). Each IMF represents a harmonic signal localized in time, with slowly varying amplitudes and frequencies, potentially highlighting different geologic and stratigraphic information.

EMD methods have evolved from EMD to ensemble EMD (Wu and Huang, 2009b) and recently to complete ensemble EMD (CEEMD) (Torres et al., 2011b). These extensions aim to solve the mode mixing problem (Huang et al., 1999, 2003) while keeping the complete reconstruction capability. Han and Van der Baan (2013) investigate the difference between these EMD methods, and discuss the suitability of EMD for seismic interpretation. They conclude that CEEMD not only solves the mode mixing problem but also provides an exact reconstruction of the original signal. In terms of spectral resolution the EMD-based alternatives outperform the short-time Fourier transform (STFT) and the Wavelet transform (WT) methods. Yet, likewise other methods, the top-performing method CEEMD, still has limitations when the components are not well separated in the time-frequency plane.

We extend our studies of time-frequency analysis with a recently proposed transform called Synchrosqueezing (SST) (Daubechies et al., 2011). SST is a wavelet-based time-frequency representation that resembles the EMD method. Unlike EMD, it has a firm theoretical foundation (Wu et al., 2011; Thakur et al., 2013). SST is also an adaptive and invertible transform that improves the readability of a wavelet-based time-frequency map using frequency reassignment (Auger and Flandrin, 1995), by condensing the spectrum along the frequency axis (Li and Liang, 2012b). This transform was originally proposed in the field of audio processing (Daubechies et al.,

2011) and has been successfully applied to paleoclimate time series (Thakur et al., 2013) and to vibration monitoring (Li and Liang, 2012a,b). The SST is still limited by Gabor's uncertainty principle (Hall, 2006), but it approximates the lower limit better, thus improving resolution.

In this chapter, we show the suitability of SST in seismic time-frequency representation. We contrast and compare SST with CEEMD and the continuous wavelet transform (CWT). Our selection of CEEMD as a reference method for comparison is based on its very low reconstruction errors (Torres et al., 2011b) and the fact that it was successfully applied to seismic signal analysis (Han and Van der Baan, 2013), where the instantaneous frequencies are estimated as a posterior step. The CWT is also taken as a reference since SST comprises a combination of this method with frequency reassignment.

In the following section we describe the theory behind EMD and the synchrosqueezing transform. Next, we test the SST on a synthetic example and compare its time-frequency representation and signal reconstruction features with the CWT and CEEMD methods. Finally, we apply SST on field data showing its potential to highlight stratigraphic structures with high precision.

Theory

3.1.1 A brief recap of EMD and siblings

EMD is a fully data-driven method to split a signal into its individual components, called Intrinsic Mode Functions (IMFs) (Huang et al., 1998). Recursive empirical operations (sifting process, see Huang et al. (1998)) separates the signal into high and low oscillatory components. The sum of all the individual components reproduces the original signal. However, some mode mixing appears in the classic EMD method, caused by signal intermittency (Huang et al., 1998), that can produce difficulties in interpreting the resulting time-frequency distribution. This fact triggered the development of the ensemble EMD (EEMD) (Wu and Huang, 2009b), which is based on a noise injection technique. Noise is added prior to decomposition, and ensemble averages are computed for resulting IMFs. This aids in better separation of independent modes but does not guarantee perfect reconstruction.

Despite the improvement in mode separation using the noise-assisted technique, reconstruction from individual components is important and Torres et al. (2011b) proposed an elegant solution. In the CEEMD, an appropriate noise signal is added at each stage of the decomposition producing a unique signal residual for computing the next IMF (Torres et al., 2011b; Han and Van der Baan, 2013). Computation of the instantaneous frequencies for each IMF then produces the desired time-frequency representation (Han and Van der Baan, 2013).

3.1.2 The Synchrosqueezing transform

The SST was originally introduced in the context of audio signal analysis and is shown to be an alternative to Empirical Mode Decomposition (EMD) (Daubechies and Maes, 1996; Daubechies et al., 2011). SST aims to decompose a signal $s(t)$ into constituent components with time-varying harmonic behavior. These signals are assumed to be the addition of individual time-varying harmonic components yielding

$$s(t) = \sum_{k=1}^{K} A_k(t)\cos(\theta_k(t)) + \eta(t), \tag{3.1}$$

where $A_k(t)$ is the instantaneous amplitude, $\eta(t)$ represents the additive noise, K stands for the maximum number of components in one signal, and $\theta_k(t)$ is the instantaneous phase of the k_{th} component. This instantaneous frequency $f(t)$ of the k_{th} component is estimated from the instantaneous phase as:

$$f_k(t) = \frac{1}{2\pi}\frac{d}{dt}\theta_k(t). \tag{3.2}$$

In seismic signals the number K of harmonics or components in the signal is infinite. They can appear at different time slots, with different amplitudes $A_k(t)$, instantaneous frequencies $f_k(t)$ and they may be separated by their instantaneous bandwidths $\Delta f_k(t)$.

The spectral bandwidth defines the spreading around the central frequency, which in our case is the instantaneous frequency; see Barnes (1993) for a completed disentangling of concepts. This magnitude is a constraint for traditional time frequency representation methods. The STFT and the CWT tend to smear the energy of the superimposed instantaneous frequencies around their center frequencies (Daubechies and Maes, 1996). The smearing equals the standard deviation around the central frequency, which is the spectral bandwidth (Barnes, 1993).

SST is able to decompose signals into constituent components with time-varying oscillatory characteristics (Thakur et al., 2013). Thus, by using SST we can recover the amplitude $A_k(t)$ and the instantaneous frequency $f_k(t)$ for each component.

3.1.3 From CWT to SST

The CWT of a signal $s(t)$ is (Daubechies, 1992):

$$W_s(a,b) = \frac{1}{\sqrt{a}} \int s(t)\, \psi^*(\frac{t-b}{a})dt, \tag{3.3}$$

where ψ^* is the complex conjugate of the mother wavelet and b is the time shift applied to the mother wavelet, which is also scaled by a. The CWT is the crosscorrelation of the signal $s(t)$ with several wavelets that are scaled and translated versions of the original mother wavelet. The symbols $W_s(a,b)$ are the coefficients representing a concentrated time-frequency picture, which is used to extract the instantaneous frequencies (Daubechies et al., 2011).

Daubechies et al. (2011) observe that there is a limit to reduce the smearing effect in the time-frequency representation using the CWT. Equation 4.3 can be rewritten using Plancherel's theorem, energy in time domain equals energy in the frequency domain, i.e. Parseval's theorem in the Fourier domain:

$$W_s(a,b) = \frac{1}{2\pi} \int \frac{1}{\sqrt{a}}\, \hat{s}(\xi)\; \hat{\psi}^*(a\xi)\; e^{ib\xi}\; d\xi, \tag{3.4}$$

where $i = \sqrt{-1}$, ξ is the angular frequency, and $\hat{\psi}(\xi)$ is the Fourier transform of $\psi(t)$. The scale factor a modifies the frequency of the wavelet $\hat{\psi}^*(a\xi)$, by stretching and squeezing it. Also, the time shift b is represented by its Fourier pair $e^{ib\xi}$. The convolution in equation 3.3 becomes multiplication in the frequency domain in equation 3.4. Considering the simple case of a single harmonic signal $s(t) = A\cos(\omega t)$ with Fourier pair $\hat{s}(\xi) = \pi A[\delta(\xi - \omega) + \delta(\xi + \omega)]$, equation 3.4 can then be transformed into:

$$\begin{aligned} W_s(a,b) &= \frac{A}{2} \int \frac{1}{\sqrt{a}} \left[\delta(\xi - \omega) + \delta(\xi + \omega)\right] \hat{\psi}^*(a\xi)\, e^{ib\xi}\, d\xi, \\ &= \frac{A}{2\sqrt{a}}\, \hat{\psi}^*(a\omega)\, e^{ib\omega}. \end{aligned} \tag{3.5}$$

In the frequency plane, if the wavelet $\hat{\psi}^*(\xi)$ is concentrated around its central frequency $\xi = \omega_0$, then $W_s(a,b)$ will be concentrated around the horizontal line $a = \omega_0/\omega$ (the ratio central frequency of the wavelet to the central frequency of the signal). However, what we actually get is that $W_s(a,b)$ often spreads out along the scale axis leading to a blurred projection in time-scale representation. This smearing mainly occurs in the scale dimension a, for constant time offset b (Li and Liang, 2012a). Daubechies and Maes (1996) show that if smearing along the time axis can be neglected, then the instantaneous frequency $\omega_s(a,b)$ can be computed as the derivative of the WT at any point (a,b) with respect to b, for all $W_s(a,b) \neq 0$:

$$\omega_s(a,b) = \frac{-i}{2\pi W_s(a,b)} \frac{\partial W_s(a,b)}{\partial b}. \tag{3.6}$$

The final step in the new time-frequency representation is to map the information from the time-scale plane to the time-frequency plane. Every point (b,a) is converted to $(b, \omega_s(a,b))$, and this operation is called synchrosqueezing (Daubechies et al., 2011). Because a and b are discrete values we can have a scaling step $\Delta a_k = a_{k-1} - a_k$ for any a_k where $W_s(a,b)$ is computed. Likewise, when mapping from the time-scale plane to the time-frequency plane $(b,a) \rightarrow (b, w_{inst}(a,b))$, the SST $T_s(w,b)$, is determined only at the centers ω_l of the frequency range $[\omega_l - \Delta\omega/2, \omega_l + \Delta\omega/2]$, with $\Delta\omega = \omega_l - \omega_{l-1}$:

$$T_s(\omega_l, b) = \frac{1}{\Delta\omega} \sum_{a_k : |\omega(a_k,b) - \omega_l| \leq \Delta\omega/2} W_s(a_k, b) a^{-3/2} \Delta a_k. \tag{3.7}$$

The above equation shows that the new time-frequency representation of the signal $T_s(\omega_l, b)$ is synchrosqueezed along the frequency (or scale) axis only (Li and Liang, 2012a). The synchrosqueezing transform reallocates the coefficients of the CWT to get a concentrated image over the time-frequency plane, from which the instantaneous frequencies are then extracted (Wu et al., 2011).

Following Thakur et al. (2013), the discretized version of $T_s(\omega_l, b)$ in equation (3.7) is represented by $\tilde{T}_{\tilde{s}}(w_l, t_m)$, where t_m is the discrete time $t_m = t_0 + m\Delta t$ with Δt the sampling rate and $m = 0, ..., n-1$; n is total number of samples in the discrete signal $\tilde{s}_m$. More special considerations are described in Thakur et al. (2013). The reconstruction of the individual components s_k from the discrete synchrosqueezed transform $\tilde{T}_{\tilde{s}}$ is then the inverse CWT over a small frequency band $l \varepsilon L_k(t_m)$ around the k_{th} component:

$$s_k(t_m) = 2C_{\phi}^{-1} \mathfrak{Re} \left(\sum_{l \varepsilon L_k(t_m)} \tilde{T}_{\tilde{s}}(w_l, t_m) \right), \tag{3.8}$$

where C_{ϕ} is a constant dependent on the selected wavelet. As we take the real part $\mathfrak{Re}$ of the discrete SST in that band, we recover the real component s_k. In this chapter we follow Thakur et al. (2013) where the reconstruction is done by a standard least-squares ridge extraction method; different approaches are explored by Meignen et al. (2012).

3.1.4 Parameter selection

The wavelet choice is a key issue in synchrosqueezing-based methods (Meignen et al., 2012). In SST we first construct the time-frequency map through a CWT, thus we need a mother wavelet that satisfies the admissibility condition (i.e. finite energy, zero mean and bandlimited). At the same time the wavelet must be a good match for the target signal (Mallat, 2008). By definition the wavelet coefficients are the correlation coefficients between the target signal and dilated and translated versions of a given basic pattern (Daubechies, 1992). In our implementation we use a Morlet wavelet with central frequency and bandwidth estimated from the seismic signal.

The other parameter of interest is the wavelet threshold γ. It effectively decides the lowest usable magnitude in the CWT (Thakur et al., 2013). It is a noise-based hard thresholding that Thakur et al. (2013) set to 10^{-8} for the ideal noiseless case in double precision machines. In real cases, when the noise level is unknown, it is common practice to use the finest scale of the wavelet decomposition (Donoho, 1995) as the noise variance σ_η^2. This threshold works in real signals as a noise-level adaptive estimator (Herrera et al., 2006) and is defined as the median absolute deviation (MAD) of the first octave (Donoho, 1995; Thakur et al., 2013):

$$\sigma_\eta = median(|W_s(a_{1:n_v}, b) - median(W_s(a_{1:n_v}, b))|)/0.6745, \tag{3.9}$$

where $W_s(a_{1:n_v}, b)$ is finest scale wavelet coefficients and 0.6745 is a normalizing factor being the MAD of a Gaussian distribution. The threshold is then weighted by the signal length n to be asymptotically optimal with value $\gamma = \sqrt{2\log n} \cdot \sigma_\eta$.

3.2 Examples

3.2.1 Synthetic data

In this section, we test the SST with a challenging synthetic signal (Figure 3.1). This is the same synthetic example used by Han and Van der Baan (2013). The signal is comprised of an initial 20 Hz cosine wave, with a 100 Hz Morlet atom at 0.3 s, two 30 Hz zero-phase Ricker wavelets at 1.07 s and 1.1 s, and three different frequency components between 1.3 s and 1.7 s of, respectively, 7, 30 and 40 Hz. Note the 7 Hz frequency component is split into three parts less than a full period each, appearing at 1.37 s, 1.51 s and 1.65 s.

Figure 3.2 shows the CWT, CEEMD and SST time-frequency representations. For comparison purposes we include the CWT result, because the SST is an extension of the CWT. The STFT is known to have suboptimal performance, as is shown in Figure 6 in Han and Van der Baan (2013). In Han and Van der Baan (2013), a 2D Gaussian smoothing filter (6 × 6 samples) was applied to the CEEMD output to improve visualization. In our example, we plot the actual outputs from each method, because the objective is to show the sharpness of the reconstructed instantaneous frequencies.

CWT uses a Morlet mother wavelet and a total of 320 scales (32 voices per octave) to provide the time-frequency map shown in Figure 3.2(a). Note that this is the same result as in Figure 7 of Han and Van der Baan (2013) with a different color scale. Here, we have added a graphical interpretation to illustrate how the synchrosqueezed representation is derived from the CWT. The dashed white line in the vicinity of 20 Hz in Figure 3.2(a) is the ridge obtained from the instantaneous frequency in the wavelet domain from equation 3.6. The next step involves the reassignment of the CWT values to the position indicated by the instantaneous frequency w_l in equation 3.7. This mapping process indicated by vertical arrows moves each point (b,a) to the location $(b,w_{inst}(a,b))$ producing a new time frequency representation that is shown in Figure 3.2(c). CEEMD (Figure 3.2(c)) uses 10 % of injected Gaussian white noise and 100 realizations. The result obtained by the SST (Figure 3.2(c)) uses, likewise, the CWT from which it was generated, a Morlet wavelet, and 32 voices per octave.

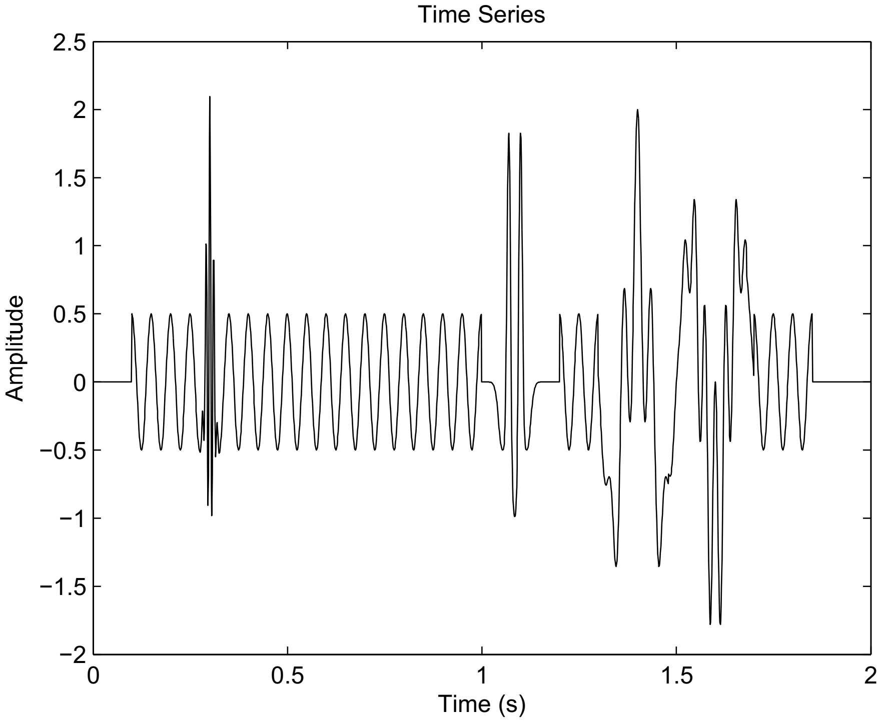

Figure 3.1: synthetic example: background 20 Hz cosine wave, superposed 100 Hz Morlet atom at 0.3 s, two 30 Hz Ricker wavelets at 1.07 s and 1.1 s, and there are three different frequency components between 1.3 s and 1.7 s. Same as Figure 1 in Han and Van der Baan (2013).

CEEMD and SST delineate the individual components equally well, especially, the instantaneous frequencies for the harmonic signals are well resolved. Yet, CEEMD collapses the short 100 Hz Morlet wavelet at 0.3 s more. The 7, 30 and 40 Hz frequency components occurring between 1.3 s and 1.7 s are resolved by both methods, but there is little indication that the 7 Hz component is not continuous. SST and CEEMD show only minor differences, but both display significantly less frequency smearing than the CWT representation.

Unlike the CWT, SST and CEEMD allow for the extraction of the individual components. Here we compare the performance of both methods in extracting and reconstructing the modes in a signal. To evaluate numerically the reconstruction error, for both decompositions, we use the difference between the original signal and the sum of the modes (Torres et al., 2011b). A more general metric based on the mean square error (MSE) is used to score reconstruction with a single value as:

$$MSE = \frac{1}{N} \sum_{n=0}^{N-1} |s(t) - \hat{s}(t)|^2, \tag{3.10}$$

where N is the number of samples, $s(t)$ is the original signal and $\hat{s}(t)$ is the reconstructed signal from the sum of all modes.

Figure 3.3 shows the Intrinsic Mode Functions (IMFs) extracted with the CEEMD. The CEEMD decomposition is able to unmix each individual component giving an easily interpretable decomposition. On the other hand, the SST method (Figure 3.4) shows some degree of mode mixing of the components.

For the CEEMD method, the first IMF shows the 100 Hz Morlet atom, which is also identified by SST IMF1, but SST also recovers parts of the 30 Hz Ricker wavelets. IMF2 of both methods are the residuals of the high frequency components. IMF3 of the CEEMD represents the higher oscillations in the upper band of the Ricker wavelets, whereas IMF3 of the SST shows directly the 30 Hz Ricker wavelets plus the 30 and 40 Hz component. For IMF4, the SST method performs equally well as the CEEMD does, but includes the 20 Hz component between the two 30 Hz. IMF5 of the CEEMD shows the 20 Hz component with some mixtures of the 30 Hz Ricker wavelets, whereas the SST shows a better representation of the 20 Hz with

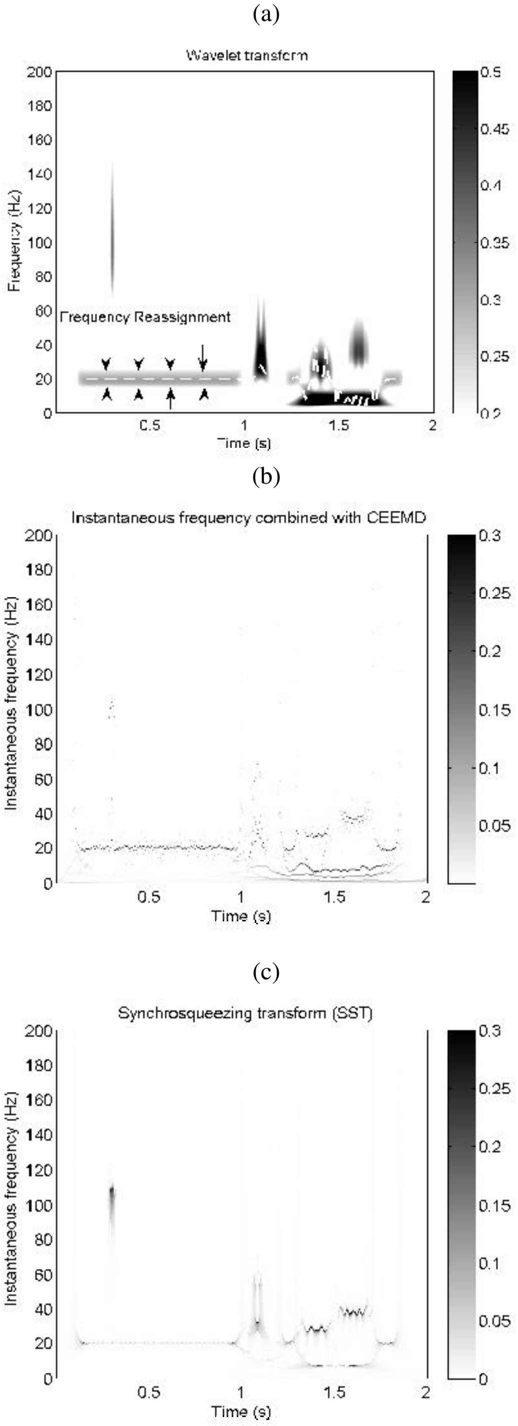

Figure 3.2: Time-frequency representation of the synthetic trace. (a) CWT, displaying smearing along the frequency axis for the harmonic signals. (b) CEEMD output with 10 % added Gaussian white noise and 100 realizations. The instantaneous frequencies corresponding to individual components are well delineated. (c) SST output, with similar results for the harmonics as CEEMD.

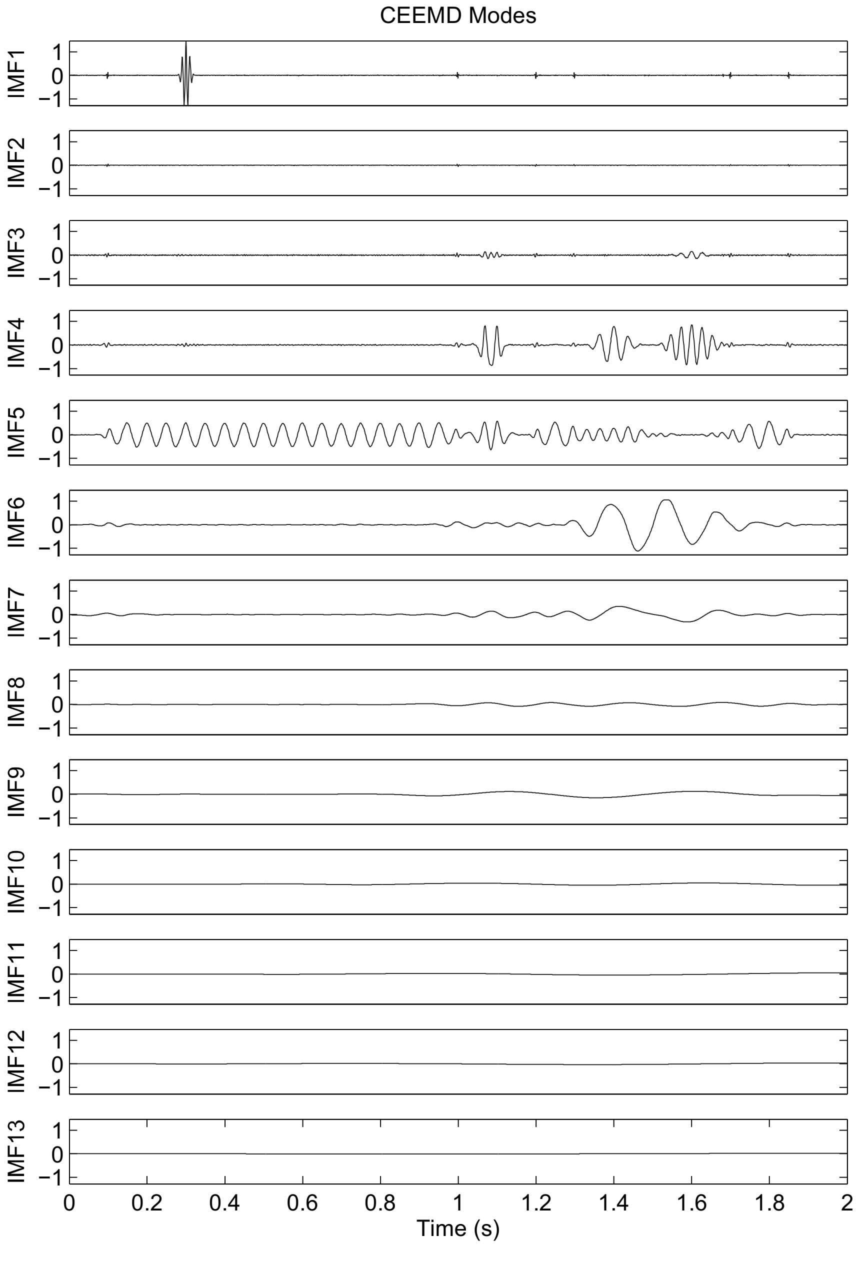

Figure 3.3: Decomposition of the original signal, shown in Figure 3.1, into its intrinsic modes by CEEMD. The decomposition gives 13 individual modes with little mode mixing.

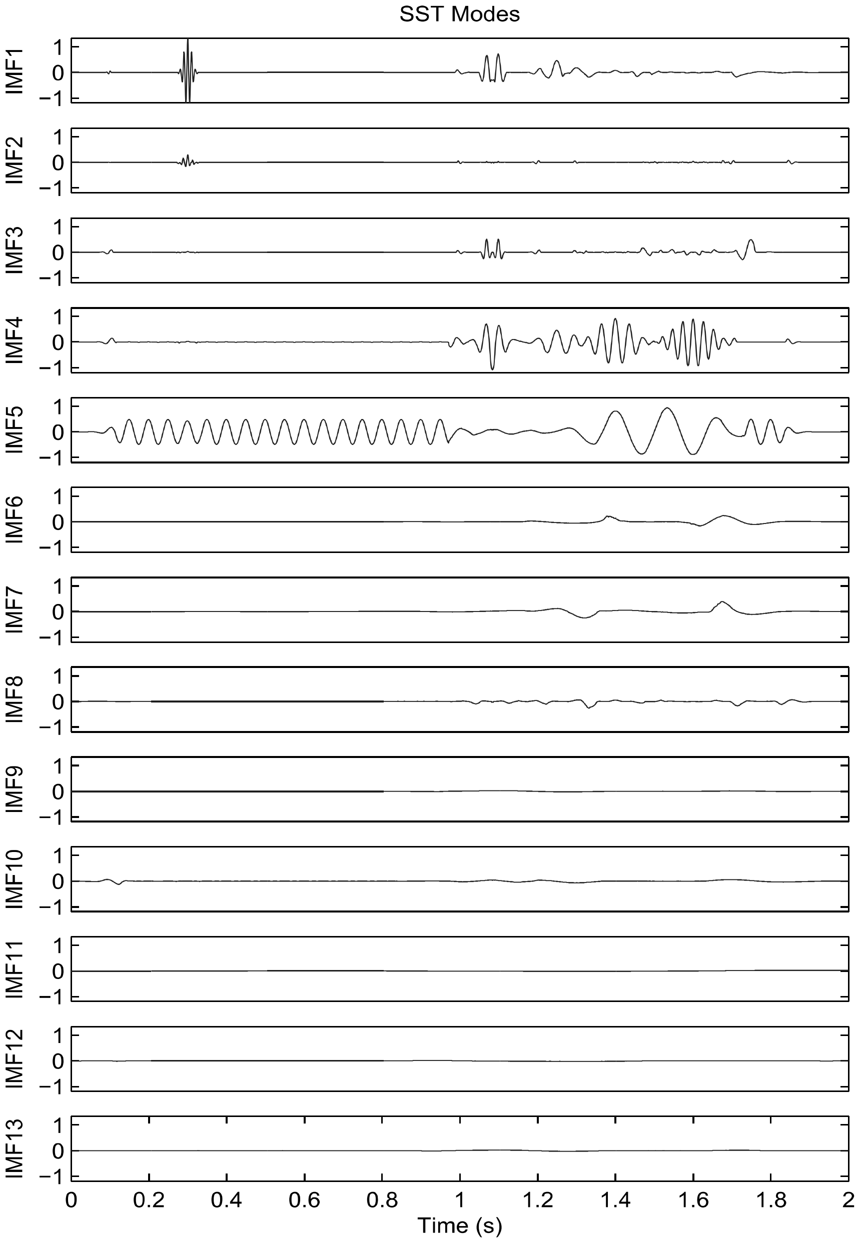

Figure 3.4: Decomposition of the original signal, shown in Figure 3.1, into its intrinsic modes by SST. We use the same 13 levels to compare to CEEMD output. While the decomposition is able to isolate the individual components, still some degree of mode mixing is appreciable in the SST components.

the 7 Hz mode. IMF6 is only informative for CEEMD with an isolated 7 Hz mode. The remainder are small-valued elements. These low-amplitude components in the CEEMD method are low-amplitude frequency bands, derived during the sift- ing process. IMFs are derived from the highest oscillating components to the lower frequency ones. Like the Fourier transform, some IMFs will have higher amplitudes than other components depending on the signal characteristics. This is visible in Figure 3.3, where the second IMF has not only a different frequency content from IMF 1 and 3, but also a different maximum amplitude.

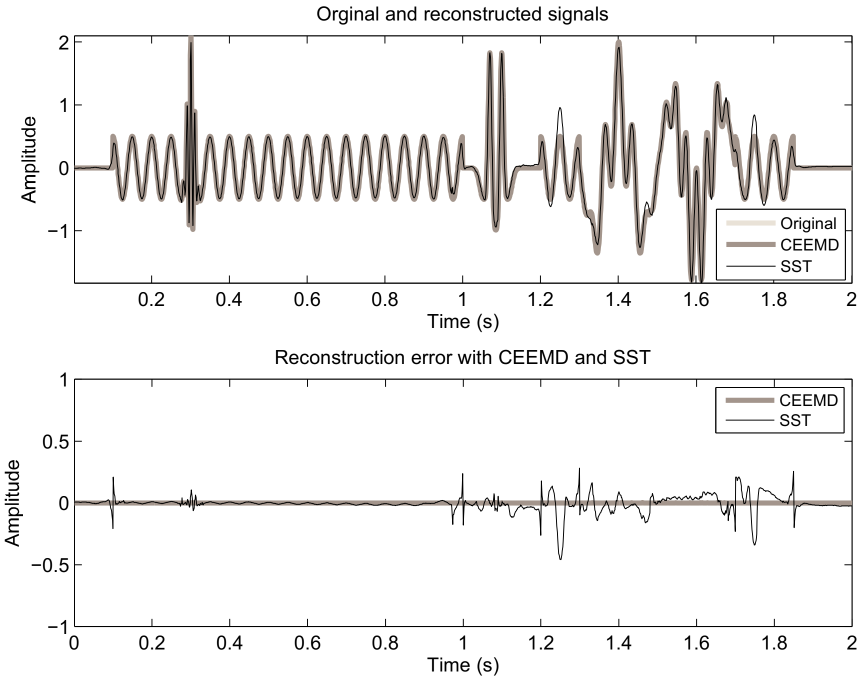

Figure 3.5: Reconstructed signals and reconstruction errors. Top left shows the CEEMD estimate (blue) over the original signal (red); there is no appreciable difference between these two signals. The reconstruction error is approximately zero, limited by the machine precision in the order of 10^{-16} (top right). Bottom row: SST produces a reasonable reconstruction especially for the stationary parts with an MSE value of 0.0013.

The reconstructed signals by both methods are shown in Figure 3.5. CEEMD (top dotted gray) does a perfect reconstruction subjected only to machine precision with an overall MSE value of 5x10^{-33} and a negligible reconstruction error as is shown in the bottom plot. The SST method provides a good estimation (top continuous line) but some areas are not reconstructed accurately, especially in the amplitudes, as is shown in the bottom plot (continuous line). The MSE for the SST is 0.0013, which is in the range of what is considered a good performance for a reconstruction method (Meignen et al., 2012).

3.2.2 Application to real seismic signals

Single trace

In this section we apply the SST to a real dataset and compare to the CWT and CEEMD methods. This is a data set from a sedimentary basin in Canada (Figure 3.6), also analyzed by Han and Van der Baan (2013) and Van der Baan et al. (2010). It contains a Cretaceous meandering channel at 0.42 s between common mid points (CMPs) 75-105 and a second channel between CMPs 160-180 of this migrated 2D cross-section. An erosional surface is located between CMPs 35-50 around 0.4 s. The data also contain evidence of migration artifacts (smiles) at the left edge between 0.1 s and 0.6 s. There are bands of alternating high-frequency areas with tightly spaced reflections and low-frequency regions, which are mostly composed of blank intervals without much reflected energy (Van der Baan et al., 2010). This makes this data set interesting for testing time-frequency decomposition algorithms. It has been shown that both channel intersections exhibit significantly lower frequency content due to their increased thickness (Van der Baan et al., 2010), causing constructive interference in the low-frequency components (Partyka et al., 1999).

We take the seismic trace at CMP 81, which is plotted in Figure 3.7, and apply CWT, CEEMD and SST as is shown in Figure 3.8. CWT and SST is based on a Morlet wavelet with 32 voices per octave. CEEMD employs 10 % of added Gaussian white noise and 50 realizations.

All time-frequency representations display some similar features including the bright channel at 0.42s and a decrease in frequency content with time, most likely due to attenuation (Figure 3.8). SST and CEEMD show more features than the CWT, due the higher time-frequency resolution of both methods. SST and CEEMD representations generally agree for the frequencies above 50 Hz but connect strong

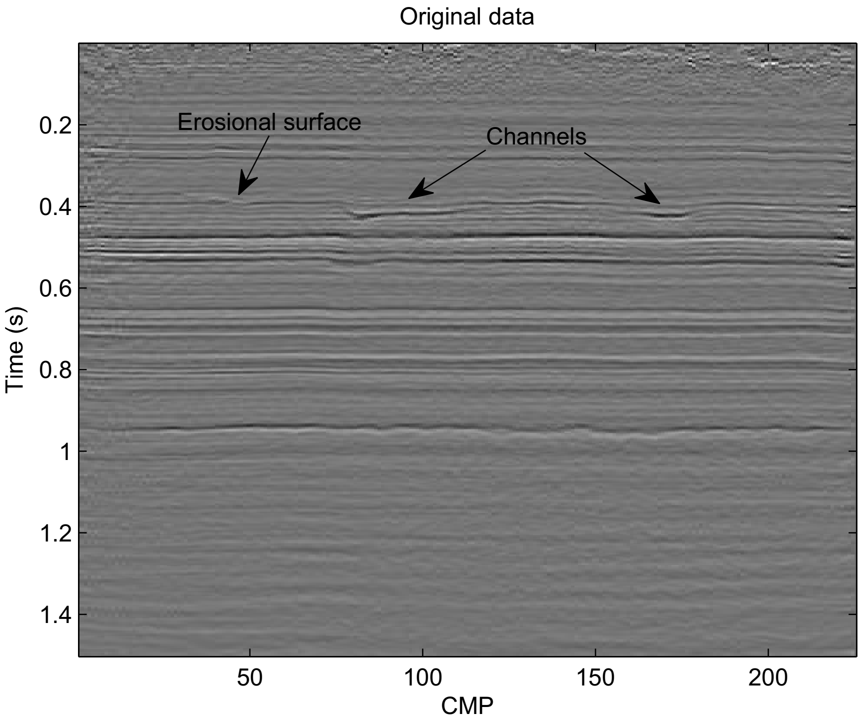

Figure 3.6: Seismic dataset from a sedimentary basin in Canada. The erosional surface and channel sections are highlighted by arrows. Same data as in Figure 10 of Han and Van der Baan (2013).

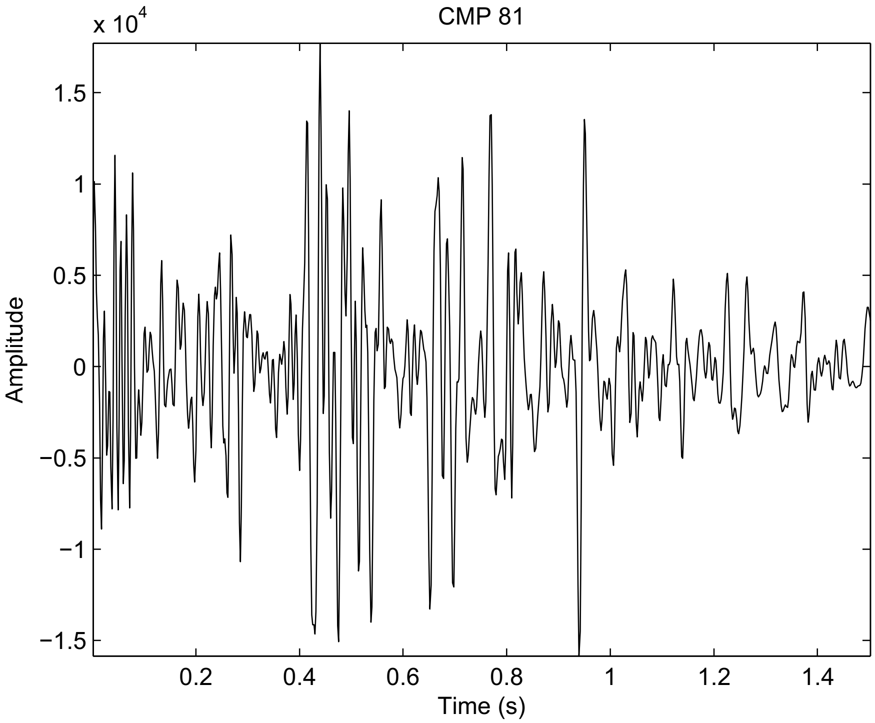

Figure 3.7: Individual trace at CMP 81 in Figure 3.6. It crosses the channel at 0.42 s.

spectral peaks differently for the lower frequencies. This demonstrates the value in examining a single time series using various time-frequency analysis methods.

Vertical cross-section

Next we apply the three methods to all traces and compute the frequency where the cumulative spectral energy is at 80 % (C80) of the total energy (Van der Baan et al., 2010). Our motivation to use this cumulative energy criterion comes from the fact that frequency-dependent thning effects are often analyzed using spectral decomposition to detect variations in turbidite layer or meandering channels (Partyka et al., 1999; Van der Baan et al., 2010). Low-frequency values in C80 indicate concentrations of energy near the lower portion of the total bandwidth, whereas high-frequency values imply a broader spectrum. In some cases, lower values will thus indicate areas of larger attenuation of the propagating wavelet. In other situations, it can reveal shifts in the position of a single notch in the locally observed wavelet, for instance, due to a thickening or thinning of reflector spacing (Van der Baan et al.,

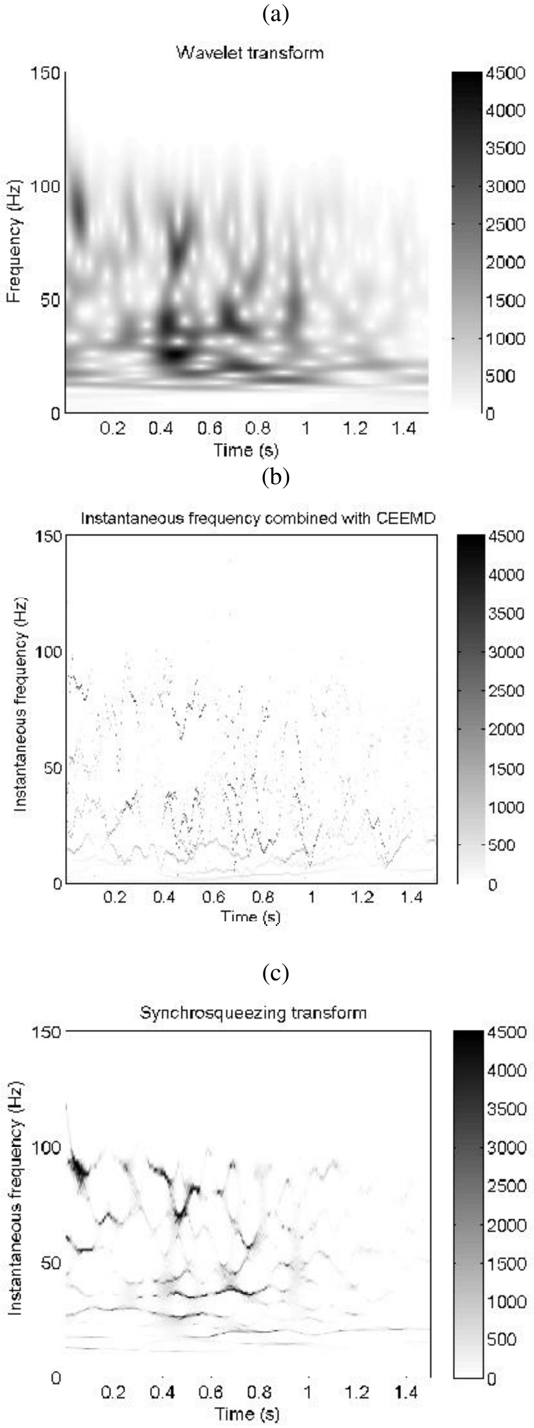

Figure 3.8: CMP 81. Time-frequency representation from (a) CWT, (b) CEEMD and (c) SST. All show a decrease in frequency content over time; yet the CEEMD and SST results are least smeared.

2010).

This frequency attribute is overlayed onto the original seismic data shown in Figure 3.6. Figure 3.9 shows the CWT, CEEMD and SST results. The colorbar represents the frequency bands in Hertz (Hz). This frequency representation from three methods shows high and low frequency bands between 0.2 and 0.8 s due to variations in reflector spacing, and a general decrease in high frequencies, which is associated with attenuation of the seismic wavelet.

The CWT C80 representation, shown in Figure 3.9a, brings out a broader picture of the spectral content of this spatial location; the mayor features are indicated. The CEEMD result emphasizes the most interesting features in the dataset. Traces on the Cretaceous meandering channels at 0.42 s, have lower frequency content than the neighboring traces. This low-frequency variation is due to the increased thickness in the channels. The SST result exhibits an even cleaner representation (Figure 3.9c). The thin layers around 0.8 s are equally well identified by all methods, but less speckle like patterns are observed below this reflector in the CEEMD and SST images. The strong uniform reflector at 0.9 s is better represented by the SST method.

Horizontal slice

In our last test, we run the three algorithms on the entire seismic cube, composed by 225 inlines, 217 crosslines with a regular spacing of 25 m. Each trace is 450 samples long with a sampling frequency of 500 Hz. Figure 3.10 shows the time slice at 420 ms of the seismic cube. Beside the channel feature, which is clearly shown throughout the image, there is a subtle fault. We compare the results of CWT, CEEMD and SST centered at this time slice analyzing different frequency slices. CWT and SST use a Morlet wavelet with 32 levels per octave, and CEEMD injects 10 % of Gaussian white noise using 50 realizations.

Figure 3.11 shows the resulting constant frequency slices for CWT (a), CEEMD (b) and SST (c) at, respectively 20, 40 and 60 Hz (top to bottom). The channel and fault are more sharply represented by CEEMD and SST than in the CWT maps. CEEMD and SST have similar performance, however only SST seems to show that

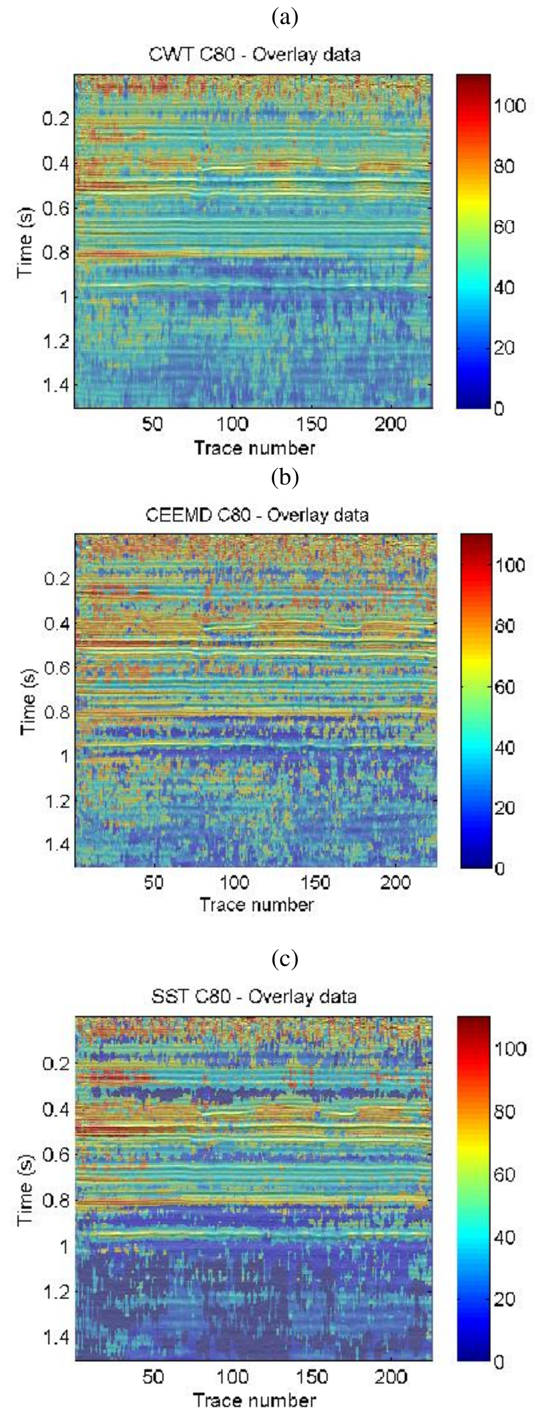

Figure 3.9: Characteristic frequencies for vertical cross-section. C80 attribute for (a) CWT, (b) CEEMD, and (c) SST. CEEMD and SST show a sparser representation than the CWT. SST has even less speckle noise and the strong reflector at 0.9 s is better represented. The colorbar represents the frequency bands in Hertz (Hz).

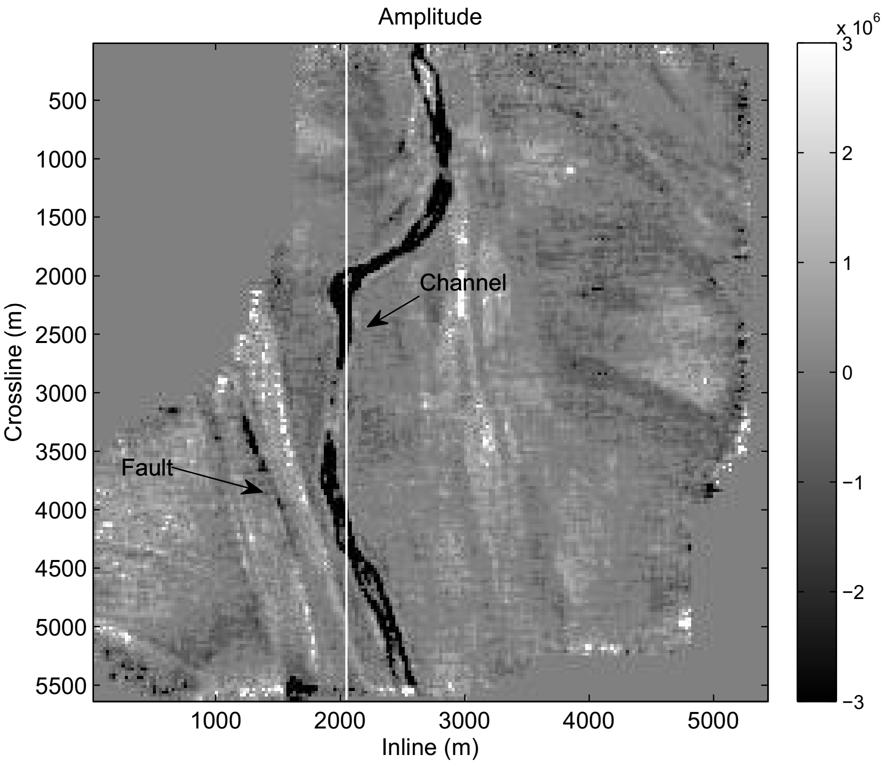

Figure 3.10: Time slice at 420 ms. The channel feature and fault are clearly visible.

the 60 Hz spectrum is fading.

The fault appears at the 40 Hz and 60 Hz time slices of all three methods. The CWT shows the main features on all three frequency slices; yet their amplitude variations are less clear, which makes the thickness calculation of the channel challenging during the further interpretation. Compared with CWT, the amplitude variation of CEEMD and SST along the channel is better defined, which is helpful to calculate subtle thickness variations. The amplitude variations between closely spaced frequencies are better resolved in the CEEMD and SST result due to significantly reduced frequency smearing and smaller spectral leakage than for the CWT and STFT methods (Han et al., 2013). In addition, the CWT depicts a rather homogeneous area in the zone to the right of the channel in all frequency slices, whereas the CEEMD and SST results show more variable magnitudes with areas of localized amplitude strengthening and weakening plus several linear features.

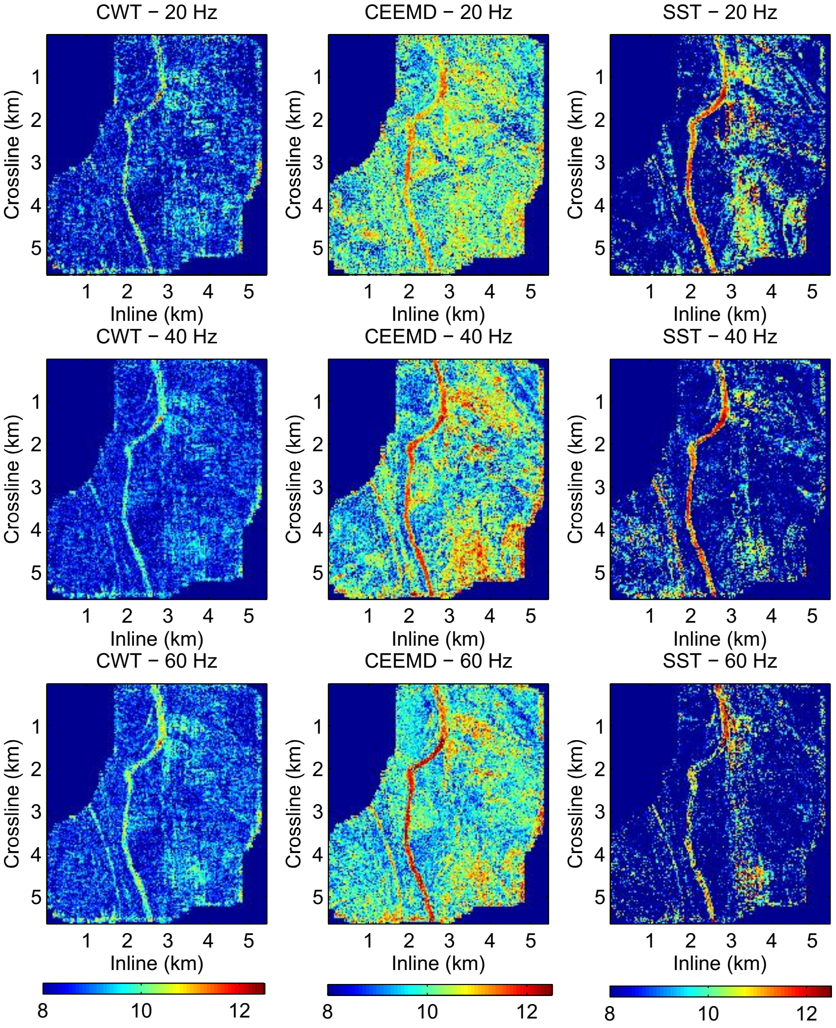

Figure 3.11: Constant-frequency slices. Left column shows from top to bottom the CWT outputs for 20 Hz, 40 Hz and 60 Hz, respectively. The center column is the corresponding instantaneous spectrum estimated by CEEMD. The SST output is shown in the right column.

3.3 Discussion

SST can be used to accurately map time domain signals into their time-frequency representation. It has a well grounded mathematical foundation which facilitates theoretical analysis. Like the alternative methods it is reversible, thereby allowing for signal reconstruction, possibly after removal of specific components.

CEEMD performs exceptionally well overcoming mode-mixing problems. The reconstruction error is around machine precision (Torres et al., 2011b). The computation of the instantaneous frequency from the isolated modes leads to a well defined time-frequency representation. SST shares many of the advantages of CEEMD in practice, with an acceptable reconstruction error. Thus, both methods are suitable to decompose a seismic trace into individual components with the advantage of frequency localization. It may also aid in noise-attenuation problems in which the signal and noise correspond to different components, likewise, a recently pro- posed technique based on regularized nonstationary autoregression (Fomel, 2013). As in this chapter, Fomel (2013) also suggests seismic data compression and seismic data regularization as possible applications for seismic data decomposition into spectral components. Both approaches aim to decompose seismic data into a sum of oscillatory signals with smoothly varying frequencies and smoothly varying amplitudes (Fomel, 2013; Thakur et al., 2013), which is the principle of the decomposition using the CWT (Daubechies et al., 2011).

CEEMD using 50 noise realizations is approximately 13 times slower than SST using our parameter settings; SST has approximately the same cost as a wavelet transform; yet neither method is prohibitively expensive. We found that using a classical Morlet wavelet and 32 levels for the SST method we get a good balance between speed and resolution in the frequency representation. The improvement of SST is clear compared with the CWT. The reassignment technique plays a important role in the results, by reallocating the wavelet energy to the corresponding time position.

CEEMD and SST are more appropriate than STFT and CWT when better time-frequency localization is needed. On the other hand, STFT and CWT remain very useful analysis methods, even if they may be subject to more spectral leakage than the CEEMD and SST methods, because they do not collapse spectra to narrow frequency bands. For instance, many attenuation methods are based on spectral ratios between two signals (Reine et al., 2009, 2012). Spectral ratios are difficult to compute if only individual frequency lines exist. On the other hand, it may be possible to use the frequency shift method (Quan and Harris, 1997) to estimate seismic attenuation using the CEEMD and SST methods. SST, due the reassignment step, will concentrate the energy a small spectral band. Thus, it will be more appropriate when better time-frequency localization is needed (such as stratigraphic mapping to detect channel structures, identification of resonance frequencies).

From our study we find that SST and CEEMD perform equally well for the seismic time-frequency representation, with the advantage of speed and a stronger mathematical foundation for the SST. A further difference is that in the SST method, one can specify the frequency range of interest prior to decomposition via the CWT scale parametrization. This can speed up computations in many situations, whereas in CEEMD components are always estimated sequentially starting with the highest-frequency ones.

3.4 Conclusions

The SST has a strong mathematical foundation based on frequency reassignment of wavelet transform decompositions. In simple applications SST and CEEMD give comparable results, although in more complex situations, SST can yield more favorable results since it has the ability to adapt the mother wavelet to the data under consideration. On the other hand, the advantage of CEEMD and variants is precisely the fact that no decomposition basis needs to be specified, eliminating the possible requirement to test for performance enhancements by changing the decomposition basis.

SST produces an acceptable reconstruction error, which improves as we extend the level of decomposition. This frequency-based decomposition method can reconstruct individual components from selected frequency bands. SST is therefore attractive for high-resolution time-frequency analysis of seismic signals.

Chapter 4

Seismic Denoising via Ensemble Empirical Mode Decomposition[1]

Summary

Random and coherent noise exist in microseismic and seismic data, and suppressing noise is a crucial step in seismic processing. In this chapter, we propose a novel seismic denoising method, based on a data-driven technique, ensemble empirical mode decomposition (EEMD). This technique is first proposed as a trace-based method and valid for random noise suppression. We compare it with bandpass filter and basis pursuit methods. Furthermore, we extend the proposed method into frequency-offset (f-x) domain, as f-x EEMD thresholding, to enhance the lateral coherence of the seismic data, we compare it with classic f-x deconvolution and f-x EMD. The synthetic and field data examples illustrate the better performance of our proposed technique. It is not only a potential technique for microseismic denoising, but also effective for suppressing random and coherence noise in seismic data.

---

[1] A version of this chapter has been submitted. Jiajun Han and Mirko van der Baan, Geophysics, 2014, under review.

4.1 Introduction

The denoising via EMD started from examining the properties of IMFs resulting from white Gaussian noise (Flandrin et al., 2004a). The first attempt is detrending and denoising ECG signals by partial reconstructions with the selected IMFs (Flandrin et al., 2004). However, this approach has the disadvantage that even if the appropriate IMFs are selected, they still may be noise contaminated. Boudraa and Cexus (2006) improve the denoising scheme by using adaptive thresholding and a Savitzky-Golay filter for each IMF, respectively. Inspired by translation invariant wavelet thresholding, Kopsinis and McLaughlin (2009) propose an iterative EMD denoising method to enhance the original method. Recently, hybrid EMD denoising methods, based on higher order statistics and curvelet transform have also been proposed (Tsolis and Xenos, 2011; Dong et al., 2013).

In seismic processing, the f-x domain plays a significant role because linear or quasilinear events in the time-offset (t-x) domain manifest themselves as a superposition of harmonics in the f-x domain. Canales (1984) first proposed prediction error filtering, based on an autoregressive (AR) model in the f-x domain to attenuate random noise, which is widely known as f-x deconvolution. However, the AR model assumes that the error is an innovation sequence rather than additive noise. Soubaras (1994) introduced the f-x projection filtering to circumvent this problem by utilizing the autoregressive-moving average (ARMA) model instead of the AR model. Sacchi and Kuehl (2001) further discuss the ARMA formulation in the f-x domain, and discover the ARMA coefficients can be computed by solving an eigenvalue problem. Integration of EMD into the f-x domain is first investigated by Bekara and Van der Baan (2009). They find that eliminating the first IMF component in each frequency slice corresponds to an auto-adaptive wavenumber filter. This process reduces the random and steeply dipping coherent noise in the seismic data. Instead of directly deleting the first IMF in the f-x domain, Chen and Ma (2014) apply the AR model on the first IMF to enhance the original f-x EMD performance.

In this chapter, we first propose a novel method for suppressing random noise based on ensemble empirical mode decomposition (EEMD) principle. Next, we test the proposed EEMD thresholding on both low and high signal to noise ratio (SNR) synthetic and microseismic examples. Finally, we extend the proposed method into the f-x domain to suppress random and coherence noise in seismic data.

4.2 Theory

4.2.1 EEMD thresholding

The first attempt at using EMD as a denoising tool emerged from the need to know whether a specific IMF contains useful information or primarily noise. Thus, Flandrin et al. (2004a) and Wu and Huang (2004) nearly simultaneously investigate the EMD feature for Gaussian noise, and they conclude that EMD acts essentially as a dyadic filter bank resembling those involved in wavelet decomposition. Therefore, the energy of each IMF from white Gaussian noise follows an exponential relationship, and Kopsinis and McLaughlin (2009) refine this relationship as

$$E_k^2 = (E_1^2/0.719) \times 2.01^{-k}, \tag{4.1}$$

where E_k^2 is the energy of the $k-th$ IMF, and the parameters 0.719 and 2.01 are empirically calculated from numerical tests. As the IMFs resemble the wavelet decomposition component, the energy of the first IMF E_1^2 can be estimated using a robust estimator based on the component's median (Donoho and Johnstone, 1994):

$$E_1^2 = (median(|IMF1(i)|)/0.6755)^2, \quad i = 1,2...n. \tag{4.2}$$

where n is the length of the input signal. Then we can set the adaptive threshold T_k in each IMF for suppressing the random noise as

$$T_k = \sigma \times \sqrt{(2 \times ln(n))} \times E_k, \tag{4.3}$$

where σ is the main parameter to be set. Combination of Equations 4.2 and 4.3 is a universal threshold for removing the white Gaussian noise in the wavelet domain (Donoho and Johnstone, 1994; Donoho, 1995).

Followed by the above procedures, the reconstructed signal $\hat{s}$ is expressed as

$$\hat{s} = \sum_{k=m1}^{M-m2} T_k[IMF_k] + \sum_{k=m2+1}^{M} IMF_k. \tag{4.4}$$

thresholding is only applied between the $m1-th$ and $(M-m2)-th$ IMFs, where IMF_k is the $k-th$ IMF, and M is the total number of IMFs of the input signal. If $m2$ is set to 0, we apply the thresholding from the $m1-th$ IMF to the last IMF. The implemented threshold method is IMF interval thresholding (Kopsinis and McLaughlin, 2009), which is presented in the next section.

Due to the mode mixing of EMD, direct application of the above procedure may not achieve the best effect. Kopsinis and McLaughlin (2009) try to alter the input signal by circle-shifting its IMF1 component, and adding the circle-shifted IMF1 back to create a different noisy version of the signal. This works IMF1 only contains noise when the input signal's SNR is low, and the circle-shifting does not change the embedded useful signal information. Averaging of the denoised outputs of different triggered signals can enhance the final result. However, when the input signal's SNR is high, directly altering IMF1 of the input signal would adversely affect results.

Considering the different SNR cases, we employ the EEMD principle to improve the EMD denoising performance. The procedure of EEMD denoising is as below:

(1). Create white Gaussian noise.

(2). Calculate IMF1 of the white Gaussian noise and add it onto the target/input signal using a predefined SNR.

(3). Decompose the resulting signal into IMFs.

(4). Apply the EMD denoising principle to the resulting IMFs.

(5). Repeat steps (1), (2), (3) and (4) several times with different noise realizations.

(6). Compute the ensemble denoising average as the final output.

Although not adding the whole white Gaussian noise sequence onto the target signal does not exactly respect the EEMD principle, it shows better results in our synthetic and real data examples rather than a denoising procedure exactly based on EEMD. Due to the dyadic filter feature of EMD, IMF1 of white Gaussian noise corresponds to the high frequency noise. It helps relieve the mode mixing of EMD to some extent, and only affects the high frequency information of the input signal, which can be compensated by a bandpass filter after the proposed EEMD denoising.

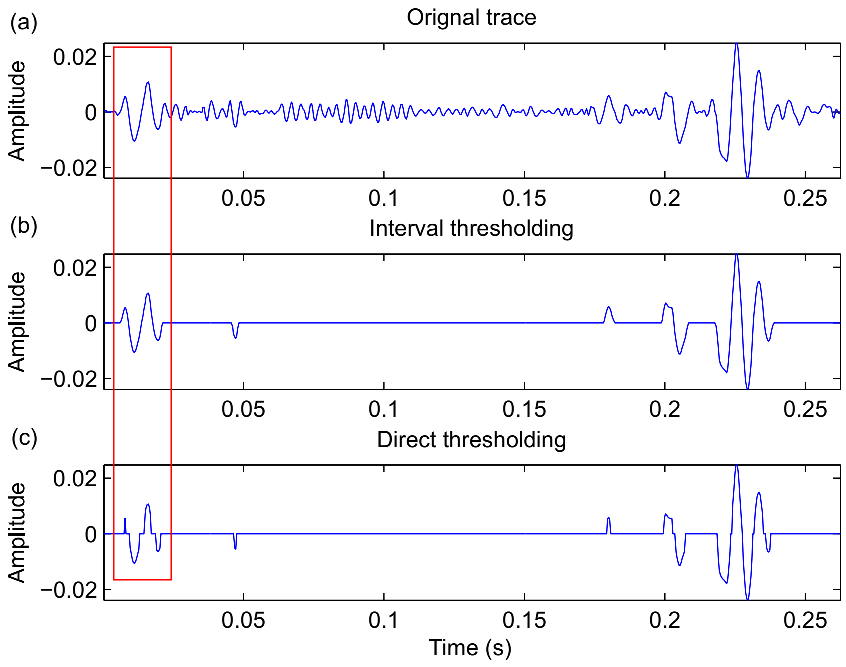

Figure 4.1: The difference between IMF interval thresholding and direct thresholding. (a). An IMF from a microseismic event. (b). IMF interval thresholding result. (c). Direct thresholding result.

4.2.2 IMF interval thresholding

In the EMD theory, each IMF is a fundamental element of the input signal. The local extrema and zero crossings are the basic elements for each IMF due to its symmetric feature. Kopsinis and McLaughlin (2008a) proposed IMF interval thresholding which preserves the smooth feature of each IMF. The idea of IMF interval thresholding is maintaining the whole interval between two zero crossings in each IMF, if the absolute value of local extrema in this interval is larger than the threshold. Take hard thresholding as an example, the expression of direct hard thresholding is

$$\hat{h}(t) = \begin{cases} h(t), |h(t)| > T \\ 0, |h(t)| \leq T, \end{cases} \tag{4.5}$$

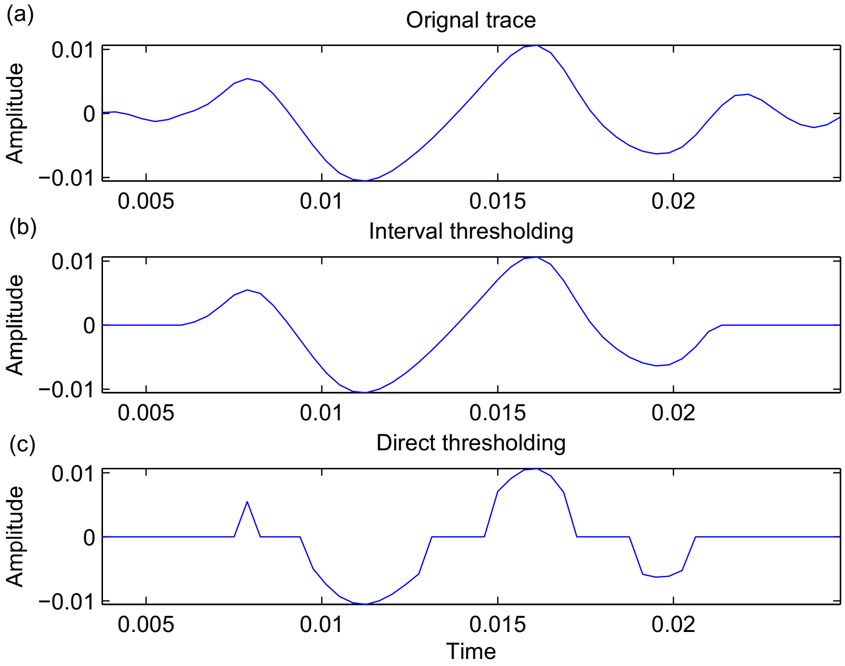

Figure 4.2: Enlarged part of red box in Figure 4.1. (a). An IMF from a microseismic event. (b). IMF interval thresholding result. (c). Direct thresholding result. The IMF interval thresholding keeps the smooth features of the IMF, whereas the direct thresholding creates needless discontinuities.

where $h(t)$ is the input signal, T is the universal threshold, and $\hat{h}(t)$ is the thresholded signal. The interval hard thresholding is expressed as

$$\hat{h}(\mathbf{z}_j) = \begin{cases} h(\mathbf{z}_j), |h(r_j)| > T \\ 0, |h(r_j)| \leq T, \end{cases} \tag{4.6}$$

$h(\mathbf{z}_j)$ indicates the sample interval between adjacent zeros crossings of the input signal, and $h(r_j)$ is the local extrema corresponding to this interval. $\hat{h}(\mathbf{z}_j)$ is the thresholded output. Due to the conditions of each IMF, it guarantees that there is one and only one local extrema $h(r_j)$ in the interval of $h(\mathbf{z}_j)$.

Figure 4.1 illustrates the difference between interval and direct hard thresholding. Figure 4.1(a) is an IMF from a microseismic event. The enlarged part of red box is shown in Figure 4.2. Direct thresholding (Figures 4.1(c) and 4.2(c)) creates needless discontinuities, therefore can have adverse consequences for the continuity of the reconstructed signal. Luckily, these discontinuities can be effectively reduced by IMF interval thresholding (Figures 4.1(b) and 4.2(b)). The new thresholding method retains the smooth features of each IMF.

The above example is for hard interval thresholding; soft interval thresholding is also based on the same idea. For more detail information about soft interval thresholding, please refer to the paper of Kopsinis and McLaughlin (2008b).

4.2.3 F-x domain EEMD thresholding

For seismic data, one option is applying the proposed EEMD thresholding to each trace for suppressing the random noise. The disadvantage of this approach is not considering the lateral coherence of the seismic reflections. A sophisticated approach is applying the EEMD thresholding in the f-x domain. To process a whole seismic section, f-x EEMD thresholding is implemented in a similar way to f-x EMD (Bekara and Van der Baan, 2009) and f-x deconvolution using the following scheme:

(1). Select a time window and transform the data to the f-x domain.

(2). For every frequency, separate real and imaginary parts in the offset sequence.

(3). Apply EEMD thresholding on real and imaginary parts, respectively.

(4). Combine to create the filtered complex signal.

(5). Transform data back to the t-x domain.

(6). Repeat for the next time window.

Bekara and Van der Baan (2009) first propose the f-x EMD filter, and they find the IMF1 contains the largest wave-number components in a constant frequency slice in the f-x domain. Therefore, signal-to-noise enhancement can be achieved by subtracting IMF1 from the data. In the f-x EEMD thresholding implementation, the parameters $m1$ and $m2$ control the threshold range of the IMF order, and parameter σ is related to the noise level. The f-x EMD filter is a special case of the f-x EEMD thresholding with parameters as $\sigma = 0$, $m1 = 2$ and $m2 = 0$. Unlike the f-x deconvolution, which uses a fixed filter length for all frequencies, EMD adaptively matches its decomposition to the smoothness of the data. Directly eliminating IMF1 of a signal means removing its most oscillatory element, and the residual receives a smoother feature. However, only subtracting IMF1 in each constant frequency slice seems to be not enough or too harsh for some seismic data (Chen and Ma, 2014); f-x EEMD thresholding thus improves its performance.

4.3 Example

4.3.1 Synthetic example

Figure 4.3(a) shows synthetic data also used in Han et al. (2013), which is comprised of several events with 30 and 40Hz Ricker wavelets. Figure 4.3(b) contains the noise contaminated version with SNR equal 1 in each trace. This is a low SNR case to test our proposed method. As the proposed method is a single trace technique, we first compare with an appropriately set bandpass filter (Figure 4.3(c)). As the random noise pollutes the whole frequency domain, a bandpass filter is not an effective method here. Our proposed method with $\sigma = 0.35$, $m1 = 3$ and $m2 = 0$ (Figure 4.3(e)) suppresses most of the random noise and better enhances the events, hence dramatically improves the SNR of the test data. Note that the same bandpass filter as Figure 4.3(c) is applied after the proposed denoising method. Another technique we compare here is the basis pursuit approach (Chen et al., 2001), which has been shown as an effective tool for suppressing random noise in seismic and microseismic processing (Han et al., 2013; Vera Rodriguez et al., 2012). Basis pursuit with regularization parameter 0.1 (Figure 4.3(g)) eliminates most of the random noise, but results in a slight signal loss in the difference section (Figure 4.3(h)). Bandpass filter and EEMD denoising methods do not lead to any information loss (Figures 4.3 (d) and (f)).

Next, we select the trace at offset 245m as an example to analyze elaborately the impacts of different denoising methods. Shown from (a) to (e) in Figure 4.4 are respectively noise free data (Figure 4.3(a)), noisy version (Figure 4.3(b)), bandpass filter (Figure 4.3(c)), our proposed method (Figure 4.3(e)) and basis pursuit approach (Figure 4.3(g)). As the SNR of each trace equals 1, the random noise affects the waveforms severely. Compared with bandpass filter, the EEMD denoising and basis pursuit techniques effectively eliminate the random noise, and protect the useful waveform to the maximum extent. Figures 4.5 to 4.7 illustrate the principle of the EEMD thresholding. The solid line (Figure 4.5) is the theoretical IMF energy of white Gaussian noise based on equation (4.1), and the dashed line represents the IMF energy of the noisy trace (Figure 4.4 (c)). The slope of first two IMFs energy matches the theoretical line most, which indicates they are similar to the noise characteristic most. On the other hand, the other IMFs contain less noise since their energy distribution deviates from the theoretical line. Figure 4.6 shows the 9 IMFs of the test trace using EEMD. The first two IMFs contain the highest frequency information, and least signal information can be found. This agrees with Figure 4.4. The parameters $m1 = 3$ and $m2 = 0$ indicate that the thresholding is only applied from IMF3 to the last IMF, and sets the reconstructed IMF1 and IMF2 to zero. Figure 4.7 shows the 9 thresholded IMFs. IMF interval thresholding makes the reconstructed IMFs keep the smooth features, meanwhile get rid most of the noise. Note that we apply soft thresholding in this synthetic example.

A high SNR case of Figure 4.3(a) is shown in Figure 4.8. In this test, the SNR for each trace is 2.5 (Figure 4.8(b)). The results from bandpass filter, EEMD thresholding with $\sigma = 0.3$, $m1 = 2$ and $m2 = 0$, and basis pursuit with regularization parameter 0.05 are shown in the same sequence as Figure 4.3. All three methods improve the input noisy data (Figure 4.8(b)). Like the low SNR case, the EEMD thresholding (Figure 4.8(e)) and basis pursuit (Figure 4.8(g)) approaches show clearer outputs than the bandpass filter ((Figure 4.8(c))), as they reduce random noise from the whole frequency band. From the difference sections, there is no obvious information lost for the proposed EEMD thresholding (Figure 4.8(f)) and bandpass filter (Figure 4.8 (d)). The traces at offset 245m from noise free data, noisy data, bandpass filter, EEMD thresholding and basis pursuit outputs, are shown in Figure 4.9 (a) to (e). Compared with another two methods, EEMD thresholding (Figure 4.9(d)) shows the most proximal result to the noise free one (Figure 4.9(a)).

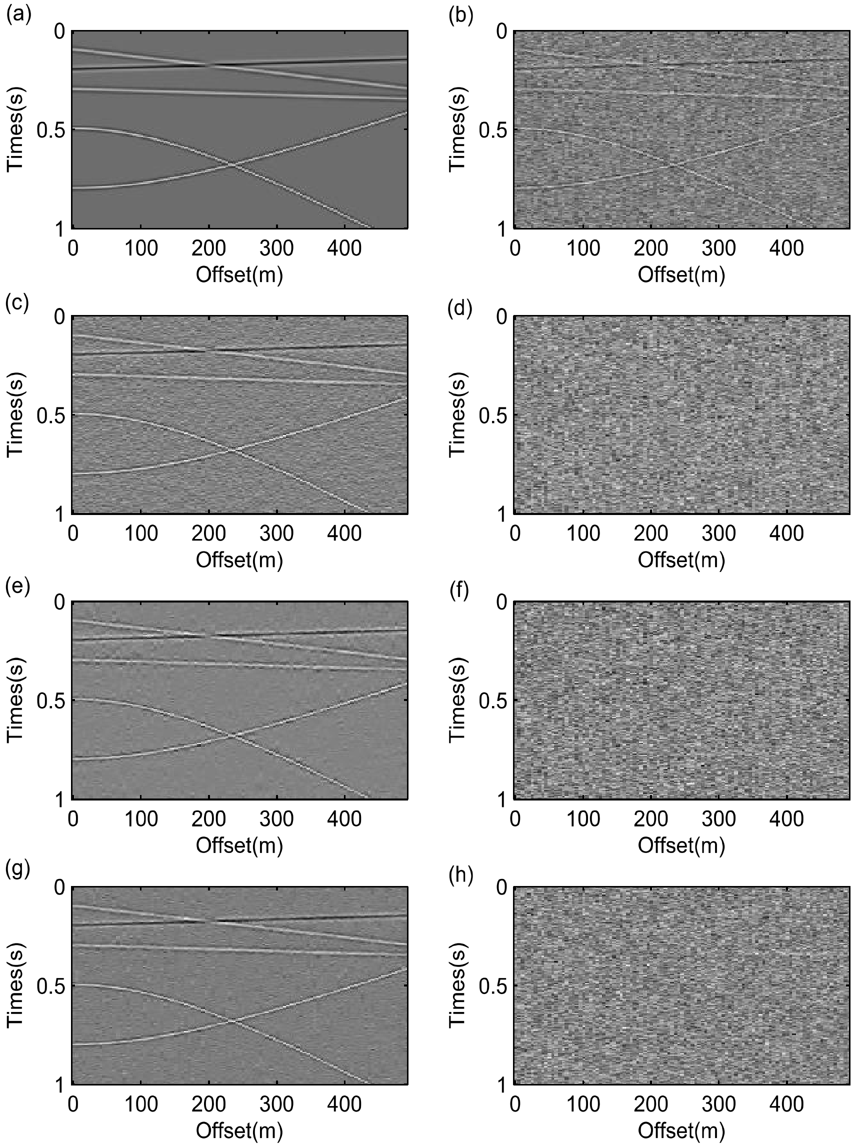

Figure 4.3: EEMD thresholding on low SNR case. (a). Noise free data from Han et al. (2013). (b). Noisy version with SRN = 1. (c). Bandpass filter output. (d). Difference of bandpass filter. (e). Proposed EEMD denoising output. (f). Difference of the proposed method. (g). Basis pursuit output. (h). Difference of basis pursuit. Compared with bandpass filter, the proposed and basis pursuit methods eliminate more random noise, therefore dramatically improve the quality of the original data.

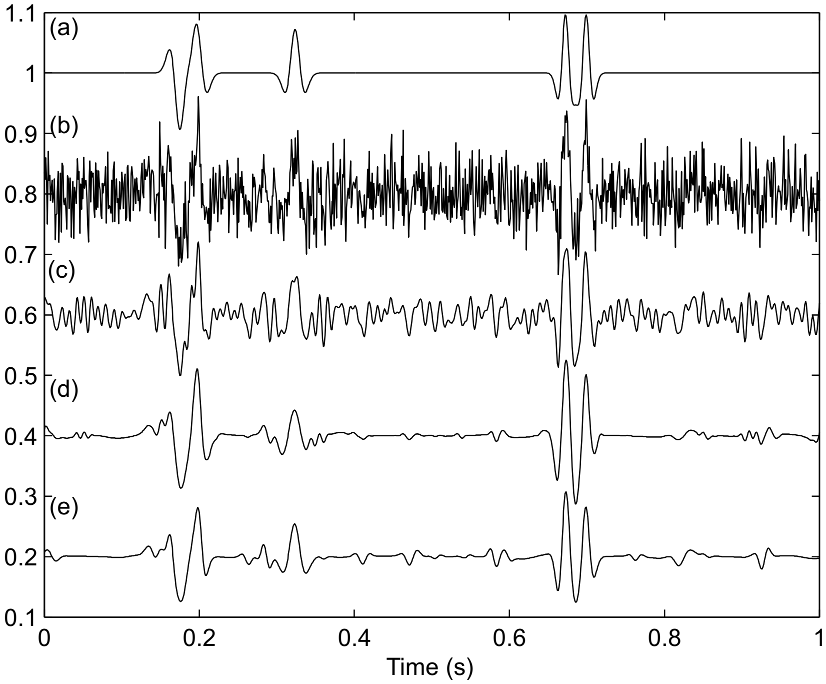

Figure 4.4: Trace at offset 245m. (a). Noise free trace. (b). Noisy trace with SNR = 1. (c). Trace after bandpass filter. (d). Trace after EEMD thresholding. (d). Trace after basis pursuit. EEMD thresholding and basis pursuit suppress more random noise than bandpass filter.

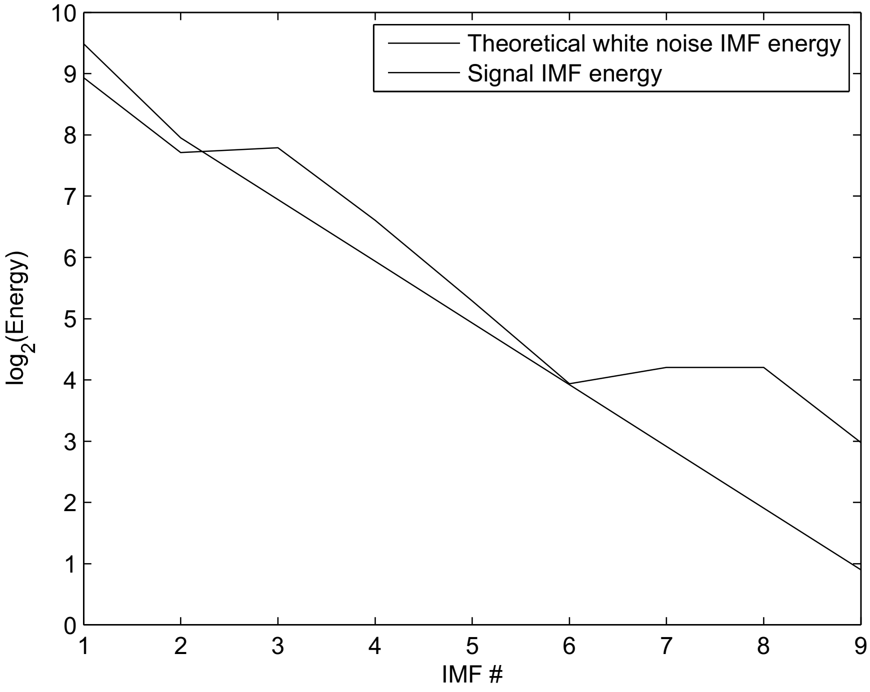

Figure 4.5: The IMF energy distribution of the noisy trace at offset 245m and the theoretical IMF energy distribution of white Gaussian noise based on equation 4.1.

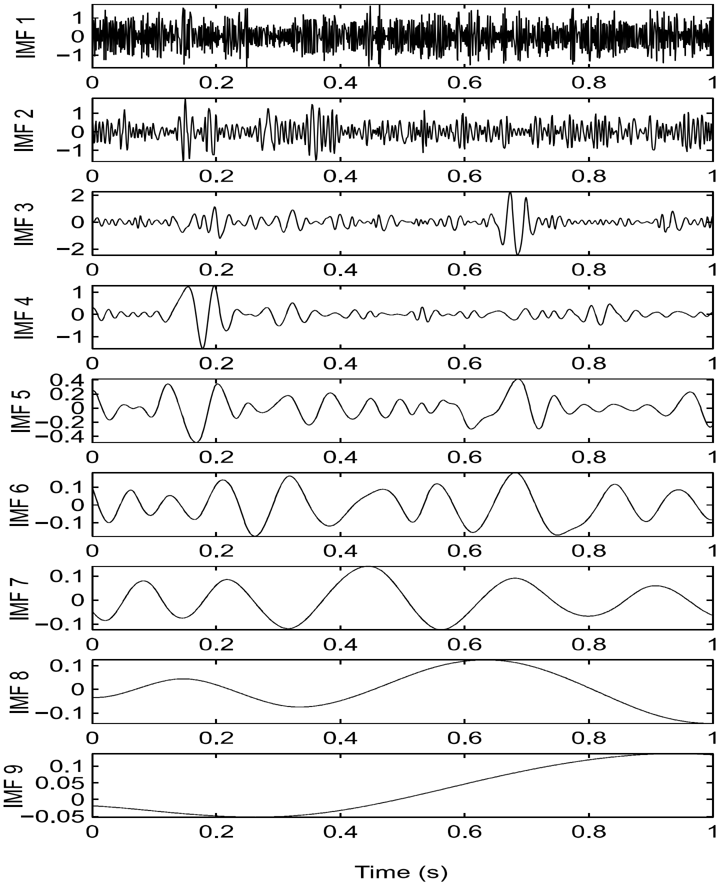

Figure 4.6: IMFs of noisy trace at offset 245m. IMF1 and IMF2 contain the highest frequency information, which are out of frequency band of interesting.

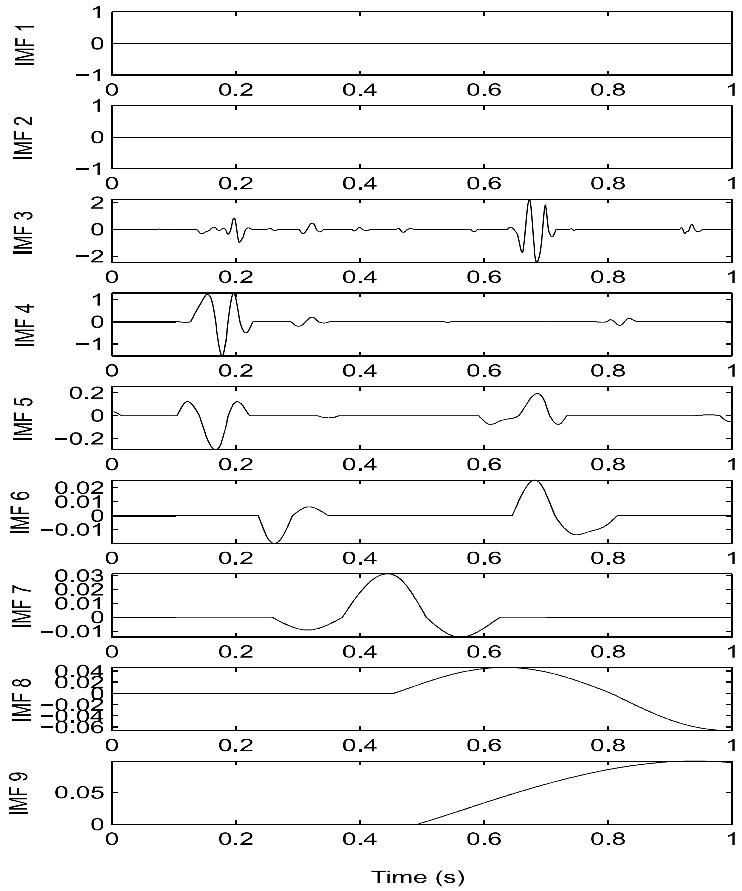

Figure 4.7: Thresholded IMFs. The reconstructed IMF1 and IMF2 are set as 0. IMF interval thresholding is applied from IMF3 to the last IMF.

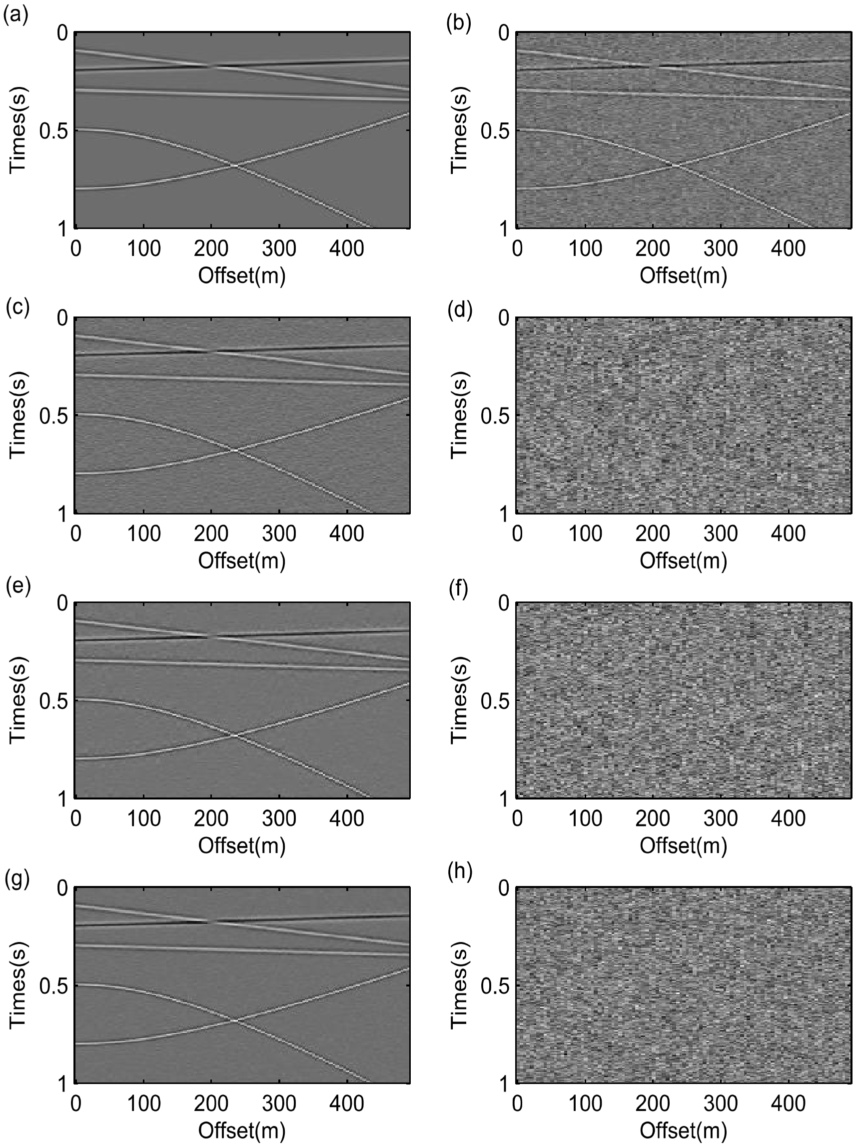

Figure 4.8: EEMD thresholding on high SNR case. (a). Noise free data. (b). Noisy version with SRN = 2.5. (c). Bandpass filter output. (d). Difference of bandpass filter. (e). Proposed EEMD denoising output. (f). Difference of the proposed method. (g). Basis pursuit output. (h). Difference of basis pursuit. Our proposed and basis pursuit methods suppress more random noise than bandpass filter. There is no information loss in the difference sections of bandpass filter and proposed method.

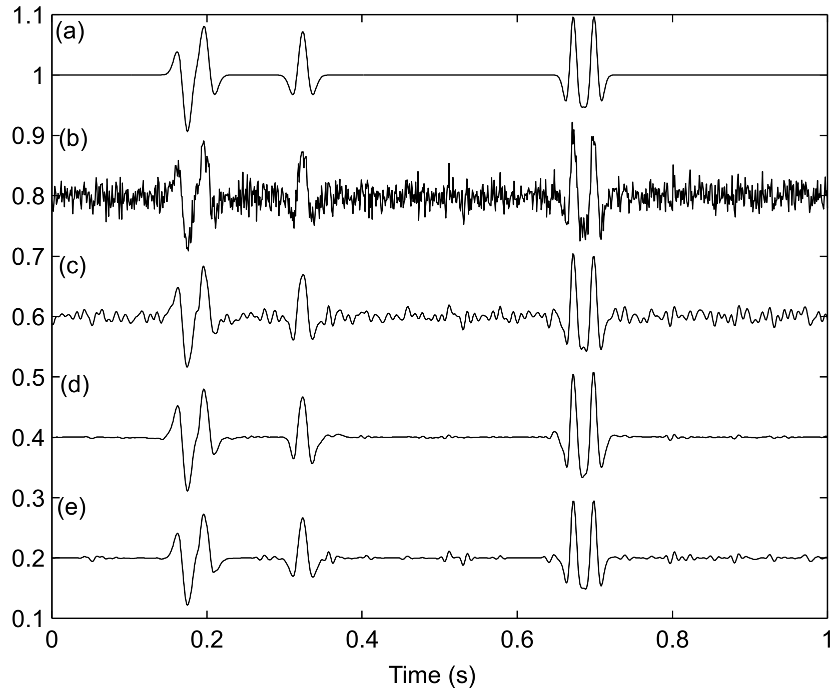

Figure 4.9: Trace at offset 245m. (a). Noise free trace. (b). Noisy trace with SNR = 2.5. (c). Trace after bandpass filter. (d). Trace after EEMD thresholding. (d). Trace after basis pursuit. EEMD thresholding obtains the smoothest output.

4.3.2 Microseismic example

In this section, we show two microseismic cases to verify the proposed technique. Figure 4.10 (a) is one of 66 microseismic events from a hydraulic fracturing treatment in Canada. Unlike the synthetic examples, the quality of these microseismic events is much better. The traditional denoising method for microseismic data is bandpass filtering. However, due to the diversity of microseismic data, a fixed frequency range may remove some useful signal. Figure 4.10(b) shows the result of a fixed bandpass filter. Note that this bandpass filter works well for most of the microseismic events in these data, but it removes some of the low frequency components around 0.56s. Furthermore, there is still some noise before the P-wave arrives.

The proposed EEMD thresholding with $\sigma = 0.6$, $m1 = 2$ and $m2 = 1$, and basis pursuit with regularization parameter 0.005 outputs are shown in Figures 4.9(c) and 4.9(d). Like bandpass filter, they both suppress most of the random noise. Furthermore, these two techniques preserve well the waveform information as they can distinguish the noise and useful information in their own domain. The denoising performance is also confirmed in their spectra (Figure 4.11). All three methods remove all the higher frequency noise. The proposed method (Figure 4.11(c)) and basis pursuit (Figure 4.11(d)) preserve the low frequency information better than the bandpass filter (Figure 4.11(b)). Only EEMD thresholding keeps the components around 300Hz, which probably contains some signal information.

A challenging microseismic test (Castellanos and van der Baan, 2013) is shown in Figure 4.12, which comes from Saskatchewan in Canada. The raw data (Figure 4.12(a)) quality is bad, as it does not only contain random noise, but also strong electronic noise. High energy 30 Hz, 60Hz and 120 Hz noise components exist in its spectrum (Figure 4.13(a)). Directly applying the EEMD thresholding and basis pursuit to the raw data would fail, as they are only valid for suppressing random noise. A pre-processing step must be accomplished before the further processing. Figure 4.12(b) is the output after a bandpass filter and notch process of 30 Hz and 60 Hz. The 120 Hz energy is not notched down as it is not visible in the other microseismic events of this experiment.

Even though the pre-processing improves the quality of the raw data, Figure

4.12(b) still suffers from severe random noise. EEMD thresholding (Figure 4.12(c)) with $\sigma = 0.25$, $m1 = 1$ and $m2 = 1$ reduces more random noise than the basis pursuit (Figure 4.12(d)), and it more effectively (Figure 4.12(c)) drops down the 120 Hz energy than basis pursuit (Figure 4.12(d)). Note that the regularization parameter is 35 for basis pursuit implementation. On the other hand, both techniques dramatically improve the SNR of the microseismic event, and this is also confirmed in the enlarged part from 0.2s to 0.8s (Figure 4.14). The denoising (Figures 4.14(c) and (d)) makes the first arrival pick much easier than on the original microseismic event or after pre-processing. The arrows indicate the first arrival pick at 0.498s, which is difficult to detect in Figure 4.14 (a) and (b). Denoising of microseismic events can facilitate picking of the first arrival times and their polarities, which is a crucial step in microseismic processing.

4.3.3 Seismic example

In this section, we verify the performance of f-x EEMD thresholding. Figure 4.15 is a stacked section from Alaska (Geological-Survey, 1981). Although the events become continuous after stacking, random, coherent and background scattered noise still exist, thereby reducing the SNR of the seismic data. Implement EEMD thresholding in the f-x domain, mainly because linear or quasilinear events in the t-x domain manifest as a superposition of harmonics in the f-x domain. Therefore, we compare the result with the classic f-x deconvolution and f-x EMD (Bekara and Van der Baan, 2009).

All three methods are implemented between 0 Hz to 60% of the Nyquist frequency, and frequency beyond 60% of the Nyquist frequency are damped to zero. F-x EMD only eliminates the IMF1 component in each frequency slice, which makes it a parameter free technique; f-x deconvolution uses the length of AR operator as 20, pre-whitening as 0.1; f-x EEMD denoising employs $\sigma = 0.3$, $m1 = 3$ and $m2 = 0$. The outputs of three methods are shown in Figure 4.16. All the techniques enhance the quality of the input data by making the events clearer, especially in the deep part. From the difference sections (Figure 4.17), neither method loss the reflection information. F-x deconvolution (Figure 4.17(b)) and f-x EEMD denoising (Figure

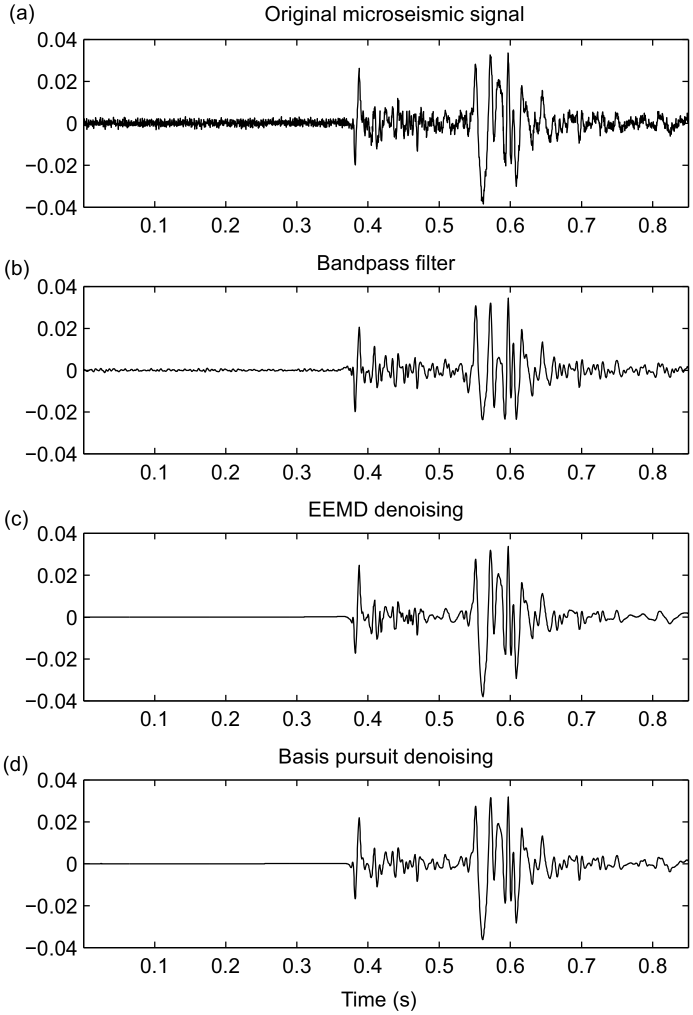

Figure 4.10: High SNR microseismic event example. (a). Raw microseismic event. (b). Bandpass filter output. (c). EEMD thresholding output. (d). Basis pursuit output. Bandpass filter removes some of the low frequency components around 0.56s. The proposed method and basis pursuit preserve the waveform better.

4.17(c)) seem to eliminate more random noise than f-x EMD (Figure 4.17(a)). The advantage of our proposed method and f-x EMD over f-x deconvolution is that, except the random noise, they can eliminate the linear dipping energy as well. Note that all figures are shown on the same amplitude scale.

Figure 4.18 is the enlarged part of the original data from time 2s - 3.6s and CMP number 1000 - 3500. It clearly shows that the Alaska data does not only contain

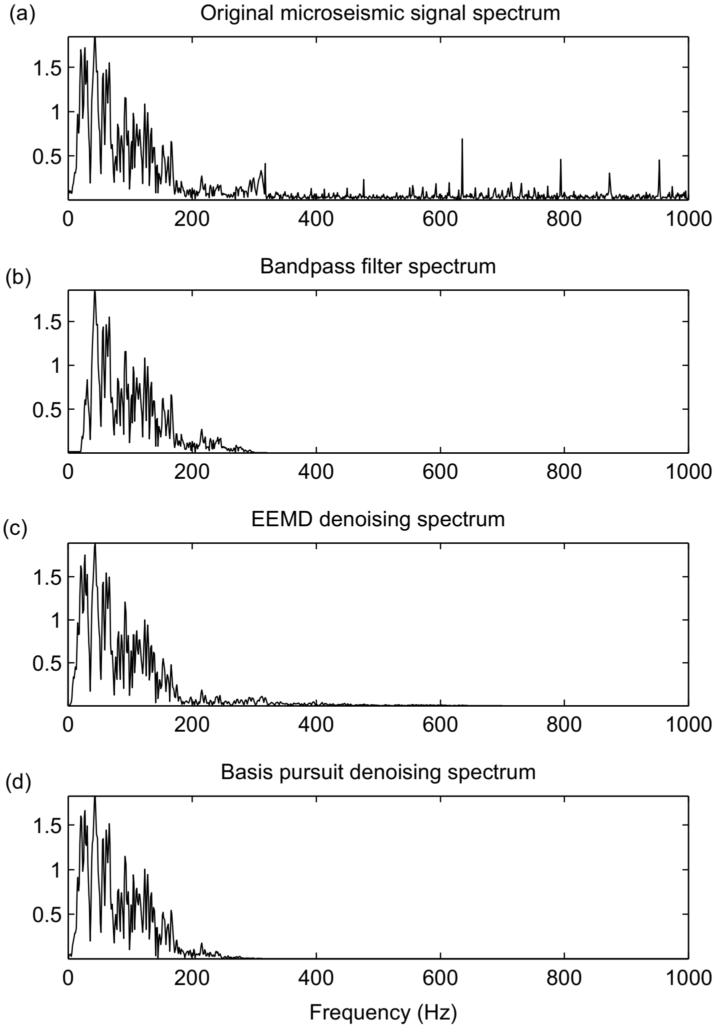

Figure 4.11: The spectrum of Figure 4.10. (a). Spectrum of the original microseismic event. (b). Spectrum after bandpass filter. (c). Spectrum after the proposed method. (d). Spectrum after basis pursuit. Due to the diversity of microseismic data, a fixed frequency range may remove some useful signal. EEMD thresholding and basis pursuit preserve the low frequency information better than the bandpass filter. Furthermore, EEMD thresholding maintains the components around 300 Hz.

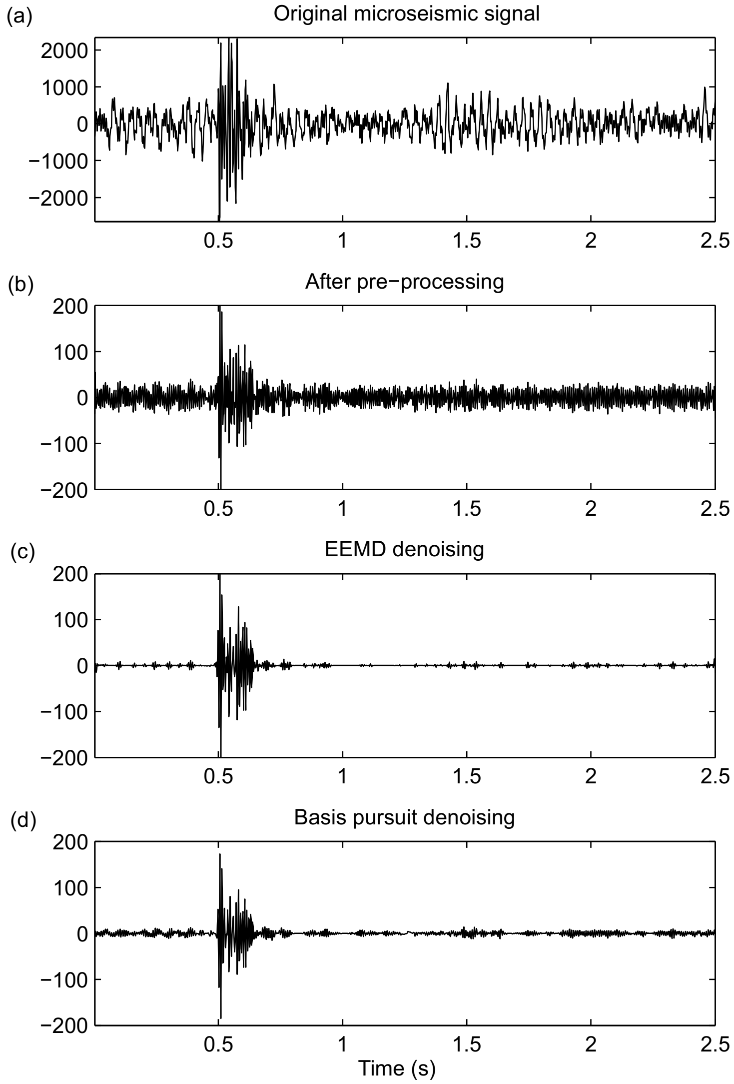

Figure 4.12: Low SNR microseismic event example. (a). Raw microseismic event. (b). Output after pre-processing. (c). EEMD thresholding output on (b). (d). Basis pursuit output on (b). The raw microseismic event contains the random noise and electronic noise. The output after pre-processing gets rid of most of the electronic noise. EEMD thresholding and basis pursuit suppress most of the random noise.

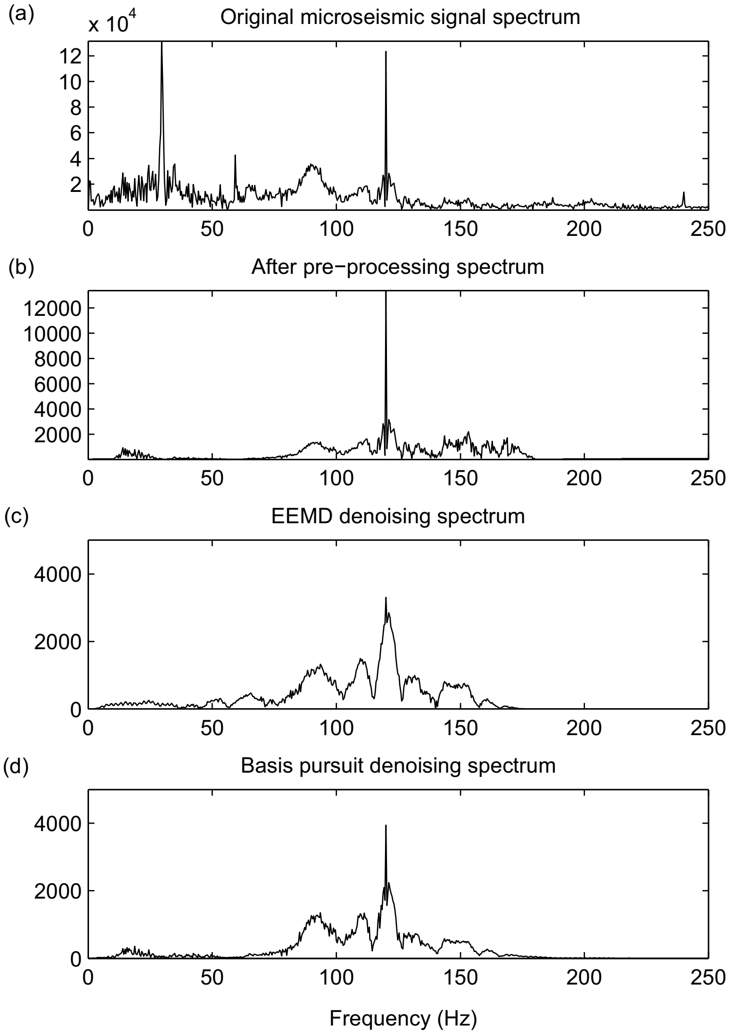

Figure 4.13: The spectrum of Figure 4.12. (a). Spectrum of the raw microseismic event. (b). Spectrum after pre-processing. (c). Spectrum after the proposed method on (b). (d). Spectrum after basis pursuit on (b). There are 30 Hz, 60 Hz and 120 Hz electronic noise in raw microseismic event. The pre-processing reduces the electronic noise at 30 Hz and 60 Hz. EEMD thresholding and basis pursuit eliminate most of the random noise. The proposed method drops down the 120 Hz energy more effectively than the basis pursuit approach.

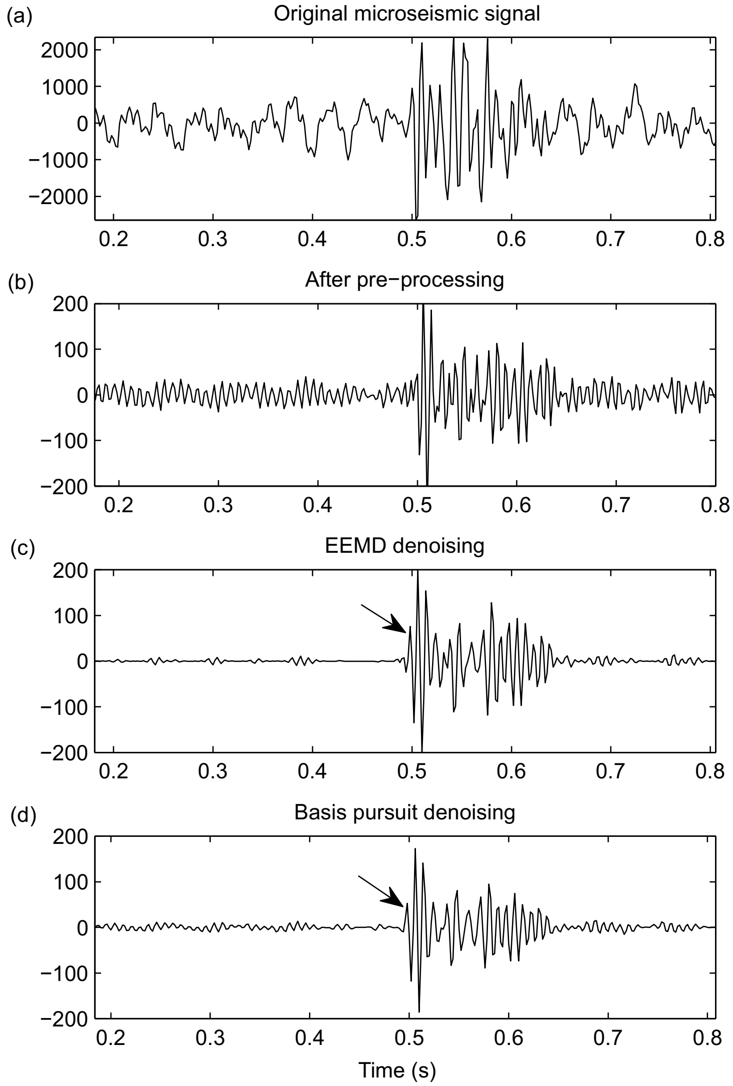

Figure 4.14: Enlarged part of Figure 4.12. (a). Original raw microseismic event. (b). Output after pre-processing. (c). EEMD thresholding output on (b). (d). Basis pursuit output on (b). The arrows in (c) and (d) mark the first arrival time, which are hard to pick on the raw microseismic event (a) or after pre-processing (b).

random but also coherent noise, like high energy linear dipping events. The same enlarged parts of three denoising outputs are shown in Figure 4.19. F-x EEMD thresholding (Figure 4.19(c)) obtains the most satisfactory output, and the events become much clearer. There are still some random and coherent noise in the results of f-x EMD (Figure 4.19(a)) and f-x deconvolution (Figure 4.19(b)) in varying degrees. F-x EMD, which eliminates only IMF1 component in each frequency, does not seem to have great impact in the data. The proposed method with parameters $m1 = 3$, $m2 = 0$ and $\sigma = 0.3$ means deleting the first two IMFs, and also applying the IMF interval thresholding from IMF3 to the last IMF. This explains why the difference section of the f-x EMD (Figure 4.20(a)) contains only a portion of noise compared with the one of the proposed method (Figure 4.20(c)). On the other side, since f-x deconvolution is only valid for random noise suppression, no dipping noise is shown in its difference profile (Figure 4.20(b)).

4.4 Discussion

EMD is a fully data-driven technique, and no a priori decomposition basis is chosen such as sines and cosines for the Fourier transform or a mother wavelet for the Wavelet transform. The EMD denoising foundation, equation 4.1, is an average result on Monte Carlo simulation of EMD on white Gaussian noise. Kopsinis and McLaughlin (2009) discuss it and further improve the EMD denoising scheme. The proposed method utilizes the EEMD principle, aim to stabilize the EMD denoising performance; first, the added noise solves the mode mixing to some extent,and second, equation 4.1 is an average result of 5000 times simulation (Flandrin et al., 2004a), therefore more time decomposition of EMD makes the IMFs energy distribution closer to the theoretical distribution.

As a comparison, basis pursuit obtains similar satisfactory results in the synthetic and microseismic examples. However it is strongly dependent on the pre-defined wavelet dictionary. We employ the Ricker wavelets as the pre-defined dictionary in both examples (Vera Rodriguez et al., 2012; Bonar and Sacchi, 2013). The excellent manifestation in the synthetic example is because the pre-defined dictionary matches

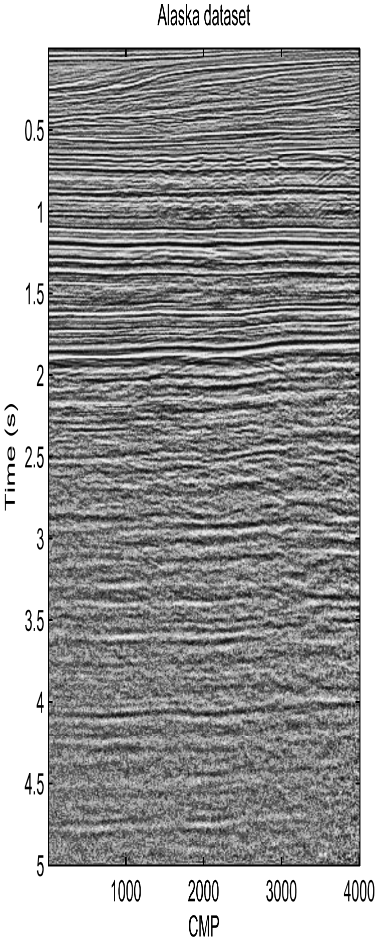

Figure 4.15: Alaska data. There are random and coherent noise in the data.

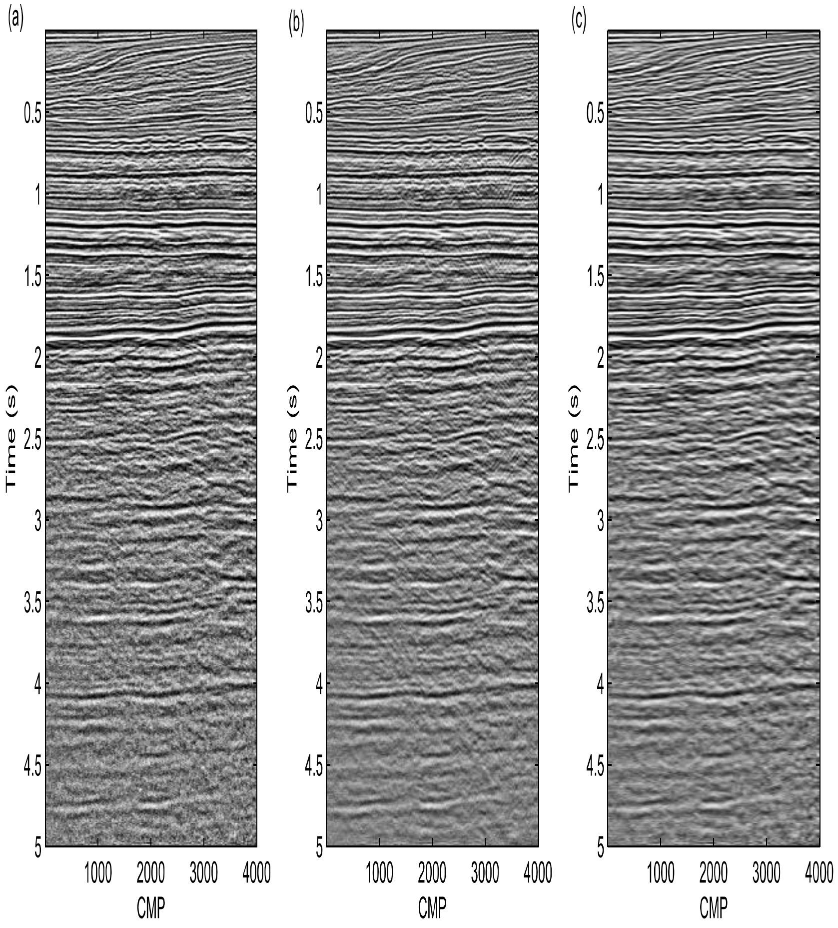

Figure 4.16: (a). Result of f-x EMD. (b). Result of f-x deconvolution. (c). Result of the f-x EEMD thresholding. All three techniques enhance the quality of the original data, especially in the deep part.

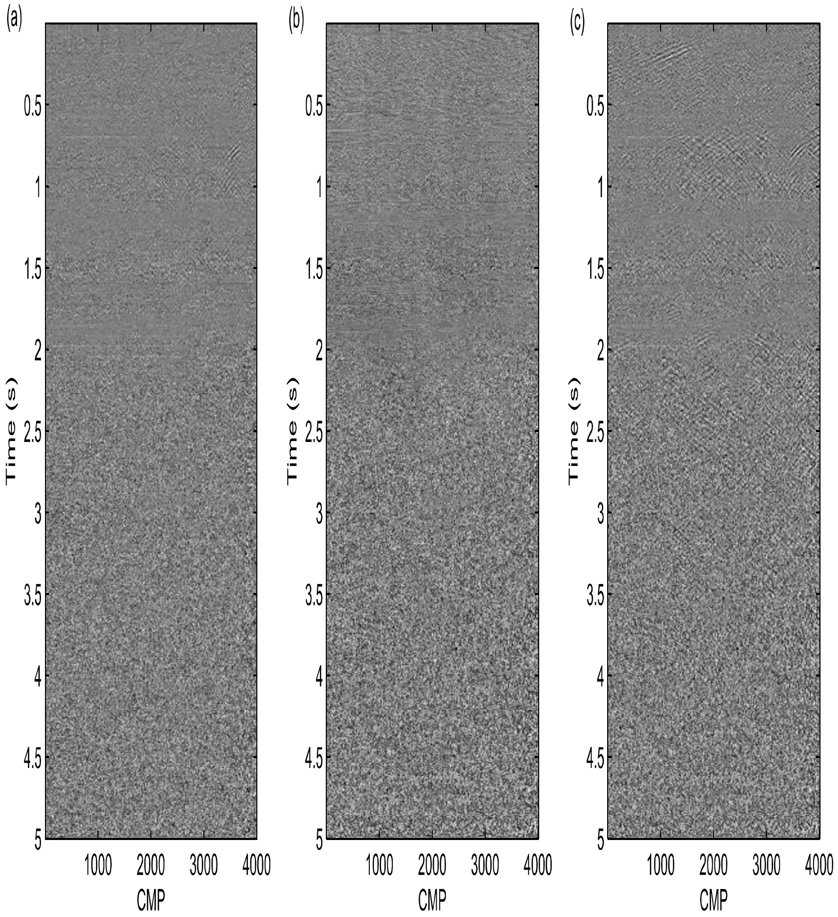

Figure 4.17: (a). Difference section of f-x EMD. (b). Difference section of f-x deconvolution. (c). Difference section of the f-x EEMD thresholding. No reflections are lost in these methods. F-x deconvolution and f-x EEMD thresholding eliminate more noise than f-x EMD.

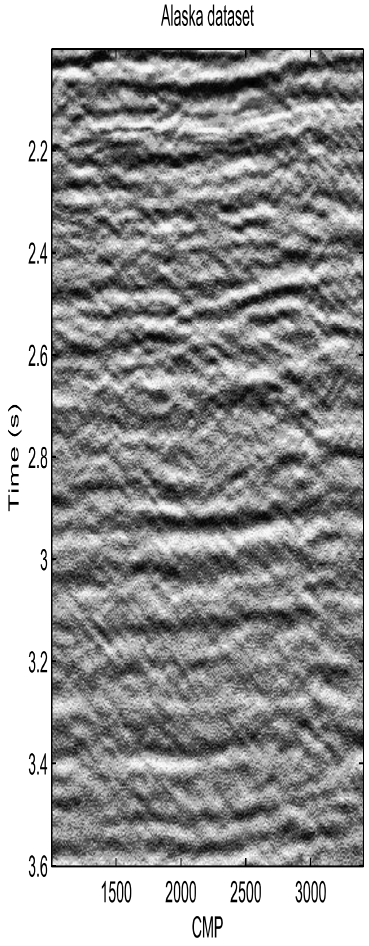

Figure 4.18: Enlarged section of the original data.

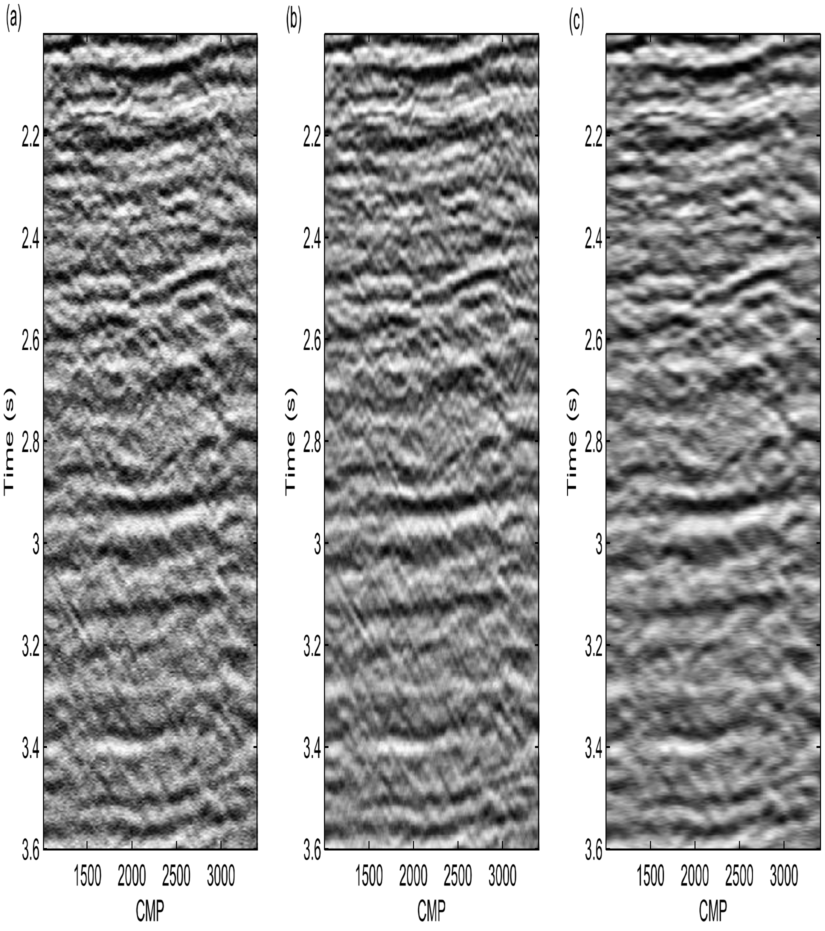

Figure 4.19: (a). Result of f-x EMD. (b). Result of f-x deconvolution. (c). Result of the proposed method. The proposed method obtains the most satisfactory output as the events become clearer than the f-x EMD and f-x deconvolution.

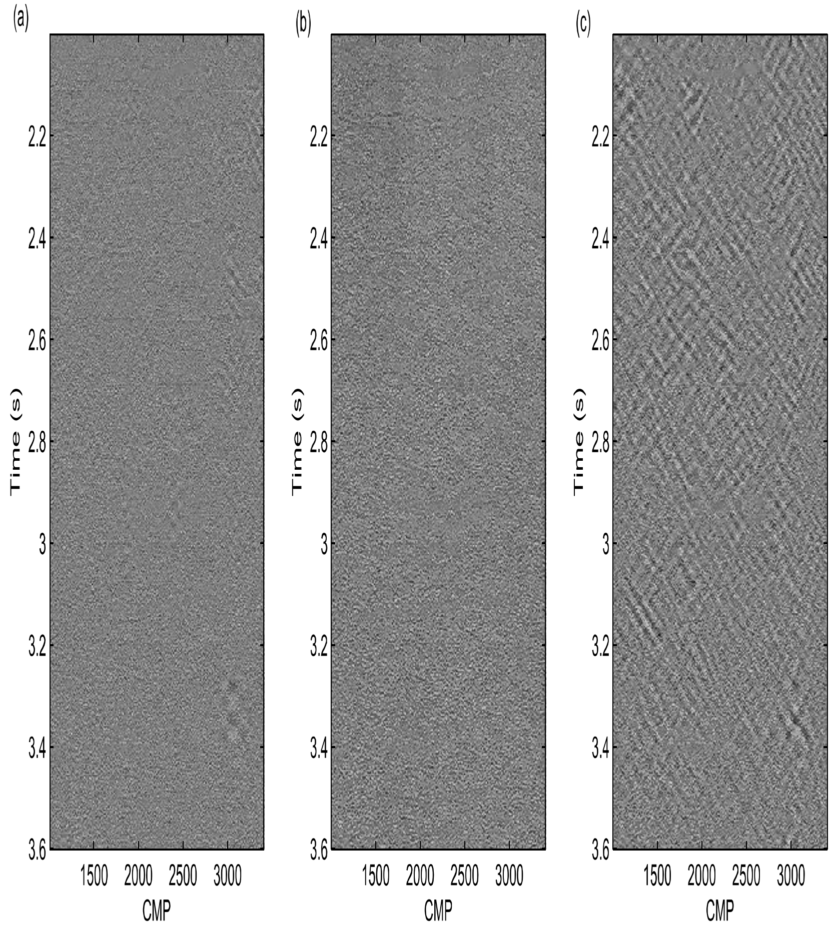

Figure 4.20: a). Difference section of f-x EMD. (b). Difference section of f-x deconvolution. (c). Difference section of the proposed method. F-x EMD suppresses partial random and coherence noise. F-x deconvolution reduces most random noise without any dipping events. The proposed method eliminates the random noise as well as the coherence noise, like the dipping noise.

the synthetic data exactly, so it only needs a small wavelet dictionary to process. In the microseismic example, basis pursuit requires a large Ricker wavelet dictionary to match the test events, therefore it is about 15 to 20 times slower than the EEMD thresholding.

Kopsinis and McLaughlin (2008b, 2009) first investigate the iterative EMD denoising, and discover that the averaging on different noisy versions by altering the IMF1 of input signal can increase the SNR of the final output. Although this approach improves the original EMD denoising, it has an assumption that there is only noise in IMF1 of the input signal (low SNR case). Based on this investigation, they further proposed the 'clear iterative EMD denoising technique' to handle the high SNR case. Our proposed EEMD denoising method is effective for both high and low SNR cases. We create the different noisy version of the target signal by adding the IMF1 of white noise. Based on the dyadic filter structure of EMD, the IMF1 of white Gaussian noise matches along with the information from half Nyquist to Nyquist frequency, and the added noise can be easily smoothed over by the final bandpass filter.

The f-x EEMD thresholding manifests its effectiveness in the Alaska data. It combines the advantages of f-x deconvolution and f-x EMD. The predominance of the AR model in the f-x domain is acceptable because of its excellent noise reduction and time efficient characteristics. However, its theory needs regular trace spacing, and the results of f-x deconvolution can enhance any coherent noise as well, like multiples and dipping energy. Trying EMD as an alternative operator in the f-x domain, Bekara and Van der Baan (2009) elaborately discuss the advantages of f-x EMD in different kinds of datasets over f-x deconvolution. They conclude that f-x EMD acts as an auto-adaptive wavenumber filter to remove the random and steeply dipping coherence noise. The theory of proposed f-x EEMD thresholding is similar as f-x EMD. Furthermore it improves the performance of f-x EMD by more parameter controls. The parameter σ is related to the noise level in the seismic data. Random noise pollutes the whole t-x domain as well as the f-x domain, therefore thresholding on each IMF in each constant frequency slice is more effective for suppressing random noise than only deleting IMF1. The parameters $m1$ and $m2$, they give a flexible control for the dip filter range. The Alaska data illustrates the dipping coherent noise is not totally limited in the IMF1 of each frequency in the f-x domain. The proposed f-x EEMD thresholding is more powerful in reducing the dipping coherent noise.

4.5 Conclusion

EEMD thresholding is a useful tool for suppressing random noise in the signals of different SNR cases, as it has capability to distinguishes the signal information and noise in each IMF. Apply the proposed method in the f-x domain, f-x EEMD thresholding acts as a sophisticated wave-number filter, which removes both random and dipping coherent noise in seismic data. f-x EEMD thresholding is an improved version of f-x EMD filter, therefore it invokes no piecewise-stationarity assumption, and it is less sensitive to irregular spatial sampling than f-x deconvolution. With more parameters control, f-x EEMD thresholding enhances the flexibilities of f-x EMD filter. The synthetic, microseismic and seismic examples illustrate the good performance of our proposed methods.

Chapter 5

Interpolation artifacts and bidimensional ensemble empirical mode decomposition[1]

Summary

Scatter point interpolation plays a significant role in bidimensional empirical mode decomposition (BEMD). The type of interpolant has a large influence on the final decomposition results and should ideally be adapted to the target image. Fortunately, interpolation artifacts can be reduced by bidimensional ensemble empirical mode decomposition (BEEMD).

5.1 Introduction

As a 2D extension of EMD, Linderhed (2002, 2005) and Nunes et al. (2003, 2005) proposed the Bidimensional Empirical Mode Decomposition (BEMD) algorithm, which decomposes images into Bidimensional Intrinsic Mode Functions (BIMFs). Initial BIMFs contain the higher spatial and frequency information; the later BIMFs and the residual are mainly composed of slow oscillations which illustrate the major

---

[1] A part version of this chapter has been published. Jiajun Han and Mirko van der Baan, CSEG2014

trend of the original image. Like IMFs, BIMFs are potentially helpful for signal analysis. It has for instance been used for rainfall analysis, image enhancement and geologic feature extraction (Sinclair and Pegram, 2005; Qin et al., 2008; Huang et al., 2010).

Obligatory choices in any BEMD implementation surround decisions on how to detect local extrema, how to interpolate scattered data points, and what stopping criteria to use. These decisions will impact the kind of BIMFs that are ultimately extracted. Nunes and Delechelle (2009) discuss extrema point detection based on neighboring window comparison and various morphological operations. For the scattered data interpolation, thin-plate spline radial basis function (TPS-RBF), cubic spline, B-spline and Delaunay triangulation methods are usually used in BEMD applications (Huang et al., 2010; Nunes and Delechelle, 2009; Damerval et al., 2005). Instead of scatter point interpolation, finite-element method and order-statistics filter are employed to estimate the upper and lower envelopes for computational consider (Xu et al., 2006; Bhuiyan et al., 2008). Stopping criteria control the number of iterations thus balancing performance versus computation time.

Like EMD, mode mixing may restrict application of BEMD. Overshoot and undershoot may occur as well depending on the type of chosen interpolant, leading to blurred and unrepresentive BIMFs.

In this chapter, we first illustrate the advantage of BEMD over EMD on 2D images. And then we compare Delaunay triangulation, cubic and TPS-RBF interpolation methods to illustrate how they may impact analysis results. Next, we apply BEMD using these interpolants onto seismic data to demonstrate potential pitfalls. Finally, we propose bidimensional enemble empirical mode decomposition (BEEMD) and illustrate how it can improve image analysis by reducing interpolation artifacts.

5.2 Bidimensional empirical mode decomposition

BEMD decomposes an image into its Bidimensional Intrinsic Mode Functions (BIMFs) based on local spatial and spectral scales. As an extension of EMD, the definition of

BEMD is based on the paper of Huang et al. (1998), and the sifting process can be described as below (Linderhed, 2002; Nunes and Delechelle, 2009) :

(1). Find all the local maxima and all the local minima of the image.

(2). Create upper and lower envelopes by proper interpolation of the local maxima and minima of the image.

(3). For each point, take the mean envelope of the upper and the lower envelopes.

(4). Subtract the mean envelope from the input image.

(5). Check the residual between the original image and the mean image; determine whether it meets the stopping criteria; If not, repeat the process from step (1) with the residual as the new input image. If yes, define the residual as a BIMF and subtract it from the input image.

(6). Find next BIMF by starting over from step (1) with the residue between the image and former BIMF as input signal.

Through the sifting procedure above, the mean envelope of each BIMF is guaranteed to be zero or nearly zero, and the BIMFs are locally orthogonal, two properties which are shared with 1D IMFs. The only difference is the number of local extrema and the number of zero crossings; for EMD, the number of local extrema and the number of zero crossings must be equal or differ by at most one, however, due to the properties of an image, it is impossible to satisfy this property for BEMD (Bhuiyan et al., 2008).

Unlike EMD, there is no standard interpolation for BEMD. The users select the interpolation for their own purpose. The first attempt is utilizing TPS-RBF as interpolation, since its smooth feature. However, due to its computation consuming predicament, other interpolants have been employed (Xu et al., 2006; Bhuiyan et al., 2008). Except TPS-RBF, I also test Delaunay triangulation interpolation (Sapidis and Perucchio, 1991) and cubic interpolation for BEMD in this chapter.

Each BIMF contains different frequency and spatial component, thus highlighting different information in the input images. However, the first attempt for decomposing 2D image is applying 1D EMD in particular directions. In next section, we elaborately discuss the advantage of BEMD over 1D EMD for decomposing 2D images.

5.3 Why BEMD?

In geophysics area, Magrin-Chagnolleau and Baraniuk (1999) and Vasudevan and F.A. (2000) first attempt to decompose the 2D seismic profiles by 1D EMD in vertical direction. With the relatively satisfactory results, they conclude that the new time-frequency attributes after EMD are the potential tools for seismic attribute analysis. These successful applications of 1D EMD in 2D images are because seismic profiles are characterized by a higher lateral continuity and less vertical continuity. Therefore, the decomposition to these 2D images does not need to take care of every directions.

For a normal 2D image, which usually has both vertical and horizonal correlations, only one direction decomposition by 1D EMD may not extract useful information. We take the famous Lena image (Figure 5.1 left) as an example. Our approach for 1D EMD is applying it only in the vertical direction: set the same number of IMFs for each trace and gather them as the whole IMFs for the original image. The output IMFs (Figures 5.1 to 5.3) has blurred areas, and the edge information is not exacted well as expection by the first two IMFs. Moreover, IMF 3 does not tend to be continuous and smooth, especially in the hat part over head. This is mainly because the extrema in each trace does not equal to the extrema of the whole image, and the following sifting process is effected. Liu and Peng (2005) expound this issue in a deeper level, and they find that decomposing images in a single direction by 1D EMD could lose correlations in other directions. Due to the inefficiency of 1D decomposition of Lena image, the first four IMFs do not capture much information as the residual (5.3 right) still resembles the original image.

Next, we apply BEMD, using TPS-RBF as interpolant, on the same Lena image. Since BEMD shares the similar features with EMD, we expect that the former BIMFs contain the higher oscillatory information, which are corresponding the edge information in the original image. Figures 5.4 (left) shows again the Lena image. Figures 5.4 (right) to 5.6 show the first 4 BIMFs and the final residual. Different BIMFs contain different frequencies and local spatial information: BIMF 1 represents the highest oscillation component, which can highlight edges in the images;

BIMF 2 and BIMF 3 can also assist to detect edge information because they contain higher spatial and frequency content; the later BIMFs and residual are mainly composed of slow oscillations which illustrate the major trend of the original image.

From the comparison, BEMD preserves the correlations of both directions (vertical and horizontal) much better than 1D EMD for the Lena image. This makes BEMD is a more suitable signal tool for 2D images. As each BIMF contains the special frequencies and spatial information, Sinclair and Pegram (2005), Qin et al. (2008) and Huang et al. (2010) have already applied BEMD for rainfall analysis, image enhancement and geologic feature extraction. Although BEMD is a powerful image tool, its application in geophysics is rare. The serious problem is scatter point interpolation, the type of chosen interpolant can greatly affect the extracted BIMFs.

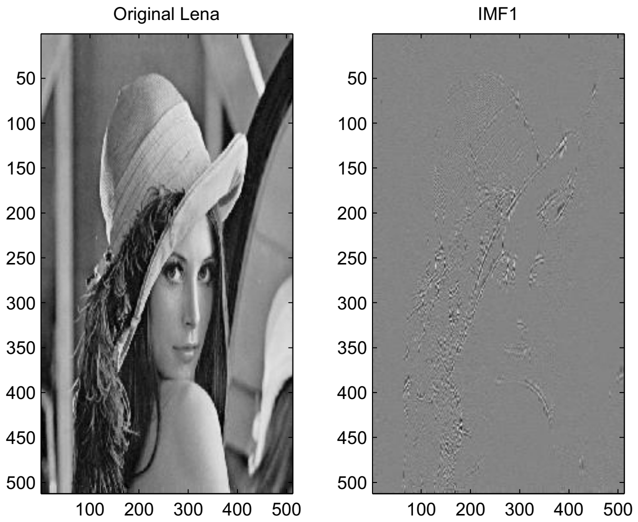

Figure 5.1: Lena image and associated IMF1 after 1D EMD applied in vertical direction. IMF1 tends to by fuzzy, and cannot highlight the boundary information effectively.

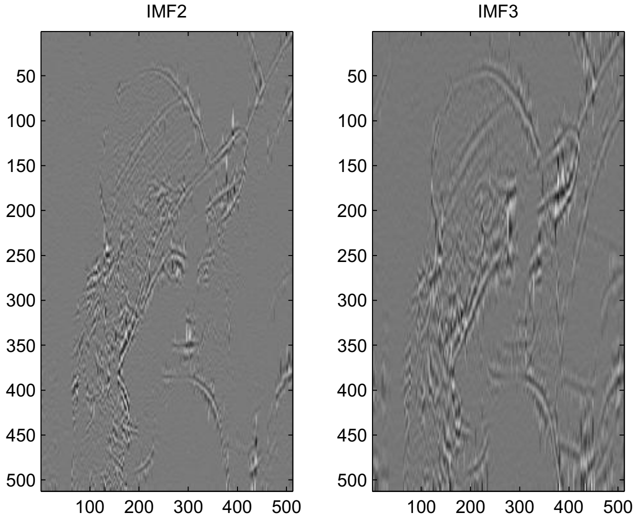

Figure 5.2: IMF2 and IMF3 after 1D EMD applied in vertical direction. More edges are visible.

5.4 Scatter point interpolation and BEEMD

Point interpolation plays a significant role in any BEMD implementation, and the ideal produced envelopes should go through each data point and enwrap the whole

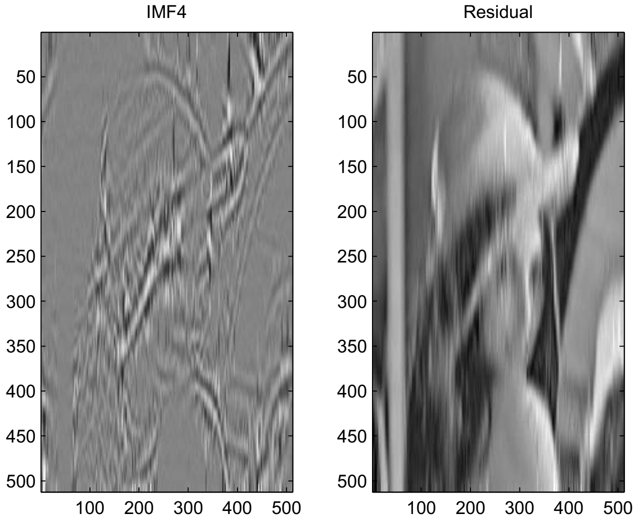

Figure 5.3: IMF4 and residual after 1D EMD applied in vertical direction. IMF4 shows boundaries clearly, but the residual (original image minus IMFs one to four) retains still much of the original information.

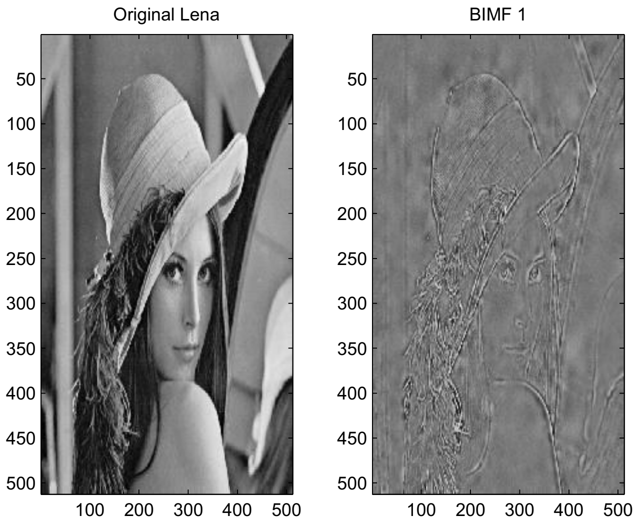

Figure 5.4: Lena image and BIMF1. BIMF1 highlights edges in the original data.

image. Different interpolation methods are suited for different images. For smooth images, the aim of interpolation is to find a stable, continuous and smooth envelope. On the other hand, for images which have many discontinuities, the interpolation should avoid overshoot and undershoot problems, whereas smooth interpolation can not.

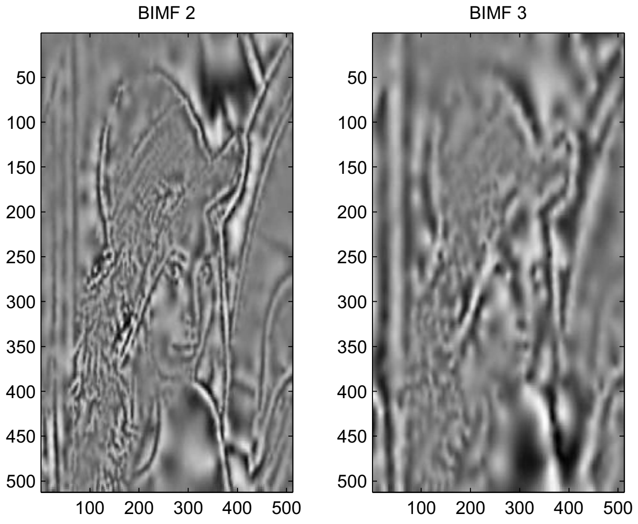

Figure 5.5: BIMF2 and BIMF3. Both contain higher oscillation information to detect boundaries.

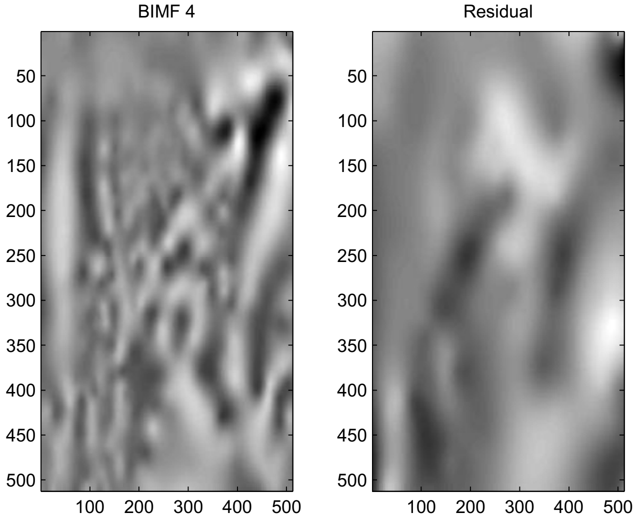

Figure 5.6: BIMF4 and residual. They reflect the main trend of the input image.

To obtain the upper and lower envelopes, we test three interpolation methods: Delaunay triangulation interpolation (Sapidis and Perucchio, 1991), cubic interpolation and thin-plate spline radial basis function (TPS-RBF) (Bhuiyan et al., 2009).

Figure 5.7(a) is a synthetic image with smooth features. The blue dots are local maxima and red dots are local minima. Figures 5.7(b)-5.7(d) are envelopes obtained using all three interpolants. The envelopes obtained by Delaunay triangulation interpolation manifest sharp and discontinuous features; the ones obtained by cubic interpolation tend to be smoother; from comparison, the envelopes of TPS-RBF show the smoothest results, as the second derivative is guaranteed to be continuous. In this case, TPS-RBF preserves the features contained in the smooth test image best.

Another synthetic image with discontinuous features is shown in Figure 5.8(a). In this case, cubic interpolation (Figure 5.8(c)) and TPS-RBF (Figure 5.8(d)) exhibit overshoot and undershoot artifacts; however, Delaunay triangulation (Figure 5.8(b)) produces the most satisfactory image.

5.4.1 Application of BEMD on seismic data

Figure 5.9 shows an image of seismic data representing two geologic subsurface features, namely a buried channel and a fault. Both features are identified by ar-

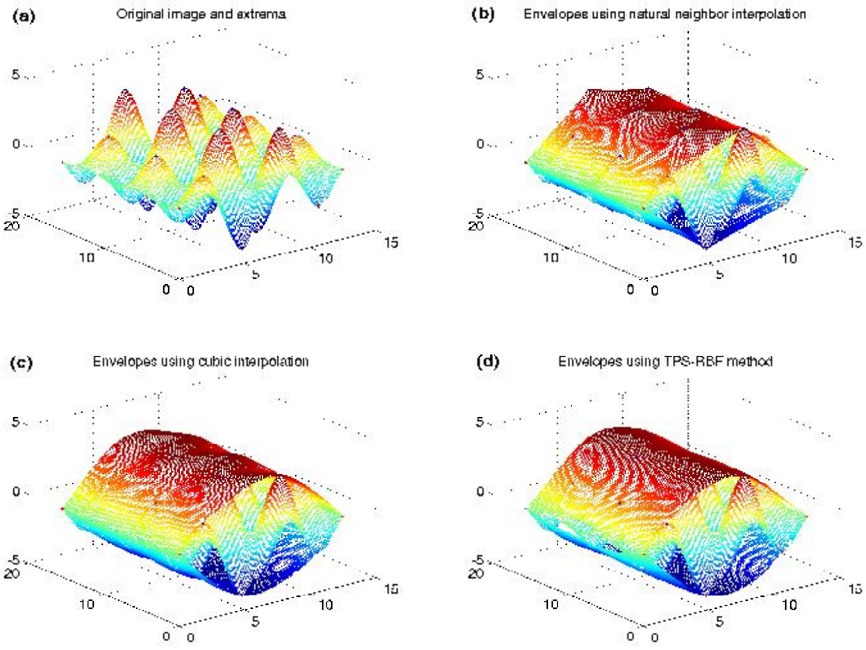

Figure 5.7: Smooth test image. (a). Test image. Blue dots are local maxima and red dots are local minima. (b). Delaunay triangulation creates discontinuous slopes between each triangle part; (c). Cubic spline produces the smoother envelopes; (d). TPS-RBF yields the smoothest envelopes.

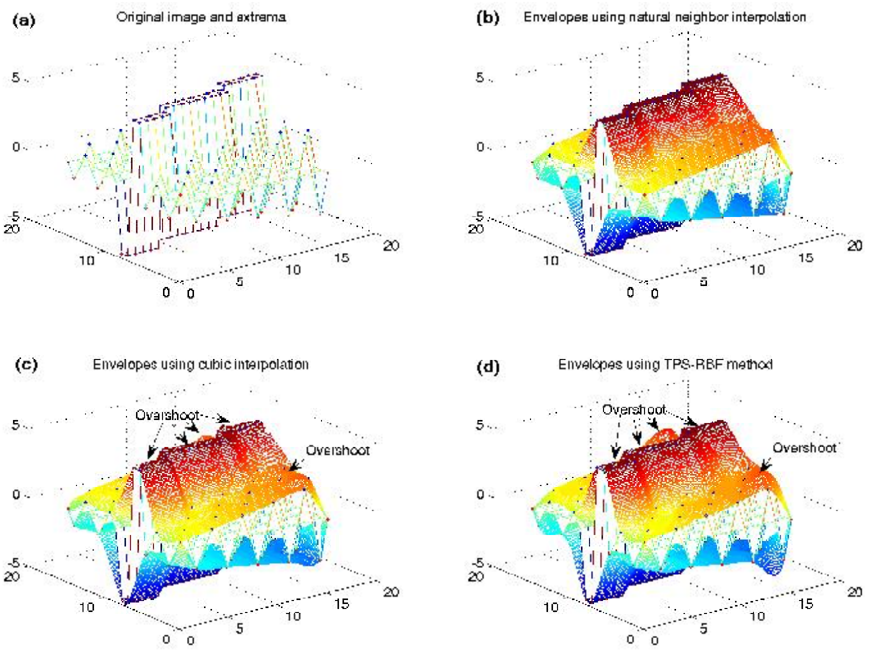

Figure 5.8: Test image with discontinuities. (a) Test image. Blue dots are local maxima and red dots are local minima. (b). Delaunay triangulation produces envelopes without overshoot; (c). cubic spline creates smoother envelopes with only some overshoot; (d). TPS-RBF produces the smoothest envelopes with severe overshoot.

rows. The image contains both smooth and sharply delineated features, making this a relevant test for identifying the effect of the interpolant on the resulting BIMFs.

Figures 5.10(a) to 5.10(c) display the first BIMF component of BEMD using 3 different interpolation methods. The outputs from Delaunay triangulation (Figure 5.10(a)) and cubic interpolation (Figure 5.10(b)) are similar. They both highlight the channel and fault features clearly. The one from TPS-RBF (Figure 5.10(c)) fares less well. Overshoot and undershoot make the boundaries of the channel fuzzy, and there is no clear identification of the fault. The fault is not visible on the later BIMFs either.

In the next subsection we demonstrate how noise-injection using bidimensional ensemble EMD can alleviate interpolation artifacts, thereby facilitating any interpretation without the need to adapt the interpolant each time to the image.

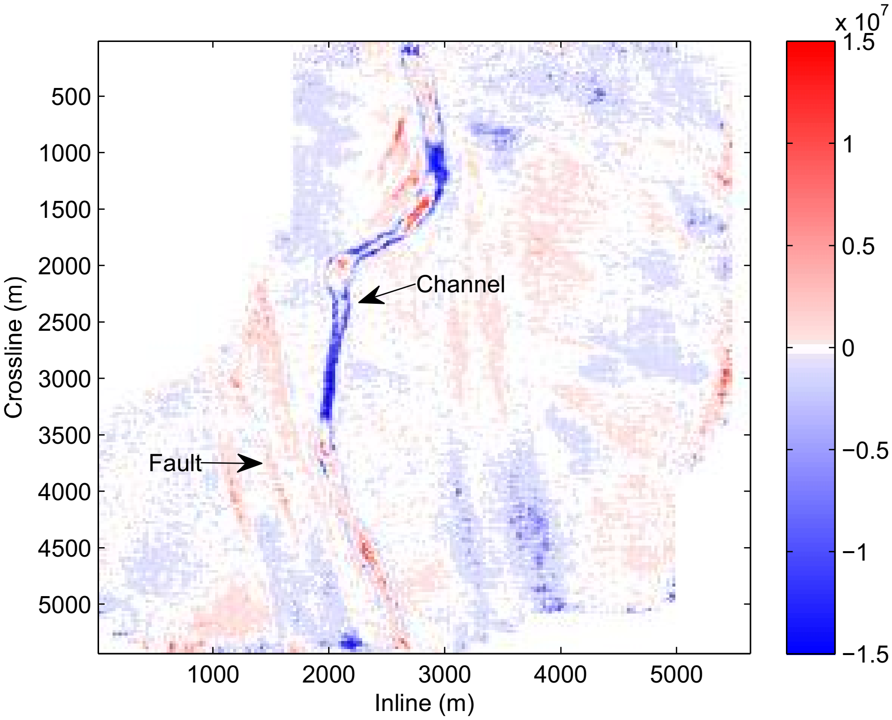

Figure 5.9: Seismic test image with smooth and discontinuous features. The channel and subtle fault are identified by arrows.

5.4.2 Bidimensional ensemble empirical mode decomposition

Based on the dyadic filter bank of EMD (Flandrin et al., 2004b), Wu and Huang (2009a) propose the ensemble empirical mode decomposition (EEMD), which enhances the application of EMD. Following their idea, we propose the bidimensional ensemble empirical mode decomposition (BEEMD).

BEEMD is a noise-assisted analysis method. It injects noise into the decomposition algorithm to stabilize its performance. The implementation procedure for BEEMD is simple:

(1). Add a fixed percentage of Gaussian white noise onto the image,

(2). Decompose the resulting signal into BIMFs,

(3). Repeat steps (1) and (2) several times, using different noise realizations;

(4). Obtain the ensemble averages of the corresponding individual BIMFs as the final result.

The added Gaussian white noise series are zero mean with a constant flat spectral and spatial spectrum. Their contribution thus cancels out and does not introduce any image components not already present in the original image, which is helpful to avoid mode mixing.

5.4.3 Application BEEMD on seismic data

We apply BEEMD algorithm onto Figure 5.9 with all three interpolants using 50 noise realizations with 10% added noise. This time, all BIMF1 (Figure 5.10(d) to Figure 5.10(f)) show similar results, always identifying both the fault and channel features. Both Delaunay triangulation and cubic interpolation produce similar results to a single BEMD; yet the TPS-RBF outcome has been greatly improved by eliminating most interpolation artifacts due to overshoot and undershoot (compare with Figure 5.10(c)).

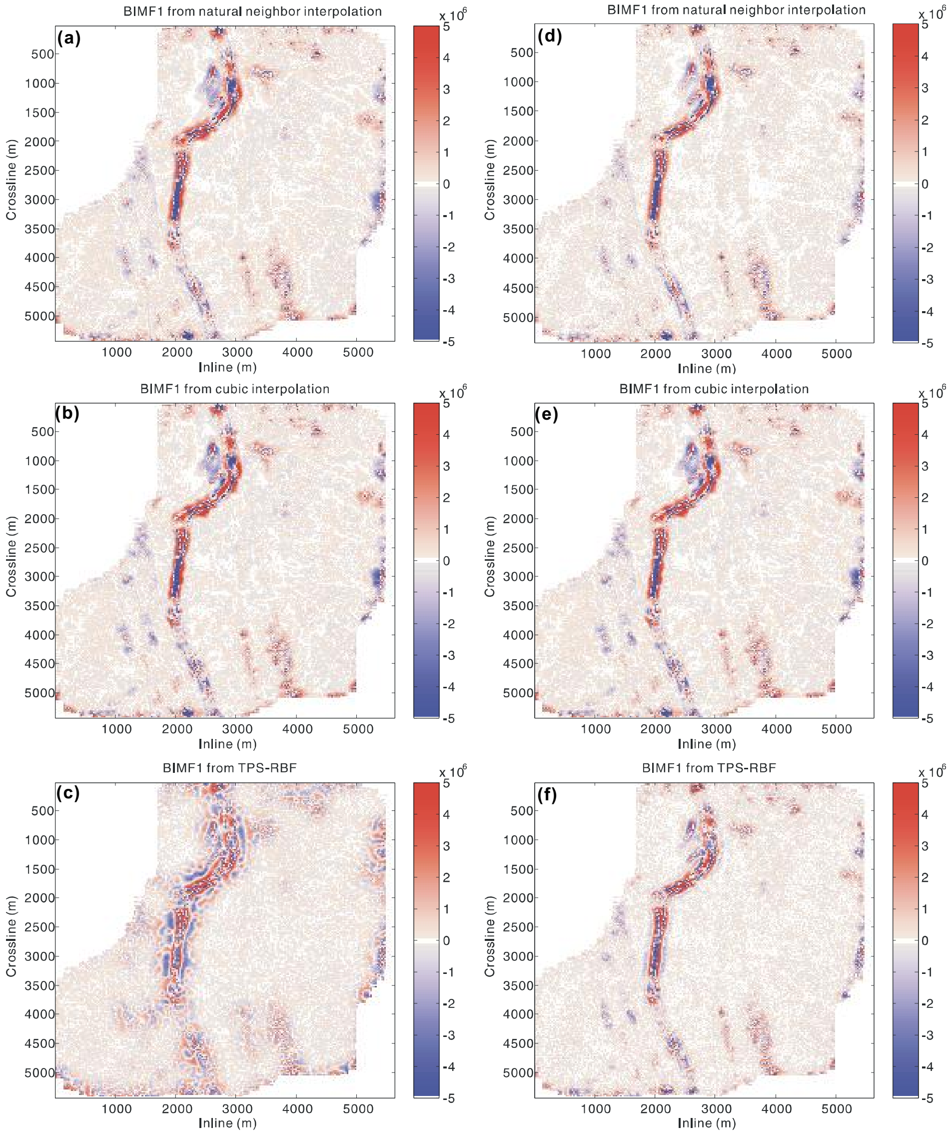

BIMF1 from natural neighbor interpolation

BIMF1 from cubic interpolation

BIMF1 from TPS-RBF

Figure 5.10: (a) to (c) are BIMF1 after BEMD results using Delaunay triangulation, cubic interpolation and TPS-RBF, respectively. The outputs from Delaunay triangulation and cubic interpolation highlight the channel and fault features. Overshoot and undershoot artifacts spread out the channel boundaries in TPS-RBF method. (d) to (f) are BIMF1 after BEEMD with 20 realizations using Delaunay triangulation, cubic interpolation, and TPS-RBF respectively. All three interpolants now produce similar results.

5.5 Conclusion

BEMD can aid in image analysis; yet the type of chosen interpolant can greatly affect the extracted BIMFs. Non-smooth interpolants such as Delaunay triangulation are best for images with many sharply delineated features and discontinuities. Very smooth interpolants such as TPS-RBF are superior if inherent features exhibit smooth gradients as well or if instantaneous frequencies are also desired. Cubic splines seem to cover a convenient middle road, rendering them suitable as all-purpose interpolants.

Ideally however the interpolant is adapted to each image, making automated interpretations more challenging. On the other hand noise-injection using bidimensional ensemble empirical mode decomposition (BEEMD) can alleviate many interpolation artifacts, thereby facilitating any interpretation without the need to adapt the interpolant each time to the image.

Chapter 6

Bidimensional empirical mode decomposition thresholding

6.1 Introduction

EMD acts essentially as a dyadic filter bank for white Gaussian noise (Flandrin et al., 2004a), and the energy distribution of each IMF is based on equation 4.1. As its 2D extension, how does BEMD act on white Gaussian noise? To the best of my knowledge, the only research on the characteristics of BEMD on Gaussian noise is from Delechelle et al. (2005). Their work selects thin-plate spline radial basis function (TPS-RBF) as interpolant for BEMD, and find a approximate relationship between the average number of extrema for each BIMF versus the BIMF order.

In this chapter, we first employ Monte Carlo simulations to find the BEMD characteristic on white Gaussian noise. After finding the energy distribution of each BIMF, we propose the BEMD thresholding method, following the idea of EMD thresholding in chapter 4, to attenuate random noise in seismic data. The field data examples demonstrate the good performance of the proposed method.

6.2 BEMD analysis of white Gaussian noise

For the Monte Carlo simulations, we set the size of white Gaussian noise to 100×100, and 50 independent white Gaussian noise have been generated for stabilizing the final result. For EMD, the IMF energy distributions vary mainly depending on the number of sifting iterations for each extracted IMF (Kopsinis and McLaughlin, 2008a). This is equally applicable to the BEMD case. Figure 6.1 shows how BIMF energy distribution varies with the number of sifting iteration. The simulation utilizes the cubic interpolant for BEMD implementation, and the y axis of Figure 6.1 is scaling to logarithm 2 of energy. With the number of sifting iteration increasing, the energy distribution of every two adjacent sifting iteration become closer. This indicates the extracted BIMFs tend towards stability after the certain number of sifting iteration. We select the sifting iteration as 10 to extract each BIMF for the following tests; this selection is considered to balance the BEMD performance versus computation time.

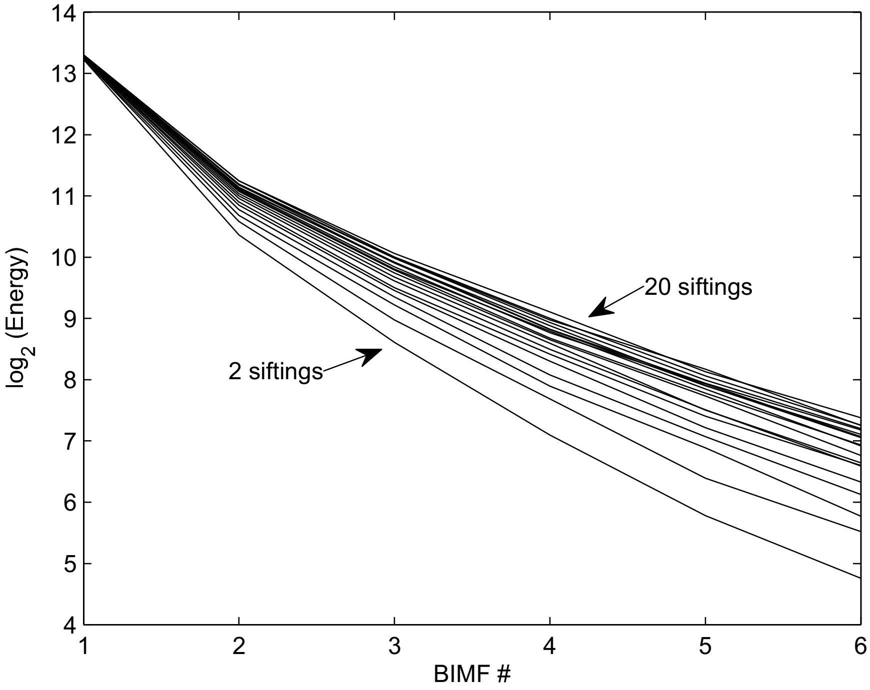

Figure 6.1: BIMF energy distributions of white Gaussian noise. The distributions vary depending on the number of sifting iterations for extracting each BIMF.

Figure 6.2 (a) to (e) show the 2D frequency spectrum for BIMF1 to BIMF6 on white Gaussian noise, note that this is the averaged result over 50 realizations and all subfigures are shown in the same amplitude scale. As evidenced in Figure

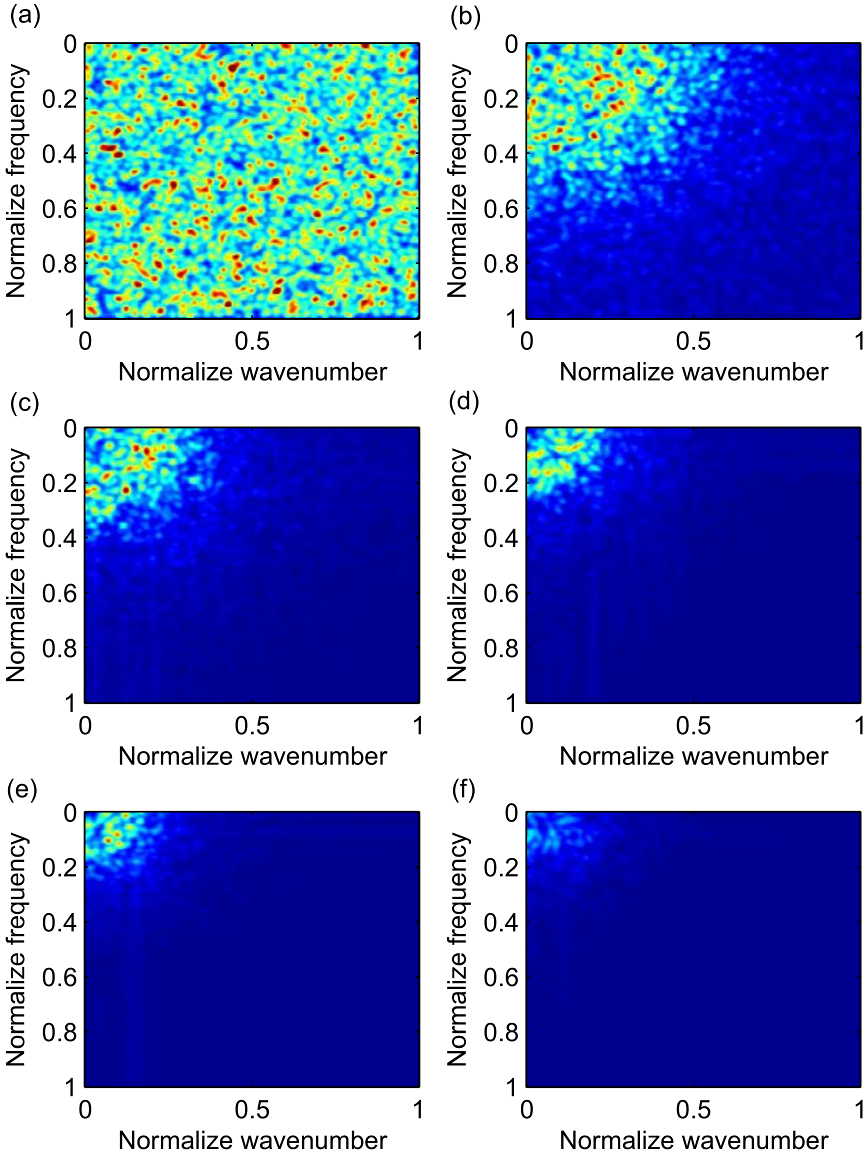

Figure 6.2: 2D frequency spectrum of each BIMF. (a). BIMF1. (b). BIMF2. (c). BIMF3. (d). BIMF4. (e). BIMF5. (f). BIMF6.

6.2, BEMD can be interpreted as the 2D frequency output of some equivalent filter. Indeed, while the filter associated with BIMF1 is essentially highpass filter, although it contains a non-negligible information of lower frequency, the higher order BIMFs are characterized by a set of overlapping filters. This filter bank structure which is reminiscent of what is observed in 2D wavelet decomposition in similar situations.

Flandrin et al. (2004a) find that EMD acts as a constant-Q bandpass filters, and the value of Q approximates 2 through examining the zero-crossings of each IMF. As zero-crossings is hard to define in 2D image, we calculate the energy distribution of each BIMF to investigate the BEMD characteristics. The dot line shown in Figure 6.3 is the BIMFs energy distribution using cubic interpolant for BEMD implementation. As there is no standard interpolants for BEMD, we also calculate the cases of TPS-RBF (solid line) and Delaunay triangulation (dash line). These energy distributions have slight differences, but have one identify feature: the energy distributions tend to be linear from the second to the last BIMF, except BIMF1. This result exactly matches the EMD case (Flandrin et al., 2004a; Kopsinis and McLaughlin, 2009), therefore we can calculate the BIMFs energy distribution on white Gaussian noise based on equation 4.1, which is the equation of IMFs energy distribution in 1D EMD case.

If cubic interpolant is chosen for BEMD implementation,

$$E_k^2 = E_1^2 \times 1.16 \times 2.65^{-k}, k = 2, 3...6. \tag{6.1}$$

If TPS-RBF is chosen

$$E_k^2 = E_1^2 \times 1.33 \times 2.56^{-k}, k = 2, 3...6. \tag{6.2}$$

If Delaunay triangulation is chosen

$$E_k^2 = E_1^2 \times 1.33 \times 3.27^{-k}, k = 2, 3...6. \tag{6.3}$$

where E_k^2 is the energy of the $k-th$ BIMF. From the above equations, the energy distributions of each BIMF are similar as the EMD case, no matter what interpolant is chosen. Therefore, BEMD manifests like a constant-Q, wavelet-like, filter bank

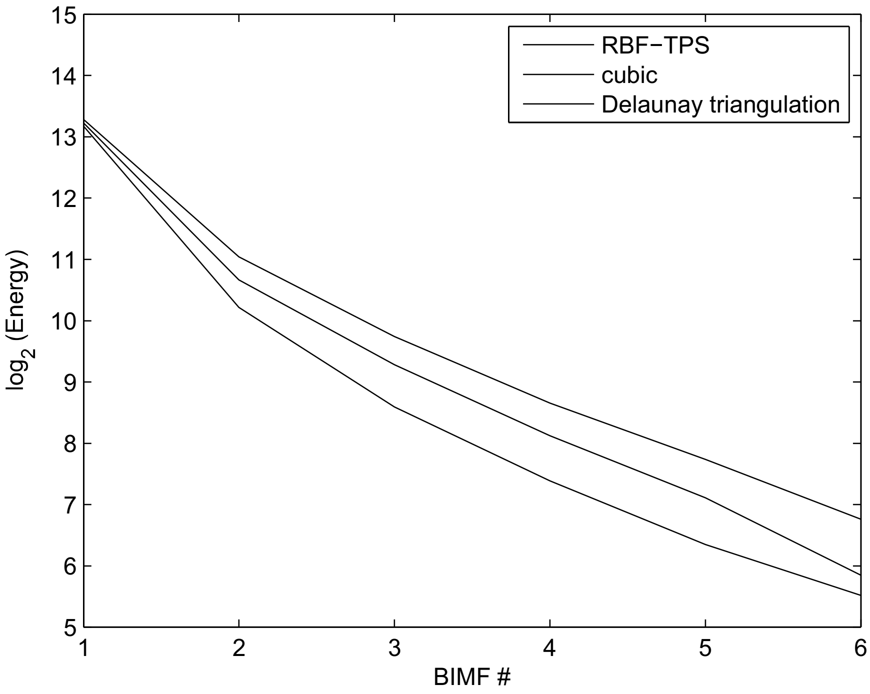

Figure 6.3: BIMF energy distributions of white Gaussian noise. Each BIMF is extracted with 10 sifting iterations. The solid line represents the TPS-RBF for BEMD implementation, dot line is for cubic interpolant, and dash line stands for Delaunay triangulation.

for a 2D image, and the Q value varies with the different interpolants.

6.3 BEMD thresholding

After obtaining the energy distribution of each BIMF, we propose the BEMD thresholding method following the idea of chapter 4. As the BIMFs resemble a wavelet-like filter bank for a 2D image, the first BIMF energy E_1^2 of the input image S can be estimated using the same robust estimator as equation 4.2:

$$E_1^2 = (median(|BIMF1(i)|)/0.6755)^2, \quad i = 1,2...n. \tag{6.4}$$

where n is the total number of the input image samples. Then we can set the adaptive threshold T_k in each BIMF for suppressing the random noise as

$$T_k = \sigma \times \sqrt{(2 \times ln(n))} \times E_k, \tag{6.5}$$

where σ is the main parameter to be set. Equations 6.4 and 6.5 are exactly the same as equations 4.2 and 4.3, and the combination of them is a universal threshold for removing the white Gaussian noise in the wavelet domain (Donoho and Johnstone, 1994; Donoho, 1995).

Following the EMD threshold procedure, the reconstructed image $\hat{S}$ is expressed as

$$\hat{S} = \sum_{k=m1}^{m2} T_k[BIMF_k] + residual. \tag{6.6}$$

The thresholding is only applied between $m1-th$ to $m2-th$ BIMFs, and has no impact on residual. In EMD thresholding (Chapter 4), the decomposition continues until the last IMF or residual only contains at most two extreme. However, this 'complete decomposition' is impracticable for BEMD due to the properties of an image and computation time. In BEMD implementation, we always set the max number of BIMFs to generate before the decomposition; therefore, the residual does not behave like a BIMF and does not follow the equations 6.1 to 6.3.

In the following example section, we select the cubic interpolant for implementing the BEMD thresholding, since it is most time efficient method among all three interpolants.

6.4 Example

6.4.1 Seismic vertical slice

The first example is a stacked seismic profile from Alaska (Geological-Survey, 1981) (Figure 6.4). Although the events become continuous after stacking, random, coherent and background scattered noise still exist, thereby reducing the quality of the seismic data. We set the parameter $m2$ as 7, which means that BEMD decomposes the image into 7 BIMFs with a residual. We set the threshold parameter σ as 0.2, and plot the original and thresholded BIMFs in Figures 6.5 and 6.6. The original

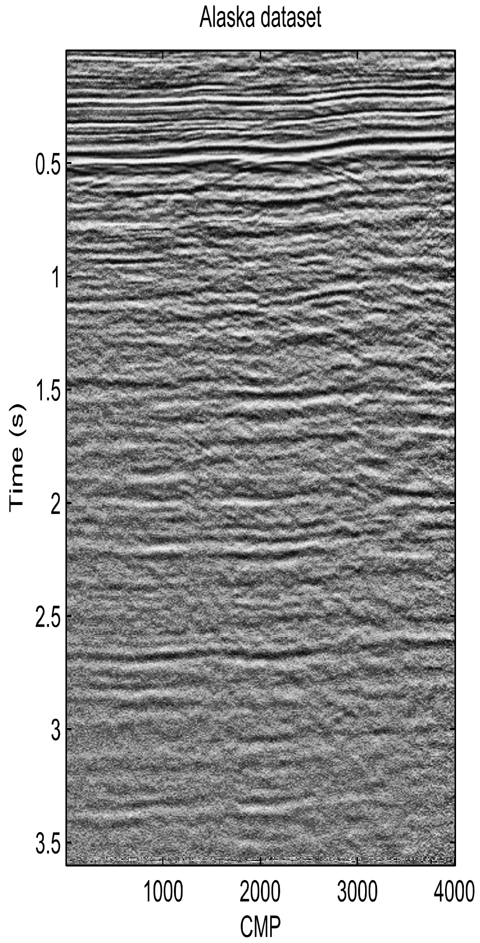

Figure 6.4: Input seismic data from Alaska. The random noise brings down the quality of the data.

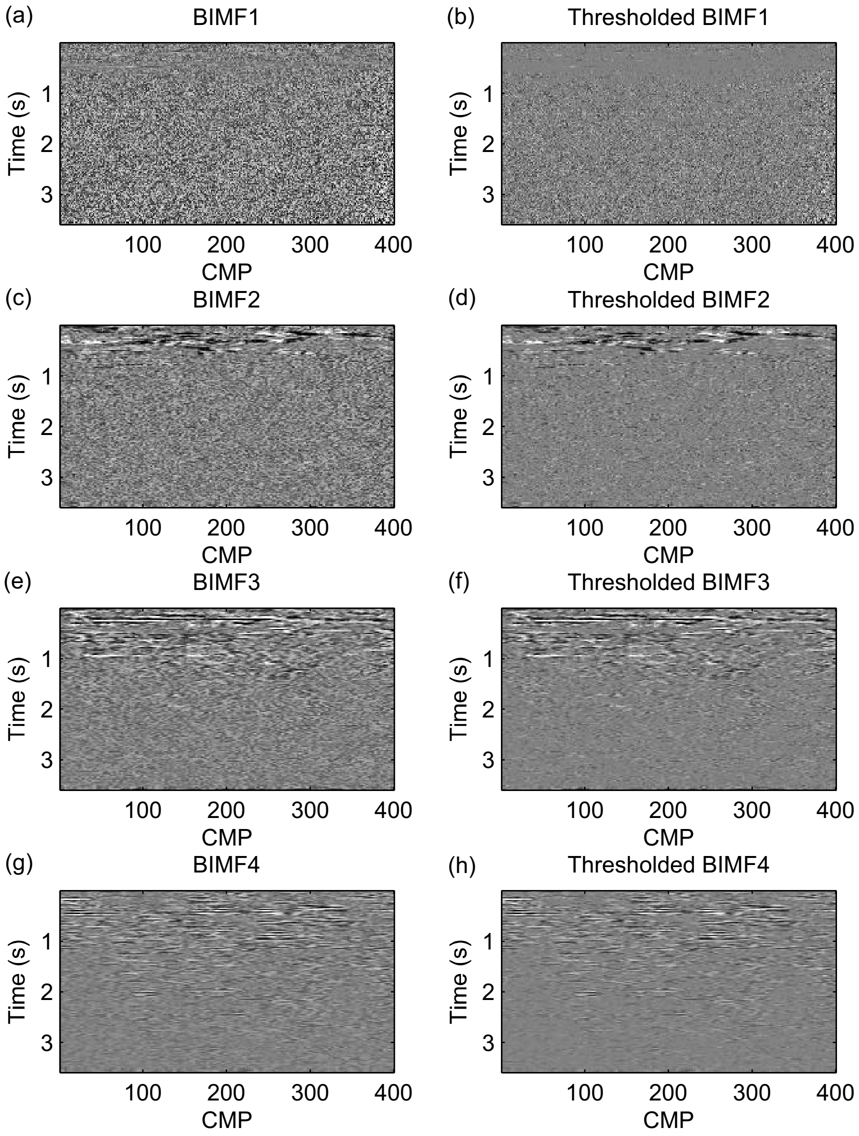

Figure 6.5: (a). BIMF1. (b). Thresholded BIMF1. (c). BIMF2. (d). Thresholded BIMF2. (e). BIMF3. (f). Thresholded BIMF3. (g). BIMF4. (h). Thresholded BIMF4. The thresholding suppresses most of the random noise from BIMF1 to BIMF4.

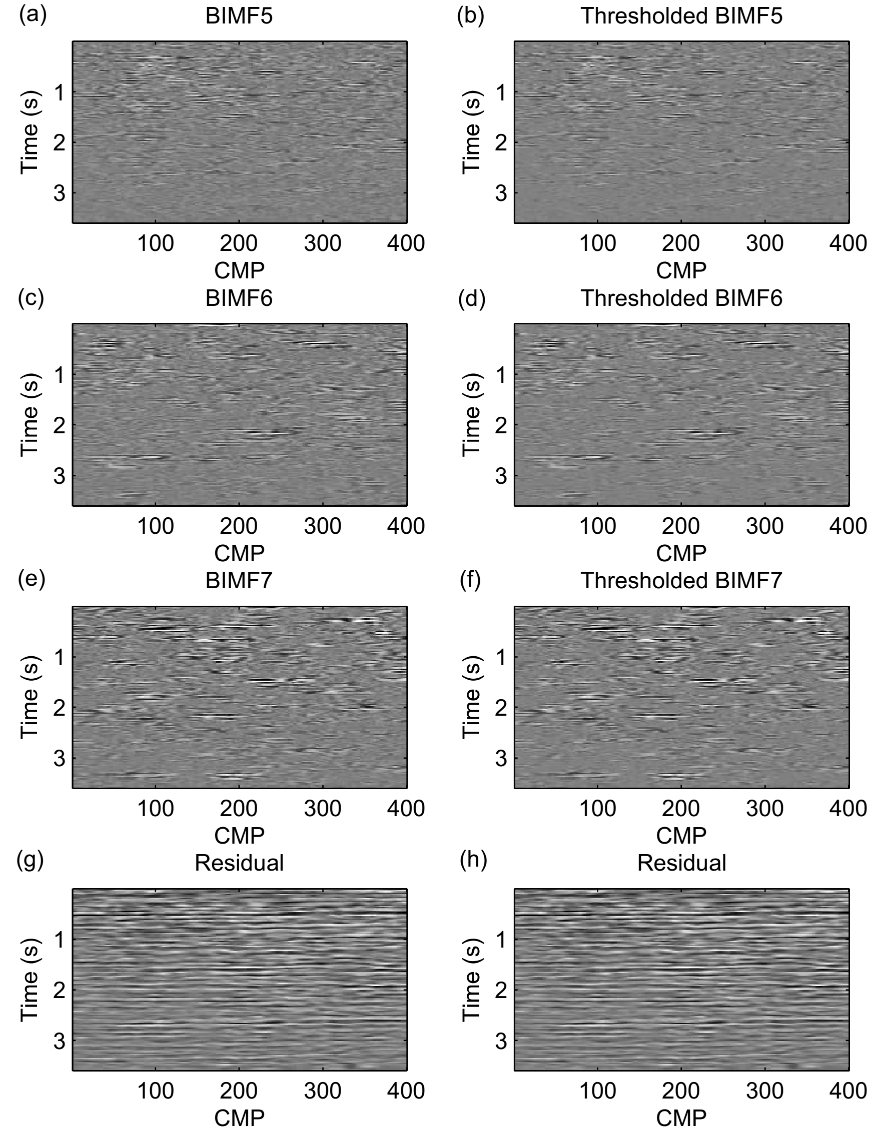

Figure 6.6: (a). BIMF5. (b). Thresholded BIMF5. (c). BIMF6. (d). Thresholded BIMF6. (e). BIMF7. (f). Thresholded BIMF7. (g). Residual. (h). Residual. The thresholding enhances the events energy from BIMF5 to BIMF 7, and has no impact on the residual.

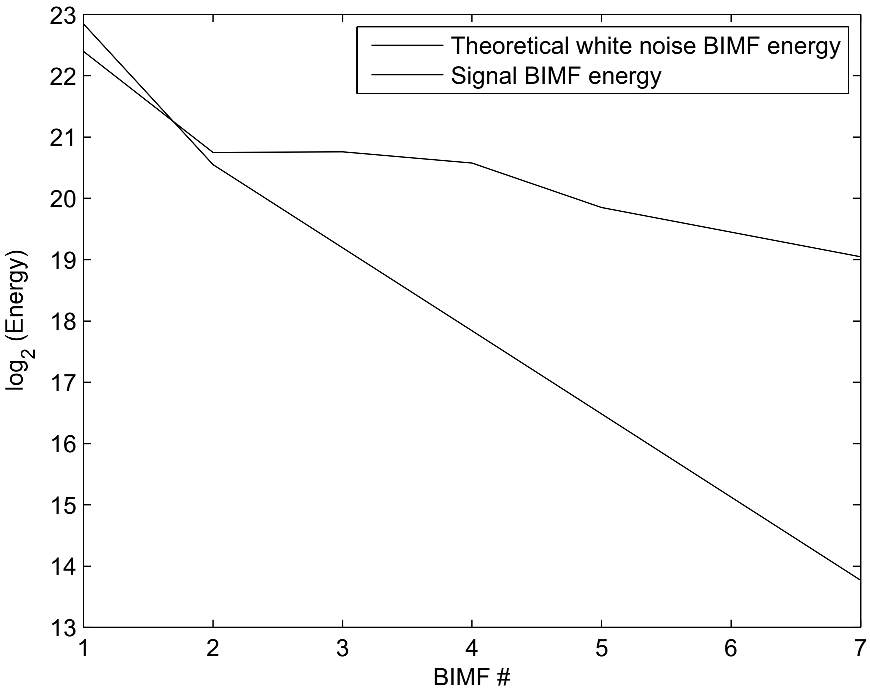

Figure 6.7: The BIMF energy distribution of Figure 6.3 and the theoretical BIMF energy distribution of white Gaussian noise based on equation 6.1.

BIMF1 (Figure 6.5 (a)) contains nearly all the noise. Except a few reflections on the top section, BIMF2 (Figure 6.5 (c)) is nearly all random noise too. Based on the energy distribution of each BIMF, BEMD has capability to distinguish the reflection information and random noise. The thresholding makes the output BIMFs (Figures 6.5 (b),(d),(f),(g) and Figures 6.6 (b), (d) and (f)) get rid of most random noise, and leave the strong reflections. As the residual does not follow the energy distribution of equation 6.1, thresholding has no impact on the residual (Figures 6.6 (g) and (h)).

The theoretical (solid line) and true BIMF energy (dash line) distributions are shown in Figure 6.7. Except the first BIMF energy, the energy of other BIMFs are all above the theoretical line. Therefore, we set $m1$ as 2, which means remove BIMF1 and the thresholding is applied from BIMF2 to the last BIMF. The BEMD thresholding output is shown in Figure 6.8(c).

Since the proposed method is 2D image denoising technique, we compare its result with two classic methods, local median filter (Bednar, 1983) and local SVD filter

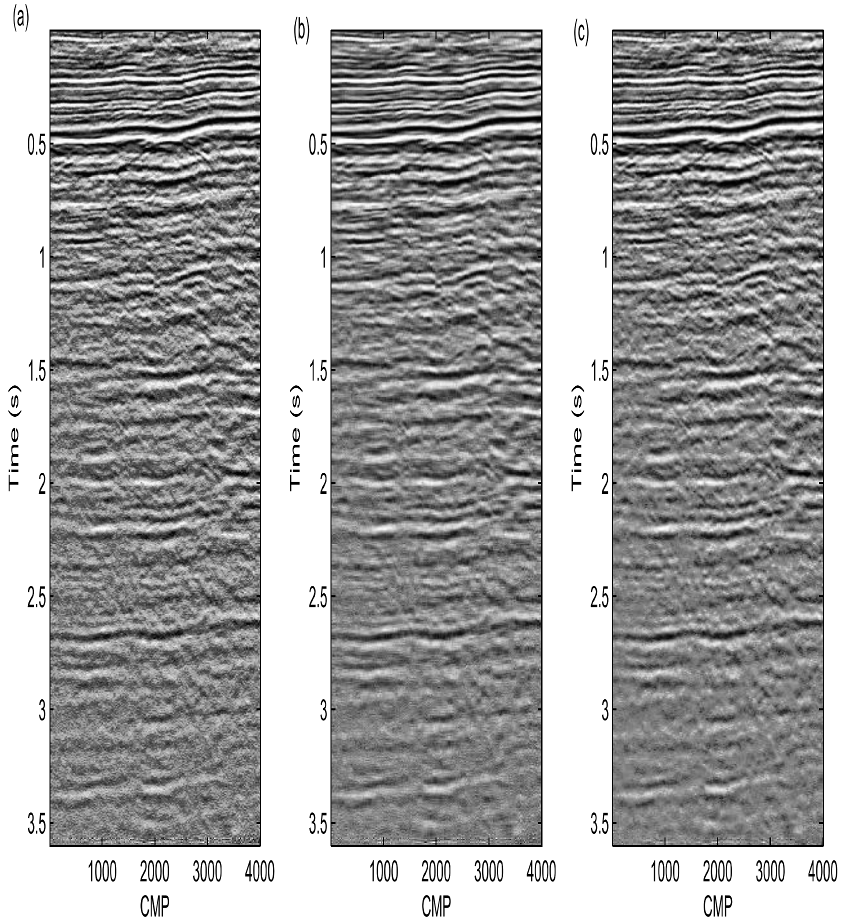

Figure 6.8: (a). Result of local median filter. (b). Result of local SVD filter. (c). Result of BEMD thresholding with $m1$ =2, $m2$ = 7 and σ = 0.1. All three method upgrades the quality of data. BEMD thresholding and local SVD filter have better performance than local median filter.

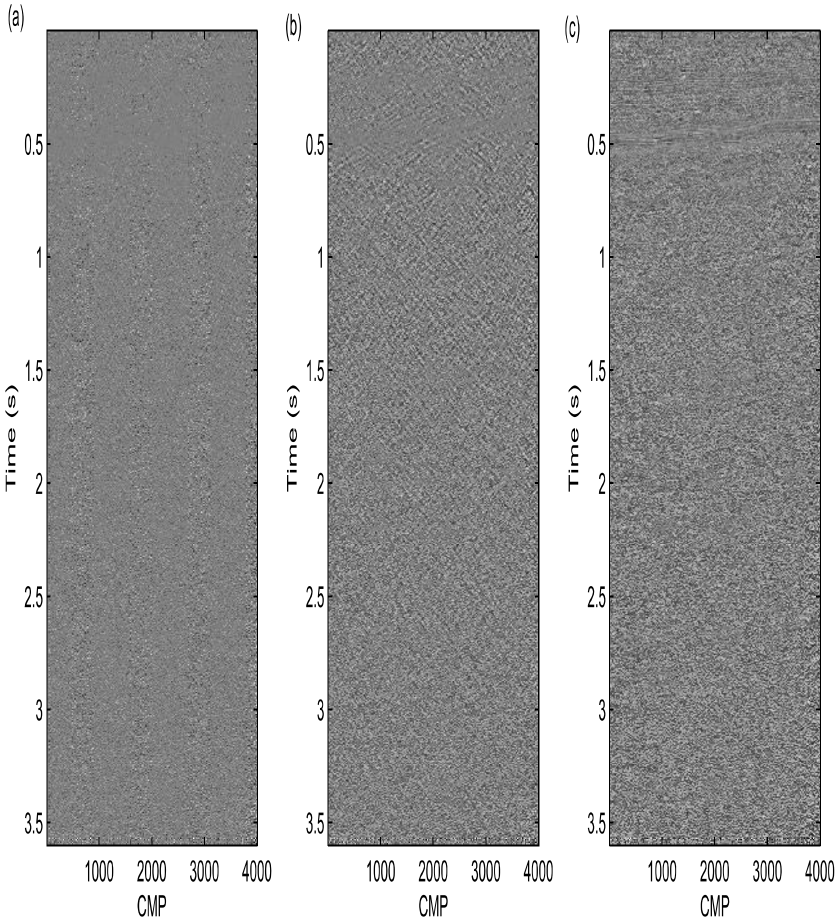

Figure 6.9: (a). The difference profile of local median filter. (b). The difference profile of local SVD filter. (c). The difference profile of BEMD thresholding. Local median filter reduces less random noise compared with the other two methods. Local SVD filter is effective for suppressing both random and coherent noise. BEMD thresholding is only valid for suppressing random noise.

(Bekara and van der Baan, 2007). The local window settings for both method are 50 and 10 for numbers of time sample and trace sample. The filter length is [5,7] for local median filter, and 1 eigenimage is used in the reconstruction for local SVD filter. All three methods upgrade the quality of the original data. Compared with the other two methods, local median filter (Figure 6.8(a)) manifests less well, as less random noise is presented in its difference profile (Figure 6.9(a)). Local SVD filter (Figure 6.8(b)) shows its powerful denoising capabilities in this data; the energy of reflections get boost and make the reflections become much clearer. From the difference profile (Figure 6.9(b)), not only random noise, the dipping coherent noise is eliminated by local SVD filter as well. The manifestation of local SVD filter is similar with the proposed f-x EEMD thresholding in chapter 4, both methods are effective for suppressing the random and coherent noise. BEMD thresholding presents better performance, and more random noise reduced than local median filter. However, since the theory of proposed method is only valid for random noise suppression, there are no coherent noise in the difference profile of BEMD thresholding (Figure 6.9(c)).

6.4.2 Seismic time slice

The second example is a seismic time slice from a sedimentary basin in Canada with the artificial random noise. Due to the influence of random noise, Figure 6.10 seems to be fuzzy. The channel and fault structures are not clear, and we mark them by the arrows. The outputs of local median filter, local SVD filter and BEMD thresholding are shown in Figure 6.11 with the same amplitude scale. The window settings for two local filters are [10,10], and the filter length is [3,3] for local median filter, and 2 eigenimage is used in the reconstruction for local SVD filter. This time, local median filter (Figure 6.11(a)) shows a better performance than local SVD filter (Figure 6.11(b)). This is because local SVD filter is effective for boosting the coherence energy, and there is no obvious coherence energy, like reflections, in this example. The output of BEMD thresholding with $m1$ =1, $m2 = 7$ and σ = 0.2 is shown in Figure 6.11(c). The proposed method effectively reduces the random noise, and the output shows smoother features compared with the other two techniques.

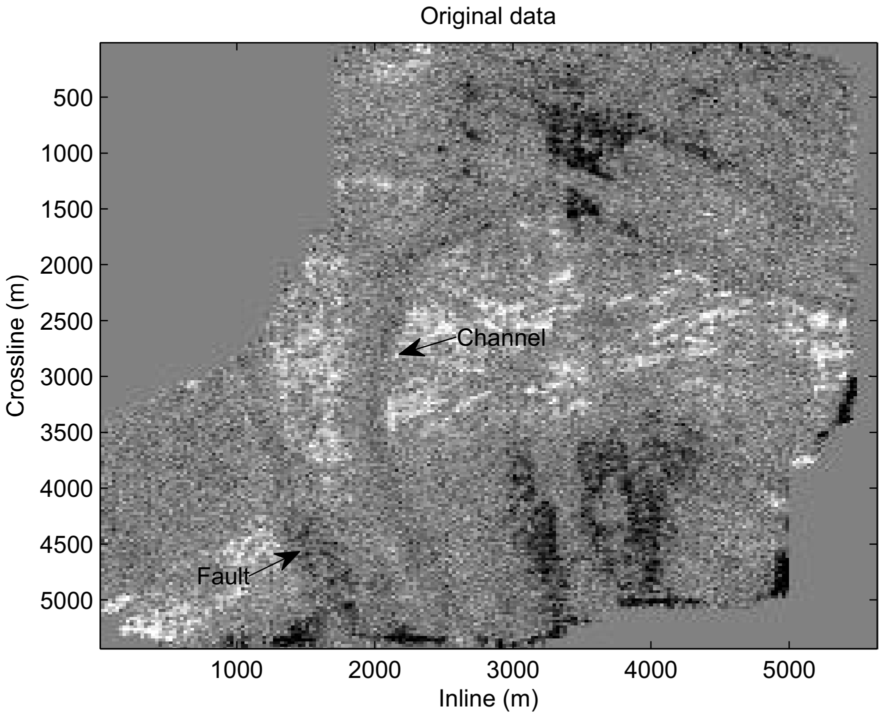

Figure 6.10: Time slice from a sedimentary basin in Canada. The time slice tends to be fuzzy due to the random noise. The channel and fault structures are marked by the arrows.

Furthermore, the channel and fault structures can be identified distinctly. No useful geologic information are lost in the difference profiles of all three methods (Figure 6.12).

6.5 Discussion

As the 2D extension of EMD, BEMD is fully data driven technique, and no predefined decomposition basis feature renders it suitable for image analysis. From equations 6.1 to 6.3, BEMD can be interpreted as a constant-Q, wavelet-like, filter bank for a 2D image. This feature is also shared with EMD (Flandrin et al., 2004a; Wu and Huang, 2004). Based on the energy distribution of each BIMF for white Gaussian noise, BEMD is capable of distinguishing the signal and noise in its own domain (BIMFs). Therefore, BEMD thresholding is essentially suppressing random

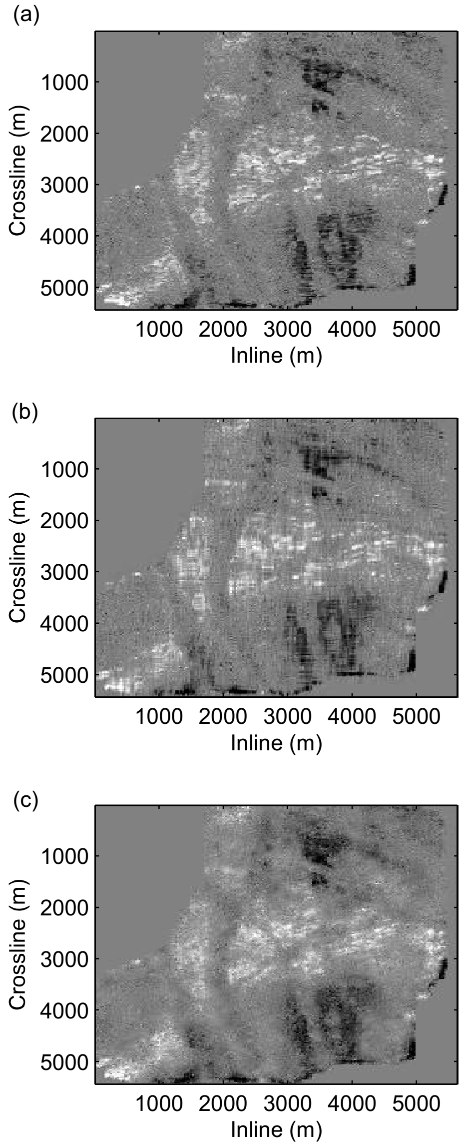

Figure 6.11: (a). Result of local median filter. (b). Result of local SVD filter. (c). Result of BEMD thresholding with $m1$ =1, $m2 = 7$ and σ = 0.2. The BEMD thresholding output is much smoother compared the other two methods, and the geologic structures can be identified distinctly.

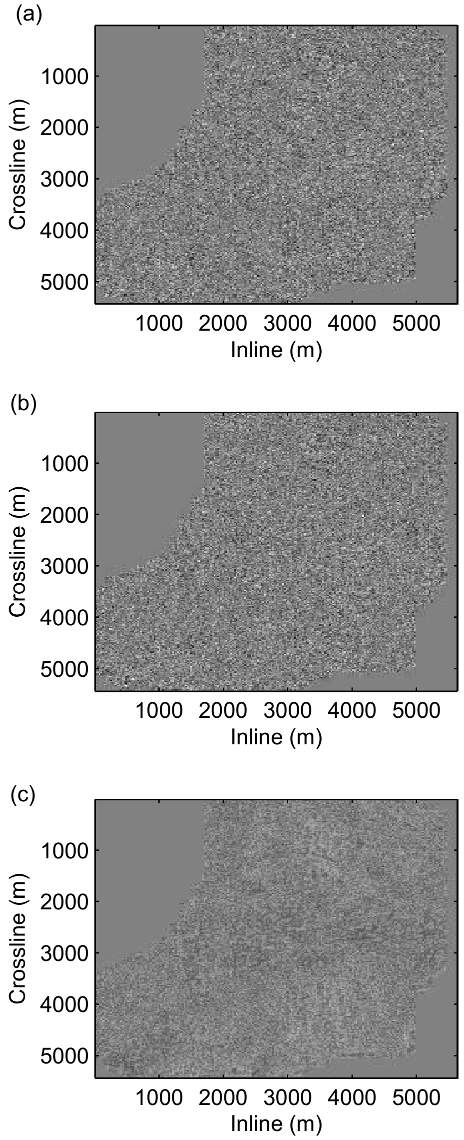

Figure 6.12: (a). Difference of local median filter. (b). Difference of local SVD filter. (c). Difference of BEMD thresholding. Most of the random noise is suppressed without any useful geologic information in all three methods.

noise in different frequencies and spatial scales of the input images.

Another possible application in seismic processing is applying the proposed method in frequency-x-y offset (f-x-y) domain, which follows the idea of f-x EEMD thresholding. The results should be valid for suppressing both random and coherent noise in 3D seismic data. Due to limited time and lack of a suitable 3D seismic dataset, we do not test f-x-y BEMD thresholding in this chapter.

Although the field examples demonstrate the good performance of the BEMD thresholding method, there are two possible improvements to enhance the results. First one is BEEMD thresholding. BEMD is suffered with mode mixing, and following the idea of EEMD thresholding in chapter 4, we could propose BEEMD thresholding for stabilizing the final denoising results. However, the computation time is the main problem preventing this idea. Even we use cubic interpolant for the proposed method, the computation time of BEMD thresholding is about 3.5 times slower than local SVD filter, and 1.5 times slower than local median filter for Alaska data. For the second example (Figure 6.9), all three methods take nearly equal computation time, as the size of the second example (217*225) is much smaller than Alaska data (1800*400). Second improvement is a new 2D thresholding method suitable for BIMFs. IMF interval thresholding (chapter 4) maintains the whole interval between two zero crossings in each IMF, if the absolute value of local extrema in this interval is larger than the threshold. The idea of IMF interval thresholding agrees with the features of each IMF, therefore it enhances the denoising capability of EEMD thresholding. In 2D case, how to keep the amplitude between two zero crossings and in which directions are need the further considerations.

6.6 Conclusion

BEMD behaves a constant-Q, wavelet-like, filter bank on the white Gaussian noise. Based on the energy distribution of each BIMF, BEMD thresholding is effective for suppressing random noise in 2D image. The seismic examples illustrate the good performance of our proposed method.

Chapter 7

Discussion and Conclusion[1]

7.1 Discussion

EMD is a fully data-driven technique, and the main parameters for EMD are the stopping criteria for the sifting process and extrme interpolation scheme (Han and Van der Baan, 2013; Mandic et al., 2013). Empirically, scholars set the default stopping criteria to perform EMD (Huang et al., 1998; Huang, 1999; Nunes and Delechelle, 2009; Wang et al., 2010). There are another two parameters for EEMD and CEEMD, namely the percentage of white Gaussian noise and the number of noise realizations, and neither seems to have a critical influence of the final decomposition. For the different examples presented in chapter 2, EEMD and CEEMD employed with the same parameters show similar time-frequency representations (EEMD results are not shown). On the other hand, the EEMD implementation tends to extract smoother IMFs with increasing IMF numbers due to a decrease in Gaussian noise fluctuations, which is not the case in the CEEMD implementation. From our tests, CEEMD is more computationally intensive than EEMD which contradicts Torres et al. (2011a) conclusions.

Since CEEMD is a complete version of EEMD, the readers may ask a question, ”why not propose the CEEMD thresholding instead of EEMD thresholding?” The

---

[1] The chapter is based in part on the paper ”Spectral estimation - What’s new? What’s next?”. Jean Baptiste Tary, Roberto Henry Herrera, Jiajun Han and Mirko van der Baan, submitted, Reviews of Geophysics.

answer is the EMD denoising foundation is based on equation 4.1, which needs the decomposition of the input signal by the full EMD scheme. In this case, CEEMD does not obey this feature, which simply means the IMFs energy after CEEMD may not follow equation 4.1.

Shared with EMD, the stopping criteria are the main parameters for BEMD. As a reassignment approach on wavelet transform, mother wavelet and the number of octaves and voices are the main parameters for SST. The reassignment method applied on instantaneous frequencies for the SST improves the time-frequency representation of the wavelet transform, and judging from various applications, SST shows its robustness properties to noisy or non-uniformly sampled data (Thakur et al., 2013; Auger et al., 2013). EMD and its variants offer high-resolution time-frequency representation for signals characterized by good SNR, like noise free synthetic data and post-stack seismic data (chapter 2). On the downside, the EMD algorithm seems very sensitive to the low SNR case as no criteria to separate noise and signal are defined in this kind of algorithm. Instantaneous frequencies computed from EMD IMFs have an inconsistent aspect in the presence of high-amplitude broadband noise (Bowman and Lees, 2013) and for close spectral lines (Mandic et al., 2013).

There are several possible improvements associated with the presented methods.

For EMD and its variants, combining with other alternative transform(s) to calculate frequency distribution may be a avaiable way. EMD or its variants aims to decompose the input signal into a sum of subsignals based on its dyadic filter structure, even if the input signal contains noise. However, instantaneous frequency is prone and sensitive to noise, direct calculation in noisy situations may reduce the performance. Furthermore, some natural signals, like volcano signals, with broadband spectra are not well represented by instantaneous frequency.

For SST, an automatic, data-driven selection of the main parameters for the CWT (mother wavelet, central frequency and bandwidth) (Mesa, 2005) could remove the usual trial-and-error procedure.

For all the presented techniques, the objects of them are huge seismic data, therefore modern computational tools and programming languages should help mitigate the time consuming problem.

7.2 Conclusion

EMD methods offers potentially viable tools for seismic processing and interpretation, and this thesis focuses on testing their suitability for seismic time-frequency analysis and attenuation noise. EMD offers a distinct way for revealing time-frequency distribution of input signals compared with the previous developed techniques, as there are no template, window and taper usages during its implementation, and no estimation assumptions exist. As an EMD variant, CEEMD decomposes the seismic signals into a sum of narrow band subsignals, and its performance in combination with instantaneous frequency retrieves higher time-frequency resolution. This feature is also true for SST, which is an EMD-like method empowered by reassignment approach on wavelet transform. Furthermore, EMD and BEMD both effectively distinguish the signal and random noise in each IMF and BIMF; based on these characteristics, the proposed EEMD thresholding and BEMD thresholding are useful tools for denoising seismic data. The applications on synthetic and real data illustrate the EMD methods are highly promising for seismic processing and interpretation.

Bibliography

Auger, F. and P. Flandrin. “Improving the readability of time-frequency and time-scale representations by the reassignment method.” *IEEE Trans. Signal Process.* 43 (1995): 1068–1089.

Auger, F., Flandrin P., Lin Y., McLaughlin S., Meignen S., Oberlin O., and Wu H.T. “Time-Frequency Reassignment and Synchrosqueezing: An overview.” *IEEE Signal Processing Magazine* 30 (2013): 32–41.

Barnes, A.E. “Instantaneous spectral bandwidth and dominant frequency with applications to seismic reflection data.” *Geophysics* 58 (March 1993): 419–428.

Barnes, A.E. “Weighted average seismic attributes.” *Geophysics* 65 (2000): 275–285.

Barnes, A.E. “A tutorial on complex seismic trace analysis.” *Geophysics* 72 (2007): W33–W43.

Battista, B.M., A. Addison, and C. Knapp. “Empirical mode decomposition operator for dewowing GPR data.” *JEEG* 14 (2009): 163–169.

Battista, B.M., C. Knapp, T. McGee, and V. Goebel. “Application of the empirical mode decomposition and Hilbert-Huang transform to seismic reflection data.” *Geophysics* 72 (2007): H29–H37.

Bednar, J. B. “Applications of median filtering to deconvolution, pulse estimation, and statistical editing of seismic data.” *Geophysics* 48 (December 1983): 1598–1610.

Bekara, M. and M. van der Baan. “Local singular value decomposition for signal enhancement of seismic data.” *Geophysics* 72 (2007): V59–V65.

Bekara, M. and M. Van der Baan. “Random and coherent noise attenuation by empirical mode decomposition.” *Geophysics* 74 (2009): V89–V98.

Bhuiyan, Sharif M. a., Reza R. Adhami, and Jesmin F. Khan. “A novel approach of fast and adaptive bidimensional empirical mode decomposition.” *2008 IEEE International Conference on Acoustics, Speech and Signal Processing* 2 (March 2008): 1313–1316.

Bhuiyan, Sharif M.a., Jesmin F. Khan, Nii O. Attoh-Okine, and Reza R. Adhami. “Study of Bidimensional Empirical Mode Decomposition Method for Various Radial Basis Function Surface Interpolators.” *2009 International Conference on Machine Learning and Applications* (December 2009): 18–24.

Boashash, B. and M. Mesbah. “Signal Enhancement by Time-Frequency Peak Filtering.” *IEEE transaction on signal processing* 52 (2004): 929–937.

Bonar, D. and M.D Sacchi. “Spectral decomposition with f-x-y preconditioning.” *Geophysical Prospecting* 61 (June 2013): 152–165.

Boudraa, A.O. and J.C. Cexus. “Denoising via empirical mode decomposition.” *Proc. IEEE ISCCSP* 2 (2006).

Bowman, D. C. and J. M. Lees. “The Hilbert-Huang Transform: A High Resolution Spectral Method for Nonlinear and Nonstationary Time Series.” *Seismological Research Letters* 84 (October 2013): 1074–1080.

Brigham, E. O. *The fast Fourier transform and its applications*. Volume 5 . Prentice-Hall, 1998.

Canales, L. “Random Noise Reduction 54th Ann International Meeting.” *SEG Expanded Abstract* 24 (February 1984): 525–527.

Castagna, J., S. Sun, and R. Siegfried. “Instantaneous spectral analysis: Detection of low-frequency shadows associated with hydrocarbons.” *The Leading Edge* 22 (2003): 120.

Castellanos, F. and M. van der Baan. “Microseismic Event Locations using the Double-Difference Algorithm.” *CSEG Recorder* (2013): 26–37.

Chakraborty, A. and D. Okaya. “Frequency-time decomposition of seismic data using wavelet-based methods.” *Geophysics* 60 (November 1995): 1906–1916.

Chang, K. and S. Liu. “Gaussian Noise Filtering from ECG by Wiener Filter and Ensemble Empirical Mode Decomposition.” *Journal of Signal Processing Systems* 64 (February 2010): 249–264.

Chen, K. *Robust matrix rank reduction methods for seismic data processing*. PhD thesis, 2013.

Chen, S., D. Donoho, and M. Saunders. “Atomic decomposition by basis pursuit.” *SIAM journal on scientific computing* 43 (2001): 129–159.

Chen, W., S. Wang, X. Chuai, and Z. Zhang. “Random Noise Reduction Based on Ensemble Empirical Mode Decomposition and Wavelet Threshold Filtering.” *Advanced Materials Research* 518-523 (May 2012): 3887–3890.

Chen, Y, T Liu, and Y Zhang. “Random Noise Attenuation by a Hybrid Approach Using fx Empirical Mode Decomposition and Multichannel Singular Spectrum.” *76th EAGE Conference and Exhibition 2014* (2014): 16–19.

Chen, Y. and J. Ma. “Random noise attenuation by fx empirical-mode decomposition predictive filtering.” *Geophysics* 79 (2014): V81–V91.

Cooley, JW. “The fast Fourier transform and its applications.” *. . . , IEEE Transactions on* 12 (1969): 27–34.

Cooley, JW. and JW. Tukey. “An algorithm for the machine calculation of complex Fourier series.” *Mathematics of computation* 19 (1965): 297–301.

Damerval, C., S. Meignen, and V. Perrier. “A fast algorithm for bidimensional EMD.” *IEEE Signal Processing Letters* 12 (October 2005): 701–704.

Daubechies, I. “Ten lectures on wavelets: Society for Industrial and Applied Mathematics..” *CBMS-NSF regional conference series in applied mathematics*. 1992.

Daubechies, I., J. Lu, and H. Wu. “Synchrosqueezed wavelet transforms: An empirical mode decomposition-like tool.” *Applied and Computational Harmonic Analysis* 30 (March 2011): 243–261.

Daubechies, I. and S. Maes. “A nonlinear squeezing of the continuous wavelet transform based on auditory nerve models.” *Wavelets in Medicine and Biology*. Boca Raton, FL: CRC Press, 1996, 527–546.

Delechelle, E, J Nunes, and J Lemoine. “Empirical mode decomposition synthesis of fractional processes in 1D- and 2D-space.” *Image and Vision Computing* 23 (September 2005): 799–806.

Dong, L., Z. Li, and D. Wang. “Curvelet threhold denoising joint with empirical mode decomposition.” *SEG Houston 2013 Annual Meeting*. 2013, 4412–4416.

Donoho, D. “De-noising by soft-thresholding.” *IEEE Transactions on Information Theory* 41 (May 1995): 613–627.

Donoho, D. and J. Johnstone. “Ideal spatial adaptation by wavelet shrinkage.” *Biometrika* 81 (1994): 425–455.

Flandrin, P., P. Goncalves, and G. Rilling. “Detrending and denoising with empirical mode decompositions.” *European Signal Processing Conference*. Citeseer, 2004, 1581–1584.

Flandrin, P., G. Rilling, and P. Goncalves. “Empirical Mode Decomposition as a Filter Bank.” *IEEE Signal Processing Letters* 11 (February 2004): 112–114.

Flandrin, P., G. Rilling, and P. Goncalves. “Empirical mode decomposition as a filter bank.” *Signal Processing Letters, IEEE* 11 (2004): 112–114.

Fomel, S. “Local seismic attributes.” *Geophysics* 72 (2007): A29–A33.

Fomel, S. “Seismic data decomposition into spectral components using regularized nonstationary autoregression.” *Geophysics* 78 (2013): O69–O76.

Gabor, D. “Theory of communication. Part 1: The analysis of information.” *Engineers-Part III: Radio and Communication* 93 (1946): 429–457.

Geological-Survey, US. “http://wiki.seg.org/wiki/ALASKA_2D_LAND_LINE_31–81.” (1981).

Hall, M. “Resolution and uncertainty in spectral decomposition.” *first break* 24 (2006): 43–47.

Han, J., R.H. Herrera, and M. Van der Baan. “Spectral decomposition by synchrosqueezing transform.” *75th Mtg., EAGE London*. 2013.

Han, J., RH. Herrera, and M. VanderBaan. “Spectral Decomposition by Synchrosqueezing Transform.” *75th EAGE Conference*. 2013, 1–5.

Han, J. and M. Van der Baan. “Empirical Mode Decomposition and Robust Seismic Attribute Analysis.” *2011 CSPG CSEG CWLS Convention* 114 (2011): 1–4.

Han, J. and M. Van der Baan. “Empirical mode decomposition for seismic time-frequency analysis.” *Geophysics* 78 (2013): O9–O19.

Han, J. and M. Van der baan. “Empirical mode decomposition for seismic time-frequency analysis.” *Geophysics* 78 (2013): accepted.

Han, J. and M. Van der Baan. “Empirical mode decomposition for seismic time-frequency analysis.” *Geophysics* 78 (2013): O9–O19.

Han, L., M.D Sacchi, and L. Han. “Spectral decomposition and de-noising via time-frequency and space-wavenumber reassignment.” *Geophysical Prospecting* 62 (December 2013): 244–257.

Herrera, RH., J. Han, and M. Van der Baan. “Applications of the synchrosqueezing transform in seismic time-frequency analysis.” *Geophysics* 79 (2014): V55–V64.

Herrera, R.H., R. Orozco, and M. Rodriguez. "Wavelet-based deconvolution of ultrasonic signals in nondestructive evaluation." *Journal of Zhejiang University SCIENCE A* 7 (October 2006): 1748–1756.

Hinich, M.J. and C.S. Clay. "The application of the discrete Fourier transform in the estimation of power spectra, coherence, and bispectra of geophysical data." *Reviews of geophysics* 6 (1968): 347–363.

Huang, J., B. Zhao, Y. Chen, and P. Zhao. "Bidimensional empirical mode decomposition (BEMD) for extraction of gravity anomalies associated with gold mineralization in the Tongshi gold field, Western Shandong Uplifted Block, Eastern China." *Computers & Geosciences* 36 (July 2010): 987–995.

Huang, JW. and B. Milkereit. "Empirical Mode Decomposition Based Instantaneous Spectral Analysis and its Applications to Heterogeneous Petrophysical Model Construction." *Frontiers+Innovation-2009 CSPG CSEG CWLS Convention*. 2009, 205–210.

Huang, N. E. "A new view of nonlinear water waves: The Hilbert spectrum." *Annual Review of Fluid Mechanics* 31 (January 1999): 417–457.

Huang, N. E. and S.S. Shen. *Hilbert-Huang transform and its applications*. Volume 5 . World Scientific Pub Co Inc, 2005.

Huang, N. E., Z. Wu, S. R. Long, K. C. Arnold, X. Chen, and B. Karin. "On instantaneous frequency." *Advances in Adaptive Data Analysis* 1 (December 2009): 177–229.

Huang, N.E., Z. Shen, and S.R. Long. "A New View of Nonlinear Water Waves: The Hilbert Spectrum." *Annual Review of Fluid Mechanics* 31 (1999): 417–457.

Huang, N.E., Z. Shen, S.R. Long, M.C. Wu, H.H. Shih, Q. Zheng, N.C. Yen, C. C. Tung, and H.H. Liu. "The empirical mode decomposition and the Hilbert spectrum for nonlinear and non-stationary time series analysis." *Proceedings of the Royal Society of London. Series A: Mathematical, Physical and Engineering Sciences* 454 (1998): 903–995.

Huang, N.E., M.-L. C. Wu, S.R. Long, S.S.P. Shen, W. Qu, P. Gloersen, and K.L. Fan. "A confidence limit for the empirical mode decomposition and Hilbert spectral analysis." *Proceedings of the Royal Society of London. Series A: Mathematical, Physical and Engineering Sciences* 459 (2003): 2317–2345.

Kay, S. and S. Marple. "Spectrum analysis a modern perspective." *Proceedings of the IEEE* 69 (1981): 1380–1419.

Kopsinis, Y. and S. McLaughlin. "Empirical mode decomposition based denoising techniques." *IAPR Workshop: Cognitive Information ...* (2008): 42–47.

Kopsinis, Y. and S. McLaughlin. "Empirical Mode Decomposition Based Soft-Thresholding." 2008.

Kopsinis, Y. and S. McLaughlin. "Development of EMD-Based Denoising Methods Inspired by Wavelet Thresholding." *IEEE Transactions on Signal Processing* 57 (April 2009): 1351–1362.

Kumar, P. and E. Foufoula-Georgiou. "Wavelet analysis for geophysical applications." *Reviews of Geophysics* 35 (1997): 385.

Li, C. and M. Liang. "A generalized synchrosqueezing transform for enhancing signal time-frequency representation." *Signal Processing* 92 (September 2012): 2264–2274.

Li, C. and M. Liang. "Time-frequency signal analysis for gearbox fault diagnosis using a generalized synchrosqueezing transform." *Mechanical Systems and Signal Processing* 26 (January 2012): 205–217.

Li, Y. and X. Zheng. "Spectral decomposition using Wigner-Ville distribution with applications to carbonate reservoir characterization." *The Leading Edge* 27 (2008): 1050–1057.

Linderhed, A. "2D empirical mode decompositions in the spirit of image compression." *Proceedings of SPIE* 4738 (2002): 1–8.

Linderhed, A. “Variable sampling of the empirical mode decomposition of two-dimensional signals.” *International Journal of Wavelets Multiresolution and Information Processing* 3 (2005): 1–15.

Liu, G., S. Fomel, and X. Chen. “Time-frequency analysis of seismic data using local attributes.” *Geophysics* 76 (2011): P23–P34.

Liu, J and K.J. Marfurt. “Thin bed thickness prediction using peak instantaneous frequency.” *SEG EXpanded Abstracts* (2006): 968–972.

Liu, J and K.J. Marfurt. “Instantaneous spectral attributes to detect channels.” *Geophysics* 72 (2007): P23–P31.

Liu, Z. and S. Peng. “Boundary Processing of bidimensional EMD using texture synthesis.” *IEEE Signal Processing Letters* 12 (January 2005): 33–36.

Magrin-Chagnolleau, I. and R.G. Baraniuk. “Empirical mode decomposition based time-frequency attributes.” *69th SEG Meeting* (1999): 1949–1952.

Makhoul, J. “Spectral linear prediction: properties and applications.” *IEEE Transactions on Acoustics, Speech, and Signal Processing* 23 (1975): 283–296.

Mallat, S. *A Wavelet Tour of Signal Processing: The Sparse Way*. 3rd edition. Academic Press, 2008.

Mallat, SG and Z Zhang. “Matching pursuits with time-frequency dictionaries.” *Signal Processing, IEEE Transactions on* 41 (1993): 3397 – 3415.

Mandic, D.P., Z. Wu, and Huang N.E. “Empirical Mode Decomposition-Based Time-Frequency Analysis of Multivariate Signals: The power of Adaptive Data Analysis.” *IEEE Signal Processing Magazine* 30 (2013): 74–86.

Marfurt, K.J. and R.L. Kirlin. “Narrow-band spectral analysis and thin-bed tuning.” *Geophysics* 66 (2001): 1274–1283.

Meignen, S., T. Oberlin, and S. McLaughlin. “A New Algorithm for Multicomponent Signals Analysis Based on SynchroSqueezing: With an Application to

Signal Sampling and Denoising." *Signal Processing, IEEE Transactions on* 60 (nov. 2012): 5787 –5798.

Mesa, Hector. "Adapted wavelets for pattern detection." *Lecture Notes in Computer Science* 3773 (2005): 933–944.

Morlet, J, G Arensz, and E Fourgeau. "Wave propagation and sampling theory-Part II: Sampling theory and complex waves." *Geophysics* 47 (1982): 222–236.

Nunes, J., O Niang, Y Bouaoune, E Delechelle, and P. Bunel. "Bidimensional empirical mode decomposition modified for texture analysis." *Image Analysis* (2003): 295–296.

Nunes, J. C. and E Delechelle. "Empirical mode decomposition: applications on signal and image processing." *Advances in Adaptive Data Analysis* 1 (2009): 125–175.

Nunes, J. C., S. Guyot, and E Delechelle. "Texture analysis based on local analysis of the Bidimensional Empirical Mode Decomposition." *Machine Vision and Applications* 16 (May 2005): 177–188.

Odebeatu, E., J. Zhang, M. Chapman, E. Liu, and X.Y. Li. "Application of spectral decomposition to detection of dispersion anomalies associated with gas saturation." *The Leading Edge* 25 (2006): 206–210.

Oropeza, V. and M.D Sacchi. "A randomized SVD for multichannel singular spectrum analysis (MSSA) noise attenuation." *2010 SEG Annual Meeting* (2010): 3539–3544.

Oropeza, V. and M.D Sacchi. "Simultaneous seismic data denoising and reconstruction via multichannel singular spectrum analysis." *Geophysics* 76 (May 2011): V25–V32.

Partyka, G., J. Gridley, and J. Lopez. "Interpretational applications of spectral decomposition in reservoir characterization." *The Leading Edge* 18 (March 1999): 353.

Qin, X., S. Liu, Z. Wu, and H. Jun. "Medical Image Enhancement Method Based on 2D Empirical Mode Decomposition." *2008 2nd International Conference on Bioinformatics and Biomedical Engineering* (May 2008): 2533–2536.

Quan, Y. and J.M. Harris. "Seismic attenuation tomography using the frequency shift method." *Geophysics* 62 (1997): 895–905.

Reine, C., R. Clark, and M. Van der Baan. "Robust prestack Q-determination using surface seismic data: Part 1: Method and synthetic examples." *Geophysics* 77 (2012): R45–R56.

Reine, C., M. Van der Baan, and R. Clark. "The robustness of seismic attenuation measurements using fixed- and variable-window time-frequency transforms." *Geophysics* 74 (2009): WA123–WA135.

Rioul, O. and M. Vetterli. "Wavelets and signal processing." *Signal Processing Magazine, IEEE* (1991): 14–38.

Sacchi, M.D. "FX singular spectrum analysis." *CSPG CSEG CWLS Convention* (2009): 392–395.

Sacchi, M.D and H. Kuehl. "ARMA formulation of FX prediction error filters and projection filters." *Journal of seismic exploration* 9 (2001): 185–197.

Saha, J. G. "Relationship between Fourier and instantaneous frequency." *57th Annual International Meeting, SEG, Expanded Abstracts*. 1987, 591–594.

Sapidis, N and R Perucchio. "Delaunay triangulation of arbitrarily shaped planar domains." *Computer Aided Geometric Design* 8 (December 1991): 421–437.

Sinclair, S. and G. G. S. Pegram. "Empirical Mode Decomposition in 2-D space and time: a tool for space-time rainfall analysis and nowcasting." *Hydrology and Earth System Sciences Discussions* 2 (February 2005): 289–318.

Soubaras, R. "Signal-preserving random noise attenuation by the f-x projection." *SEG Technical Program Expanded Abstracts* (January 1994): 1576–1579.

Stockwell, R.G. “Why use the S-transform.” *American Mathematical Society* 52 (2007): 279–309.

Stockwell, R.G., L. Mansinha, and R.P. Lowe. “Localization of the complex spectrum: the S transform.” *IEEE Transactions on Signal Processing* 44 (April 1996): 998–1001.

Taner, M.T., F. Koehler, and R.E. Sheriff. “Complex seismic trace analysis.” *Geophysics* 44 (November 1979): 1896.

Thakur, G., E. Brevdo, N.S. Fučkar, and H.T. Wu. “The Synchrosqueezing algorithm for time-varying spectral analysis: Robustness properties and new paleoclimate applications.” *Signal Processing* 93 (May 2013): 1079–1094.

Tong, W, Zhang M., Yu Q., and Zhang. H. “Comparing the applications of EMD and EEMD on time-frequency analysis of seismic signal.” *Journal of Applied Geophysics* 83 (August 2012): 29–34.

Torres, M.E., M.A. Colominas, G. Schlotthauer, and P. Flandrin. “A complete ensemble empirical mode decomposition with adaptive noise.” *2011 IEEE International Conference on Acoustics, Speech and Signal Processing (ICASSP)*. IEEE, 2011, 4144–4147.

Torres, M.E., M.A. Colominas, G. Schlotthauer, and P. Flandrin. “A complete ensemble empirical mode decomposition with adaptive noise.” *IEEE International Conference on Acoustics, Speech and Signal Processing (ICASSP)*. 2011, 4144 –4147.

Tsolis, G. and TD. Xenos. “Signal Denoising Using Empirical Mode Decomposition and Higher Order Statistics..” *International Journal of Signal …* 4 (2011): 91–106.

Ulrych, T. J. and T. N. Bishop. “Maximum Entropy Spectral Analysis and Autoregressive Decomposition.” *Reviews of Geophysics and Space Physics* 13 (1975): 183–200.

Van der Baan, M., S. Fomel, and M. Perz. "Nonstationary phase estimation: A tool for seismic interpretation?." *The Leading Edge* 29 (2010): 1020–1026.

Vasudevan, K. and Cook F.A. "Empirical mode skeletonization of deep crustal seismic data: Theory and applications." *Journal of Geophysical research* 105 (2000): 7845–7856.

Vera Rodriguez, I., D. Bonar, and M.D Sacchi. "Microseismic data denoising using a 3C group sparsity constrained time-frequency transform." *Geophysics* 77 (2012): V21–V29.

Wang, G., X. Chen, F. Qiao, Z. Wu, and N.E. Huang. "on Intrinsic Mode Function." *Advances in Adaptive Data Analysis* 02 (2010): 277–293.

Wu, H.-T., P. Flandrin, and I. Daubechies. "One or Two Frequencies? the Synchrosqueezing Answers." *Advances in Adaptive Data Analysis (AADA)* 03 (April 2011): 29–39.

Wu, Z. and N. E. Huang. "A study of the characteristics of white noise using the empirical mode decomposition method." *Proceedings of the Royal Society A: Mathematical, Physical and Engineering Sciences* 460 (June 2004): 1597–1611.

Wu, Z. and N. E. Huang. "Ensemble Empirical Mode Decomposition: a Noise-Assisted Data Analysis Method." *Advances in Adaptive Data Analysis* 01 (2009): 1–41.

Wu, Z. and N.E. Huang. "Ensemble Empirical Mode Decomposition: a Noise-Assisted Data Analysis Method." *Advances in Adaptive Data Analysis* 1 (2009): 1–41.

Xu, Y., B. Liu, J. Liu, and S. Riemenschneider. "Two-dimensional empirical mode decomposition by finite elements." *Proceedings of the Royal Society A: Mathematical, Physical and Engineering Sciences* 462 (October 2006): 3081–3096.

Appendix A

From 1D Instantaneous Attributes to 2D Instantaneous Spectra

In this appendix, I show how to create the 2D instantaneous spectra after calculating the instantaneous attributes of each IMF.

Assume we have obtained $imf_i(t)$ after EMD on the input signal $s(t)$, and their instantaneous amplitude $A_i(t)$ (equation (2.8)) and corresponding instantaneous frequencies $IF_i(t)$ (equation (2.10)) are calculated, where index $i = 1, 2, ...k$. As the signal $s(t)$ equals the summation of every $imf_i(t)$, its instantaneous spectra $S(t, f)$ is the summation of all the individual instantaneous spectra $IMF_i(t, f)$ of each $imf_i(t)$. This relationship is expressed as equation (A-1)

$$s(t) = \sum_{i=1}^{k} imf_i(t) \Longleftrightarrow S(t, f) = \sum_{i=1}^{k} IMF_i(t, f), \qquad (A-1)$$

The instantaneous spectrum $IMF_i(t, f)$ is calculated from its instantaneous amplitude $A_i(t)$ and corresponding instantaneous frequency $IF_i(t)$ as,

$$IMF_i(t, f) = A_i(t)\delta(f - IF_i(t)). \qquad (A-2)$$

where δ is the Dirac delta function.

Next I show an example. Figure A-1(a) shows the instantaneous amplitude of one synthetic IMF, and its corresponding instantaneous frequency is shown in Figure A-1(b). Figure A-2 is the instantaneous spectrum created by the information in Figure A-1 utilizing equation (A-2).

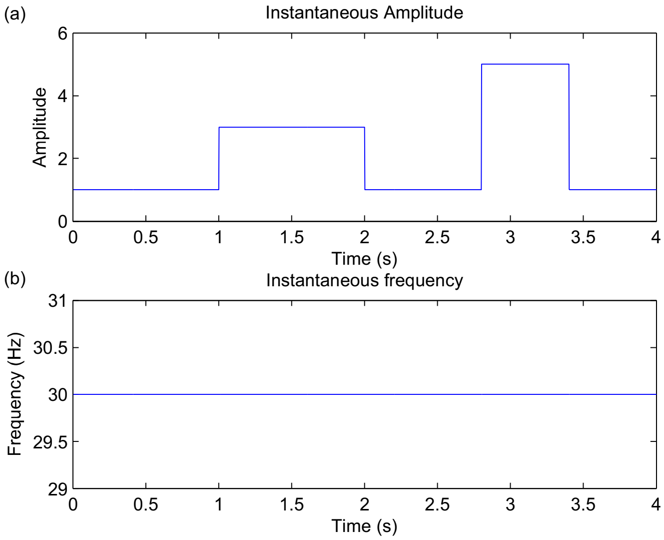

Figure A-1: (a). The instantaneous amplitude of one synthetic IMF. (b). The instantaneous freqeuncy of one synthetic IMF.

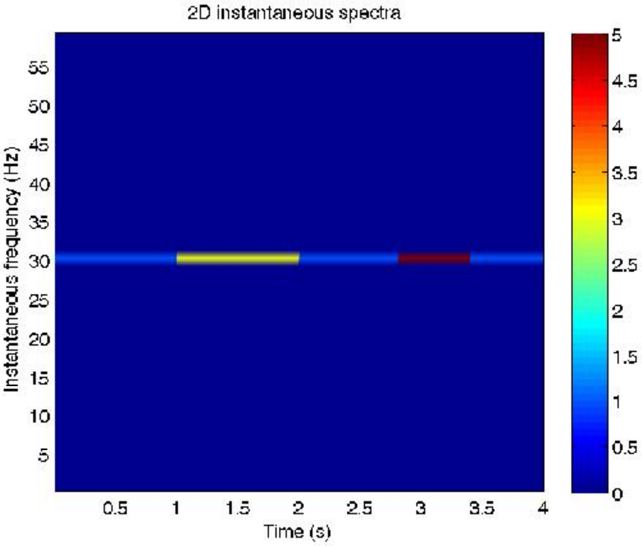

Figure A-2: The 2D spectrum created from Figure A-1.

Appendix B

Explanation on white noise injection for relieving mode mixing

Mode mixing means that different frequency components mix together in one IMF, or one frequency component is represented in different IMFs but at different times (see Figure 2.2). In this situation, the instantaneous frequency of IMFs fluctuates rapidly.

Noise injection is effective for relieving mode mixing. Take CEEMD as an example, CEEMD utilizes bandpassed versions of white noise in each stage when extracting different IMFs. Flandrin et al. (2004a) demonstrated that white Gaussian noise is divided into IMFs, each characterized by a different octave in the frequency domain. During the CEEMD decomposition, equations (2.3) and (2.4), different noise IMFs $E_k[w_i]$ are added to the residual r_k, thereby adding bandpass filtered noise of a specific frequency content to the residual. This promotes extraction of IMFs with a more restricted frequency range, thus preventing mode mixing.

The added white Gaussian noise series helps to perturb the signal and enable the EMD to visit multiple solutions in the finite neighborhood of the true answer. As the added noise series are zero mean, their contribution thus cancels out and does not introduce signal components not already present in the original data. The ensemble averaging also introduces smooth features of each IMF.